Preparation of high-conductivity, high-capacity phase change media capsules with enhanced thermos-chemical stability in thermal energy storage applications

Thèse N° 9715

Présentée le 28 octobre 2019

à la Faculté des sciences et techniques de l'ingénieur
Laboratoire de la science et de l'ingénierie de l'énergie renouvelable
Programme doctoral en energie

pour l'obtention du grade de Docteur ès Sciences

par

Selmar Rudolf BINDER

Acceptée sur proposition du jury

Dr K. Mikityuk, président du jury
Prof. S. Haussener, Dr. L. Weber, directeurs de thèse
Prof. H. Walter, rapporteur
Prof. L. Fischer, rapporteur
Prof. J. Van Herle, rapporteur

2019

ÉCOLE POLYTECHNIQUE
FÉDÉRALE DE LAUSANNE

Acknowledgements

First and foremost, I would like to thank my thesis director, Prof. Sophia Haussener, for her continuous support and supervision, and the opportunities she has provided me with. Her guidance has been invaluable in writing this thesis and her strive for excellence has undoubtable left a lasting impression on me. My thesis' co-director, Dr. Ludger Weber, deserves my gratitude for continued advice and corrections, as well as the occasional pad on the shoulder.

Prof. Andreas Mortensen, whose benevolence helped to spark this project, deserves my gratitude for advice and for granting the project complete access to the Laboratory for Mechanical Metallurgy (EPFL, Switzerland). Prof. Heinrich Hofmann receives my gratitude for his advice, for allowing me to use the facilities at the Powder Technology Laboratory (EPFL, Switzerland), for offering his help, and for taking his time to sit down with a young doctoral student and discuss the details of his research project, even though he had no professional obligation. Prof. Colin Pulham (University of Edinburgh, United Kingdom) helped us to get instrument time at the General Materials Diffractometer (GEM, ISIS-Neutron and Muon Source). His advice and warm welcome during my visit of the Harwell Campus are gratefully acknowledged.

To my colleagues, whom without exception I consider my friends, it has been a delightful experience to work with so many smart and kindhearted people. Working in the environment that they create is a privilege that has left me humbled and inspired at the same time. Nithin Mallya is an ideal office mate and receives my thanks for approximately 500 small pointers with regard to software and literature. I would like to thank David Perraudin for being a trusty companion during the first and second year. I thank Dr. Silvan Suter for being a creative and inclusive thinker, and making

me feel like I had a brother. Dr. Isaac Holmes is a delightful partner for intellectual arguments, who enjoys them likely as much as I do. Thank you for your insight, interest, and for taking things the right way. I thank Dr. Clemens Suter, to whom I am indebted for professional support and advice beyond what I can likely ever return – and for his selfless and responsible conduct. I thank Dr. Saurabh Tembhurne and Dr. Meng Lin for being great seniors and shining role models.

To my less immediate colleagues at EPFL and around the world, who go out of their way to help another researcher, as one does with one's neighbors, Gionata Schneider (Laboratory for Mechanical Metallurgy, EPFL, Switzerland), for assistance with SEM imaging is gratefully acknowledged. Dr. Felix Messerschmitt (Electrochemical Materials Laboratory, ETHZ, Switzerland) is gratefully acknowledged for his assistance in obtaining and analyzing EDX data.

Then I thank my Students and interns. I have very much enjoyed teaching each one of them and observing their skills develop: Svyat Sudakov, Pascal Diller, Loïc Favre, Michael Kessler, Steven Schenk, … - Keep it up!

Reinhold Frei AG (8493 Saland ZH, Switzerland) supplied Al-12%Si alloy under non-profit conditions, for a good cause.

Finally, I am sincerely grateful to the Swiss science foundation, and the people who work there. Some of them I had the privilege to meet, and all of them have given me good reason to believe that the Science of this country is in good hands.

Lausanne, July 9, 2019 Selmar Binder

This work was performed with the financial support of the National Research Program "Energy Turnaround" (NRP 70) of the Swiss National Science Foundation (SNSF) under Grant #153780. Further information on the National Research Program is available at www.nrp70.ch.

Abstract

Thermal energy storage using the effects of the latent heat in the solid-liquid phase transformation has been discussed for high-temperature applications since the 1980. Reusable, organic phase change media stabilize low temperatures of parcels, and salt/water tanks act as buffer storage in residential heating/cooling and industrial processes. Emerging, renewable technologies for energy production and conversion profit from high operation temperatures. Alloys from abundant metals such as aluminum, silicon, and copper have suitable melting characteristics to preheat chemical conversion catalysts and process gas streams for heat-to-power applications. They typically absorb and release a large heat of fusion, facilitate better heat transport compared to salts, and are inert to thermal decomposition compared to organic compounds. Fundamental challenges emerge from the high reactivity of molten metals towards the preferred metal encapsulation materials. Stable encapsulations are necessary to protect the storage medium, and to preserve a constant heat exchange surface during the phase transition. This thesis explores the fabrication of stainless-steel capsules for use with pure aluminum, as well as Al-12%Si and Al-26%Cu-5%Si alloys. Experimental capsules of cylindrical shape were prepared with or without interface modification, and tested by isothermal exposure up to 800 °C and in a newly developed test-bench with 100+ melting cycles and in-situ performance measurement. Iron aluminide formation on the interior capsule surface reduced performance. Interface modifications and corrosion layers were characterized by scanning electron microscopy, energy dispersive x-ray spectrometry, differential scanning calorimetry, and Vickers hardness micro-indentation. Results were integrated into numerical diffusion and heat transfer

modelling, allowing predictions about the effects of atomic diffusivity, solubility, and thermal conductivity on heat storage performance. Ceramic diffusion barrier coatings for stabilized performance were deposited via modified reverse-dip-coating on steel encapsulation and silicon substrates, and characterized using the same methodology. Ceramic coatings and guidelines for conservative operation conditions were effective in stabilizing heat storage density and power. Boron nitride coating was demonstrated to prevent 90 % of the capacity loss occurring in the control group, in a scaled-up pilot experiment with 200 MJ latent heat capacity in encapsulated Al-26%Cu-5%Si. Temperature scanning calorimetric data from the cycling test-bench validated numerical heat transfer simulations and performance predictions from diffusion modelling. Results from validated heat and diffusion modelling were used in the design of a 1.4 MJ lab-scale prototype storage, with automated charging and discharging of stacked encapsulated samples, using air as heat transfer fluid. Herein presented guidelines allow design and operation of robust steel encapsulations, which conserve high performance for 10'000s of full-load-hours. Our experimental data and interpretative modelling focus on a relevant material class, that combines low material cost with high conductivity, large capacity, and melting temperatures relevant to advanced power cycles. Experiments on lab-, prototype- and pilot-scale demonstrate how our findings contribute to practical implementation of novel highly performant metal latent heat thermal energy storage systems.

Keywords: Heat storage, Latent heat storage, Molten metal corrosion, Heat- and mass-transfer, Degradation modelling, Diffusion barrier coating, Scale-up

Zusammenfassung

Phasenübergangs-Wärmespeicherung für Hochtemperatur-Anwendungen ist seit den 1980er Jahren kontinuierlich im wissenschaftlichen Gespräch. Sie dienst dazu, thermische Energie aus variablen Quellen schnell und zuverlässig zu speichern und wieder zur Verfügung zu stellen. Im Temperaturbereich von 400 °C aufwärts haben Legierungen aus Aluminium, Silizium und Kupfer ökonomische und technische Vorteile gegenüber Salzen, die bisher zur Anwendung gekommen sind. Grösstes Hemmnis bei der Anwendung von Metallen als Phasenübergangs-Speichermedium ist die im Bereich der Gusstechnologie bereits bekannte Flüssig-Metall-Korrosion. Besonders Aluminium ist reaktiv und bildet intermetallische Phasen mit Stahl und seinen Bestanteilen, und löst diese überdies auch auf. Um trotzdem die Vorzüge von Aluminiumlegierungen zur Prozesswärme-Speicherung nutzen zu können, bedarf es deshalb der Erforschung der Vorgänge an der Aluminium-Stahl Kontaktfläche, sowie der Entwicklung von Methoden zur Bekämpfung jener Korrosionsmechanismen. Wir untersuchen im Folgenden die Kinetik der Bildung von intermetallischen Schichten an der Kontaktfläche der Aluminium-Legierung Al-12%Si und des hochwertigen Chromnickelstahls Fe-18%Cr-10%Ni. Experimentelle Behälter wurden aus dem genannten Stahl als hohle Zylinder hergestellt und mit Bornitrid beschichteten, porösen Calciumsilikat-Einsätzen verschlossen. Zuerst wurde das Korrosionsverhalten und speziell die Wachstumsgeschwindigkeit der intermetallischen Schicht bei 600°C, 700°C, und 800°C untersucht. Die metallografischen Schliffe quer zur Zylinder-Achse der Proben zeigten ein Wachstumsverhalten, das signifikant von den Vorhersagen des Standardmodells abwich. Elektronen-Mikroskopie, energiedispersive Röntgenanalyse, Vickershärte-

Messungen und Plasma-Emissions-Spektroskopie wurden eingesetzt um die gebildeten Phasen zu identifizieren. Vom Wärmespeichermedium wurde mittels dynamischer Differenzkalorimetrie die Zeit- und Temperaturabhängigkeit der veränderlichen thermophysikalischen Kenngrössen der Schmelzwärme und Schmelztemperatur ermittelt. Vorhersagen aus optimierter numerischer Modellierung beinhalten, dass ab 650°C das Schichtwachstums durch zunehmende Löslichkeit abgemildert wird. Sperrschichten aus Keramik-Dispersionen wurden experimentell auf Verlässlichkeit und Dichtigkeit geprüft. Bornitrid Beschichtungen waren chemisch stabil und hielten zyklischen Belastungen am besten stand. Eine neue Methode zur kalorimetrischen Auswertung von zylinderförmigen latent-Wärmespeichereinheiten zeigte, dass solche Beschichtungen während bis zu 500 h und 250 lade/entlade-Vorgängen vor Kapazitätseinbussen schützten. Dies stellt einen wichtigen Fortschritt dar für die Anwendung der in ihren anderen Charakteristika vorzüglichen Schmelzwärme-Speicherlegierung Al-12%Si, da bisher keine andere Lösung der Korrosionsproblematik bekannt ist und zugleich bereits weltweit intensiv an der Entwicklung von Hochtemperatur Schmelzwärme-Speicherlösungen basierend auf dieser Legierung gearbeitet wird.

Stichworte: Wärmespeicherung, Latent-Wärme-Speicher, Flüssig-Metall-Korrosion, Wärme- und Massen-Transfer, Korrosions-Model, Diffusions-Sperr-Schicht, Anwendungs-Massstab

Table of content

List of figures

Measured and modeled interface location and thickness for the encapsulating steel (light grey), intermetallic (grey), and Al-12%Si PCM alloy (dark grey) for isothermal experiments at **a)** 600°C and **b)** 700°C. The measurements indicate average radial location of the bounding interfaces (square/triangle - markers with error bar) with the PCM and the encapsulating steel. Error bars are derived from the variation of 12 independent distance measurements per point. The computational model (black lines separating the shaded regions) and the standard parabolic growth model (red lines) were fitted to the isothermal experimental. Differences between the two models are associated to the de-passivation (initial delay, pronounced in a) and to dissolution and saturation (changes in slope).

a) Elemental composition of the PCM alloy during exposure to 700 °C isothermal condition, as determined by energy dispersive x-ray photon spectroscopy. The Fe concentration stagnates at 2.6 % after 3 days and the Si concentration increases as Al incorporates into the melt-adjacent phase. Levels of dissolved Fe and Ni increase over time, while Cr, Mn, and Mo stay below uncertainty of EDX quantification. **b)** Decrease in h_f and T_m (DSC) correlate with the increase in Fe in the PCM. h_f decreased from 462 J/g to 398 J/g. T_m decreased by 11.6 K.

a) The predicted evolution of r_1 and r_2 (smooth lines, separating shaded areas) with modified initial condition r_0=10.5 mm compared to the validation experiment (square / triangle with error bars). Agreement in qualitative behavior is notable: The velocity $\mathrm{d}w_1/\mathrm{d}t$ is positive after $t_{\varphi,0}$. Later its magnitude decreases temporarily before it finally reaccelerates. In the experimental data, $\mathrm{d}w_1/\mathrm{d}t$ is negative between 5 and 30 days. The parabolic growth model forms a straight line in the same plot (red dots). **b)** Sinusoidal variation of T_b centered at 600°C ± 50 °C (dashed gray line) predicted a prolonged onset period, compared to the 600 °C isothermal data. $\mathrm{d}r_{1/2}/\mathrm{d}t$ changed in the prediction with an oscillatory contribution from T_b.

a) Extrapolation of $\hat{h}_\mathrm{f}$ to 365 days of operation for combinations of $8 < r_0 < 48$ mm (marker size), and $575 < T_\mathrm{b} = < 735$ °C (marker color and x-axis). $\hat{h}_\mathrm{f}$ changes from the initial condition at $(\hat{h}_{\mathrm{f},0}, r_0)$ (open circles), with increasing T_b. Decrease in $\hat{h}_\mathrm{f}$ was more pronounced for small r_0, and large T_b. Each discrete variation (r_0, T_b) is composed of 32 points representing independent numerical simulations with simultaneously randomized material parameters Q_s, Q_m, D_0, and ϕ_0. **b)** Probability distribution of the mobility and solubility activation energies used for the numerical extrapolations. Mean μ_X are fitted to experimental data, while $f_\mathrm{pd} \sim \mathcal{N}(\mu_X, \sigma_X)$ assumes $\sigma_X \sim 1\%$ or 0.5% (respective shaded areas).

a) w_1 and w_2 represent corrosion of the encapsulation (positive values) and conversion of the storage medium (negative values), as a function of r_0 and T_b. w_1 increases with r_0 and T_b, while w_2 increases with T_b for small r_0 but has a maximum close to 650 °C for r_0=48 mm. **b)** Biot number as a function of temperature and initial radius for $u_\mathrm{b} = 100\ \mathrm{WK^{-1}m^{-2}}$ and varying intermetallic layer conductivity k_φ. Surface heat transfer is limiting in all cases. The maximum value of Bi=0.8 is reached for k_φ=1 $\mathrm{WK^{-1}m^{-1}}$ at the minimal radius and maximal temperature, where w_ω was also largest.

a) $\hat{h}_\mathrm{f}$ as a function of vs $\hat{q}_s$, after 365 days of simulated operation for combinations of r_0 and T_b. Large r_0 and low T_b lead to high $\hat{h}_{\mathrm{f},0}$ (open circles) and conserve storage density per overall system-mass. **b)** $\hat{h}_{\mathrm{f},0}$ as a function of ϕ_F^a. $\hat{h}_\mathrm{f}$ decreases with increasing ϕ_F^a and T_b. The trend is more pronounced for small r_0. **c)** $\hat{h}_\mathrm{f}$ as a function of D_F^a. $\hat{h}_\mathrm{f}$ decreases with increasing D_F^a. **d)** $\hat{h}_\mathrm{f}$ as a function of D_F^φ. $\hat{h}_\mathrm{f}$ decreases with increasing D_F^φ. Error bars in c) and d) indicate σ_X from probabilistic modelling (X=$\hat{h}_\mathrm{f}\ \vee D_\mathrm{F}^a \vee D_\mathrm{F}^\varphi$, respectively).

a) The modelled effect of load cycle frequency on degradation onset for a square wave profile of high ($\tilde{T} \pm 75$ K) and low ($\tilde{T} \pm 25$ K) cycle amplitudes. The delay is affected by the phase shift of the cycle (red and blue colored results), leading to a bifurcation of the observed $t_{0.\omega}$ by a factor of >20 in the high amplitude case. For high frequencies $t_{0.\omega}$ approaches 3 days and 1 day, respectively, for low and high amplitudes. **b)** Load cycle shape and amplitude influence the lifetime of the passivation layer as shown for f_c=2 (where the effect of the cycle phase shift is weak).

a) Electron microscopic investigation of the intermetallic layer developed after 110 days at 700°C, exhibiting an oriented microstructure between 316L (left) and Al-12%Si (right). η and ξ domains are separated by a sharp phase boundary (center). Tangential cracks appear close to belts of porosity, on the Al-rich side of both large domains. Precipitates in the Al matrix (right) contain Fe, Si, and Ni (SEM-EDX). The total thickness of the intermetallic layer is 1520 µm. **b)** A 10-15 µm thick transformation zone is visible between steel and η, with a third porosity belt on the Al-rich side. **c)** Additional porosity is concentrated in a narrow region in the η phase, close to the boundary to ξ, τ precipitates are present on either side η-ξ boundary. **d)** Porosity within ξ increases gradually towards the interface with Al-12%Si.

List of tables

Nomenclature

Non-standard units

G...	Giga-unit prefix, 10^9
k...	Kilo-unit prefix, 10^3
M...	Mega-unit prefix, 10^6
r.u.	Polymeric repeat unit
T...	Tera-unit prefix, 10^{12}
toe	Ton-of-oil equivalent energy, $42 \cdot 10^9$ J
W_{th}	Watt-thermal

Acronyms

1-d	One dimensional
2-d	Two dimensional
3-d	Three dimensional
AA-CAES	Advanced adiabatic compressed air energy storage
aq.	Aqueous
BSE	Backscattered electron
B.C.	Boundary condition
CAES	Compressed air energy storage
CSP	Concentrated solar-thermal power
DSC	Differential scanning calorimetry
EBSD	Electron backscattering diffraction
EDX	Energy dispersive x-ray spectrometry
GEM	General materials diffractometer, Harwell Campus, UK
HV	Vickers hardness
I.C.	Initial condition
IEP	Isoelectric point
LH-TES	Latent heat thermal energy storage
NMR	Nuclear magnetic resonance spectroscopy
n-scattering	Neutron scattering/neutron diffraction
PCM	Phase change material

rms	Root-mean-square
r.u.	Polymeric repeat unit
SE	Secondary electron
SEM	Scanning electron microscopy
TES	Thermal energy storage
TOF	Time-of-flight
XRD	x-Ray diffraction
YSZ	Yttria stabilized zirconia

Chemical compounds

Alumina/Al_2O_3	Aluminum oxide
α-alumina	Aluminum oxide, corundum, hexagonal close-packed
$Al(iPrO)_3$	Aluminum iso-propoxide
AlN	Aluminum nitride
Al-12%Si	Eutectic aluminum-silicon alloy
Al-26%Cu-5%Si	Eutectic aluminum-copper-silicon
BN	Boron nitride
h-BN	Hexagonal boron nitride
CaO	Calcium oxide
Fe_2O_3	Iron (III) oxide
α-FeAl	Iron aluminum alloy
η-Fe_2Al_5	Iron aluminide
ξ	Iron chrome silicon aluminide
τ	Iron silicon aluminide
H_2O	Water, di-ionized
HNO_3	Nitric acid
iPrOH	Iso-Propanol
K_2O	Potassium oxide
MgO	Magnesium oxide
MnO_2	Manganese (IV) oxide
Na_2O	Sodium oxide
Na_2SiO_3	Sodium silicate
$nNa_2O.mSiO_2$	Non-stoichiometric sodium silicate

$pFe_2O_3.nNa_2O.mSiO_2$	Iron doped sodium silicate
P_2O_5	Phosphorous oxide
Si_3N_4	Silicon nitride
SiO_2	Silicon dioxide
SO_3	Sulfur oxide
TiO_2	Titanium dioxide

Arabic letters

A	Conceptual particle of the a-phase
	Heat exchange surface area
a_1	Yeremenko dissolution constant[1]
a	Generic aluminum phase
Bi	Biot number
Bi_2	Biot number in cycling calorimetry
b_1	Yeremenko dissolution exponent[1]
C_1	High corrosion cycle
C_2	Low corrosion cycle
c_p	Specific heat capacity at constant pressure
$c_{p,l}$	Liquid heat capacity
$c_{p,s}$	Solid heat capacity
$c_{p,f}$	Mean apparent heat capacity in the two-phase region
c_p^k	Heat capacity of k-th layer
$< c_{p,sl} >$	Expected effective heat capacity during melting/solidification
$c_{p,E}$	Encapsulation heat capacity
D_i^k	Diffusion coefficient of i in k
$D_{i,0}^k$	Preexponential factor of i in k
d_i^ν	Diffusion boundary layer width of particle i in phase ν
dV	Total volume differential
dV_i^ν	Partial volume differential of phase ν in layer i
dH	Enthalpy differential
dGi_2	Temperature intensity differential
E_ν	Kinetic energy of particle-wave

F	Conceptual particle of the f-phase
f	Generic iron phase
f_{c}	Charge-discharge cycle frequency
f_{pc}	Phase change frequency
f_{wt}	Weight fraction
Gi_2	Gradient integral
g_{b}	Boundary temperature gradient
g_1	First partial gradient
g_2	Second partial gradient
H	Enthalpy function
ΔH_i	i-th charge/discharge capacity
H_{f}	Total heat of fusion
$H_{(l)}$	Liquidus enthalpy
$H_{(s)}$	Solidus enthalpy
h_{f}	Specific heat of fusion in Jkg^{-1}
h_{f}^*	Apparent heat of fusion
$\hat{h}_{\mathrm{f}}$	Latent energy density
$h_{(l)}$	Mass-specific liquidus enthalpy
$h_{(s)}$	Mass-specific solidus enthalpy
J_i^{ν}	Volume transfer of species i in phase ν
$J_{\mathrm{F}}^{f\to\varphi}$	Volume transfer of F, from f to φ
$J_{\mathrm{A}}^{a\to\varphi}$	Volume transfer of A, from a to φ
K	Instrument factor
$\mathrm{K}_{\alpha,\mathrm{Cu}}$	Electron transition in Cu
k_{B}	Boltzmann constant, $1.3806 \cdot 10^{-23}\ \mathrm{Jmol^{-1}K^{-1}}$
k_p	Parabolic growth coefficient
k_p^*	Empirical growth coefficient
$k_{p,0}$	Pre-exponential growth coefficient
k_1	Yeremenko growth coefficient
k	Heat conductivity
$k^{a/f/\varphi}$	Heat conductivity in $a/f/\varphi$
k_l	Liquid heat conductivity

k_s	Solid heat conductivity
k_{ep}	Effective conductivity
L_z	Cylinder length
M_{w}	Molecular weight
m_{p}	PCM mass
m_{E}	Encapsulation mass
n^*	Empirical growth exponent
P_j	j-th model parameter
P^+	Charging power
P^-	Discharge power
P^+_{max}	Peak charging power
P^-_{max}	Peak discharge power
$\hat{p}_{\mathrm{f}}$	Charging power density
Q_{a}	Activation energy for layer growth
Q_{m}	Activation energy for atomic mobility
Q_{s}	Activation energy for dissolution
$\dot{Q}_{\mathbb{0}}$	Constant heat source at origin
$\dot{Q}_{\mathrm{b}}$	Boundary heat transfer rate
$<\dot{Q}_{\mathrm{b}}>$	Average heat transfer rate
Q_{min}	Minimum momentum transfer
$\hat{q}_{\mathrm{s}}$	Sensible energy density
R^2	Determination of fit parameter
R_{gas}	Gas constant 8.3141 $\mathrm{kJmol^{-1}K^{-1}}$
R_{h}	Ratio of hold duration
r_0	Initial radius of the a-f interface
r_{b}	Encapsulation boundary radius
r_{Γ}	Phase boundary radius
r_i	Interface radius
St_v	Stefan number
s_{m}	Molar entropy of melting
t	Time
Δt	Duration

t_0	Initial time
$t_{i,0}$	Begin of *i*-th storage event
$t_{0,\varphi}$	Incubation time of the iron aluminide reaction
T_0	Initial temperature
ΔT_b	Half-amplitude of cyclic boundary temperature
T_b	Boundary temperature
$\tilde{T}_\mathrm{b}$	Median boundary temperature
T_g	Glass transition temperature
T_m	Melting temperature
T_p	PCM temperature
T_w	Water temperature
T_i	Ice temperature
$T_{(l)}$	Liquidus temperature
$T_{(s)}$	Solidus temperature
T_m	Melting temperature
T_p	PCM center temperature
T_rm	Homologous temperature
T_∞	Wall temperature
$\dot{T}_\infty$	Heating rate
U_b	Total boundary heat transfer coefficient
u_surf	Surface heat transfer coefficient
u_b	Total heat transfer coefficient
u_1	Sample heat transfer coefficient
u_2	Device heat transfer coefficient
$V_{i,k}$	Volume of the *i*-th species in the *k*-th layer
w_0	Initial thickness
w_i	Thickness of *i*-layer
w_ν	Thickness of ν-layer
$w_{\varphi/\omega}$	Thickness of layer φ/ω-layer
w_min	Threshold thickness
x	First special coordinate, Cartesian
x_Γ	Phase boundary location

x_{SiO_2}	Atom fraction
ΔX_{Fe}	Stoichiometry range of Fe

Greek letters

β_A	Stoichiometric ratio
β_{br}	Peak broadening
Γ	Generic phase boundary
$\Gamma(t)$	Moving phase boundary
γ_f	First order constant for $\partial h_f/\partial \phi_F$
δ_i	Logarithmic quotient for particle i
δt	Time step
δx	Discretization length in x
ε	Half melting interval
θ	Bragg reflection angle
θ_Γ	Wetting angle
κ	Thermal diffusivity
λ_B	De Broglie wavelength
λ_N	Neumann coefficient
λ_P	Paterson coefficient
μ_c	Colloid viscosity
ν	Generic phase
π	Archimedes constant, 3.141593
ρ	Mass density
ρ^k	Density of k-th layer
ρ_{st}	Density 25 °C, 1 atm
σ_{h_f}	Standard deviation of h_f
τ_S	Scherrer grain size
ϕ_{Fe}^*	Apparent Fe concentration
ϕ_i^k	Volume fraction of i in k
$\phi_{i,eq}^k$	Volumetric equilibrium solubility of i in k
$\phi_{i,0}^k$	Preexponential solubility factor of i in k
φ	Generic intermetallic phase

Ω	Conceptual particle of the ω-phase
ω	Generic passivation layer phase

Operators

$\sim$...	Proportional to... / distributed according to...
Δ_{L}	Laplace operator
∂_t	Partial derivative in time
∂_x	Partial derivative in space
$\rho_{X,Y}$	Correlation function
σ_Y	Standard deviation of Y
χ^2	Maximum likelihood function
d	Total differential
Ei	Exponential integral function
erf	Error function
erfc	Complementary error function
exp	Exponential function
max( )	Maximum
min( )	Minimum
$\mathcal{N}$	Standard normal distribution

1

Chapter 1:
Latent heat thermal energy storage

1.1. Application potential

Management of energy sources is a central activity of the human society, from prehistoric collection of firewood for cooking to modern large-scale industrial processes. Global primary energy consumption has increased from negligible levels at mid-18th century to almost $1{,}4 \cdot 10^{10}$ ton-oil-equivalent (14 Gtoe) in 2017.[1] In the same time the human population was able to grow to close to $7 \cdot 10^9$ individuals, while expanding per capita availability of resources.[2] Predictions consider that, as this number grows to $9 \cdot 10^9$ by 2050[3], energy demand may fall in the range of 15 to 35 Gtoe.[4] Energy saving potential by promoting Thermal Energy Storage (TES) has been estimated close to 0.9 Gtoe in Europe alone.[5] Switzerland consumes a share of 20 Mtoe of which the Swiss industrial sector uses about 4 Mtoe.[6] Of this, process heat makes up for 2 Mtoe. Based on the European heat market statistics 40%[7] of process heat requires high-temperature (T>400 °C) resulting in an application potential of almost 1 Mtoe for high-temperature TES, in Switzerland alone.

Traditional forms of heat storage use the specific heat capacity (c_p) of a medium. They are referred to as sensible heat storage. Gases are seldom useful in this context as their low mass density translates into low energy density. Sensible heat storage media are often liquids or solids with high heat capacity or high density, or both. Storage density is a primary performance indicator of a storage medium. Another critical indicator is the rate at which energy can be stored and released. A storage medium

with desirable energy density, but severe heat transfer limitations may be useless. Heat transfer rates are therefore as important as energy density. Fundamental limitations for heat transfer come from the material properties, most notably, from the thermal conductivity (k). Beside favorable energy density and release rate, new technologies demand for heat storage with high exergetic efficiency, which entails operation at high temperature. Examples are thermo-mechanical electricity generation from concentrated solar irradiation, and Advanced Adiabatic-Compressed Air Energy Storage (AA-CAES).

Latent Heat TES (LH-TES) uses a Phase Change Material (PCM) which stores and releases heat during melting and solidification, respectively. Alloys with well-defined melting points by nature stabilize the exergy content of the heat output. This is of interest to industrial processes for power production[8] and storage.[9]–[11] Thereby, LH-TES is expected to play a significant role in advancing heat storage system performance.[11]–[13] A developing application is Concentrated Solar Power production (CSP). CSP currently depends on conventional TES technology to decouple electricity production from the solar irradiation schedule,[14],[15] and may further profit from advanced LH-TES.[16],[17] Similar advantages have been calculated for AA-CAES, where LH-TES has been estimated to improve roundtrip efficiency by 20 % to 70-75 %.[18]–[20] Additionally. supercritical carbon dioxide Brayton cycles are may also profit from LH-TES, based on their process temperatures in excess of 600 °C.[21]

1.2. Metal as latent storage medium

A characterizing aspect of thermo-mechanical power cycles is their desire to operate at the highest temperature that material properties permit. Currently, LH-TES with PCMs composed of Al, Si, Cu, Mg, Ca, among others have been identified as suitable candidates.[22],[23] The eutectic alloy of Al with Si (Al-12%Si), and the ternary eutectic of Al with Cu and Si (Al-26%Cu-5%Si) are stable to thermal decomposition, and form passivation layers when in contact with ambient oxygen. They offer a high heat uptake during melting, and facilitate heat release performance due to their excellent thermal conductivity.[23]

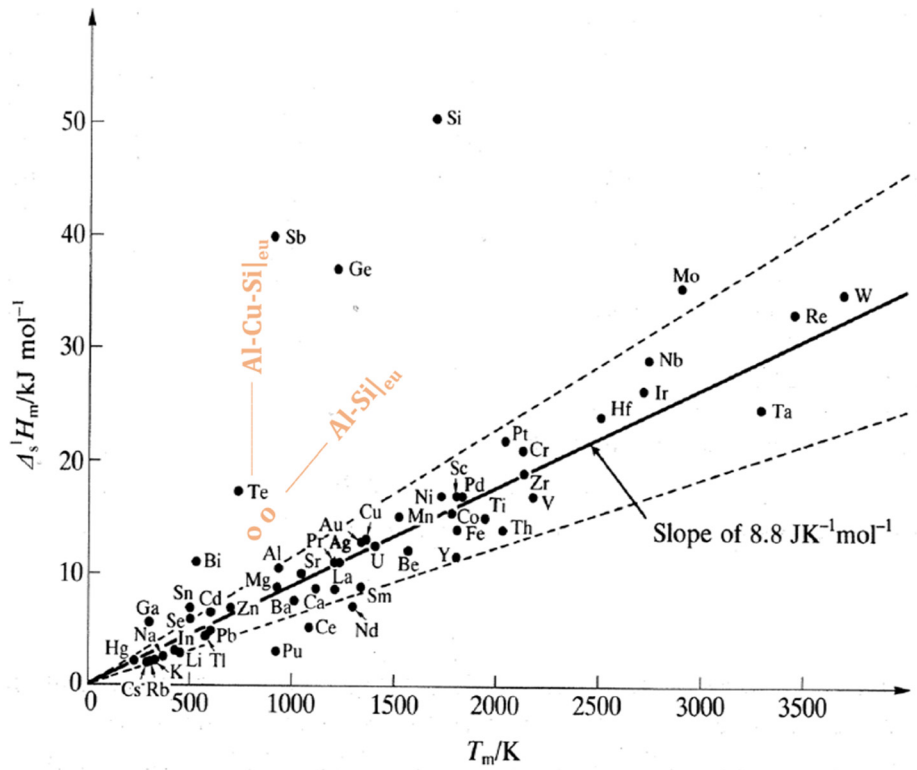

The distribution of elemental metals in the coordinate space of enthalpy of fusion (vertical axis) and melting temperature (horizontal axis). A linear trend sees many elements falling close to the line with slope 8.8 Jmol^{-1}K^{-1}. Figure modified and taken from [24].

Figure 1.1

The enthalpy of fusion (H_f) is defined as the heat uptake required to melt a given body of solid. If defined with respect to unit mass it is called the specific enthalpy of fusion (h_f), and has Si-units of Jkg^{-1}, although Jg^{-1} is often more convenient. h_f has been used as a critical property of PCMs for LH-TES applications, together with the melting temperature (T_m). Values of h_f for metals follow with few exceptions the Richards rule, which states that the molar entropy of melting (s_m) is close to 8.8 Jmol^{-1}K^{-1}, which are related by Eq.(1.1).

$$h_f = T_m s_m \frac{1}{M_w} \qquad \text{Eq.(1.1)}$$

The conversion factor M_w is the molar weight. This gives an important trend of higher energy density with increased storage temperature, and drives LH-TES research to further develop metal PCM systems with higher T_m.

Figure 1.1 compares metal and semiconductor elements with regards to Richards rule. It is noted that semiconductors such as Si, Ge, Sb, etc. require more heat to melt and fall outside of the +/- 30 % bounds. Si exhibits s_m four times larger than the Richard rule would predict, and would therefore be an attractive storage material with T_m of 1414 °C. Strong covalent bonding character of the semiconductor is responsible for the deviation from classical metal behavior. Alloys formed between Si with many metals, in particular Al, have a eutectic melting temperature significantly below the weighted average melting temperature of the constituents. For Al-12%Si the heat of fusion is relatively well estimated by a mass weighted rule of mixing, which makes it particularly interesting for LH-TES.

1.3. Molten metal corrosion

Al alloys as storage medium have been proposed at least since the 1980,[23] but haven't advanced to the application stage due to their corrosiveness in the molten state.[25] The emerging challenge is linked to the reactivity of the molten metal towards preferable encapsulation materials, such as steel.[26] Stabile encapsulations are necessary to protect the storage medium, and to preserve a constant heat exchange surface during the phase transition. Encapsulation materials ideally have a high thermal conductivity (see Figure 1.2). No single available containment material has allowed to harvest the fast and compact storage performance that would be possible when considering the metal PCM's intrinsic properties. Figure 1.3 shows the binary phase diagram of Fe with Al, and highlight frequently reported alloys and intermetallic compounds that are formed under relevant conditions for LH-TES (Table 1.1).

Table 1.1 Composition and density of selected phases from the Fe-Al diagram.[27]

Symbol	Formula	Al-range [at%]	Density ρ [kgm^{-3}]
α_2	FeAl	24-51	5583
ξ_0	$FeAl_2$	66-67	4330
η	Fe_2Al_5	71-73	4131
θ	Fe_4Al_{13}	75-76	3850

Since Birchenall and Riechman published on heat storage in eutectic alloys in 1980[23], many have taken up the material and noted its favorable phase change properties, i.e. conductivity, storage density, and suitable/adjustable T_m unrivaled by any salt. And same as 2007 Gasanaliev et al.[22], so does 2010 Kenisarin[11] conclude his review with a note on the importance of corrosion in the system that does not suggest the problem has been resolved. Kenisarin's concluding remarks feature a single experimental study that investigates metal PCM in close contact with the intended encapsulation material, during 1000 cycles where thermo-physical properties were continuously monitored by transferring an aliquot of the PCM to a Differential Scanning Calorimetry (DSC) apparatus. Most recently, in 2018, Wei et al.[25] repeated the demand for corrosion mitigation and added the notion that cyclic stability testing has to be established for PCMs, as it is standard in other fields.

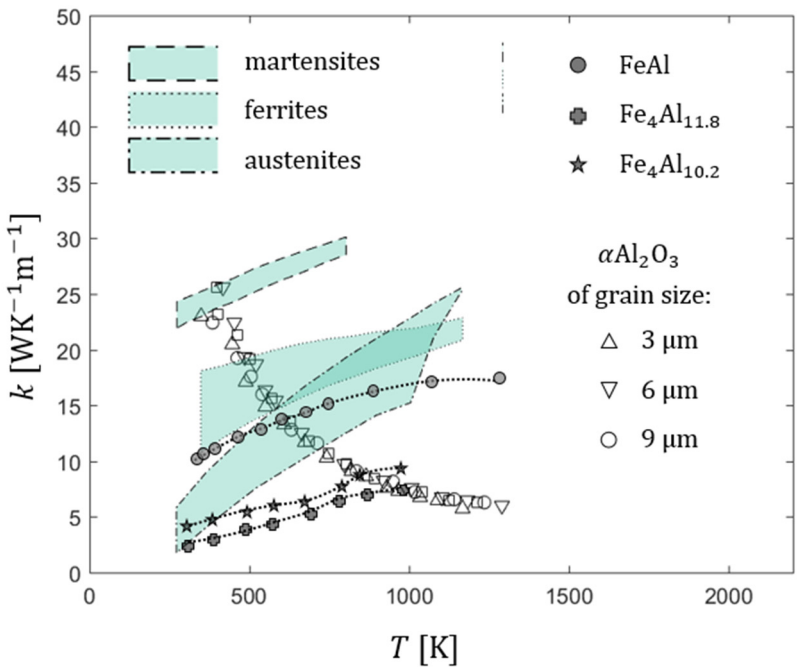

Thermal conductivities of selected materials over a wide temperature range. Data collected from [28]–[30]. Figure 1.2

1

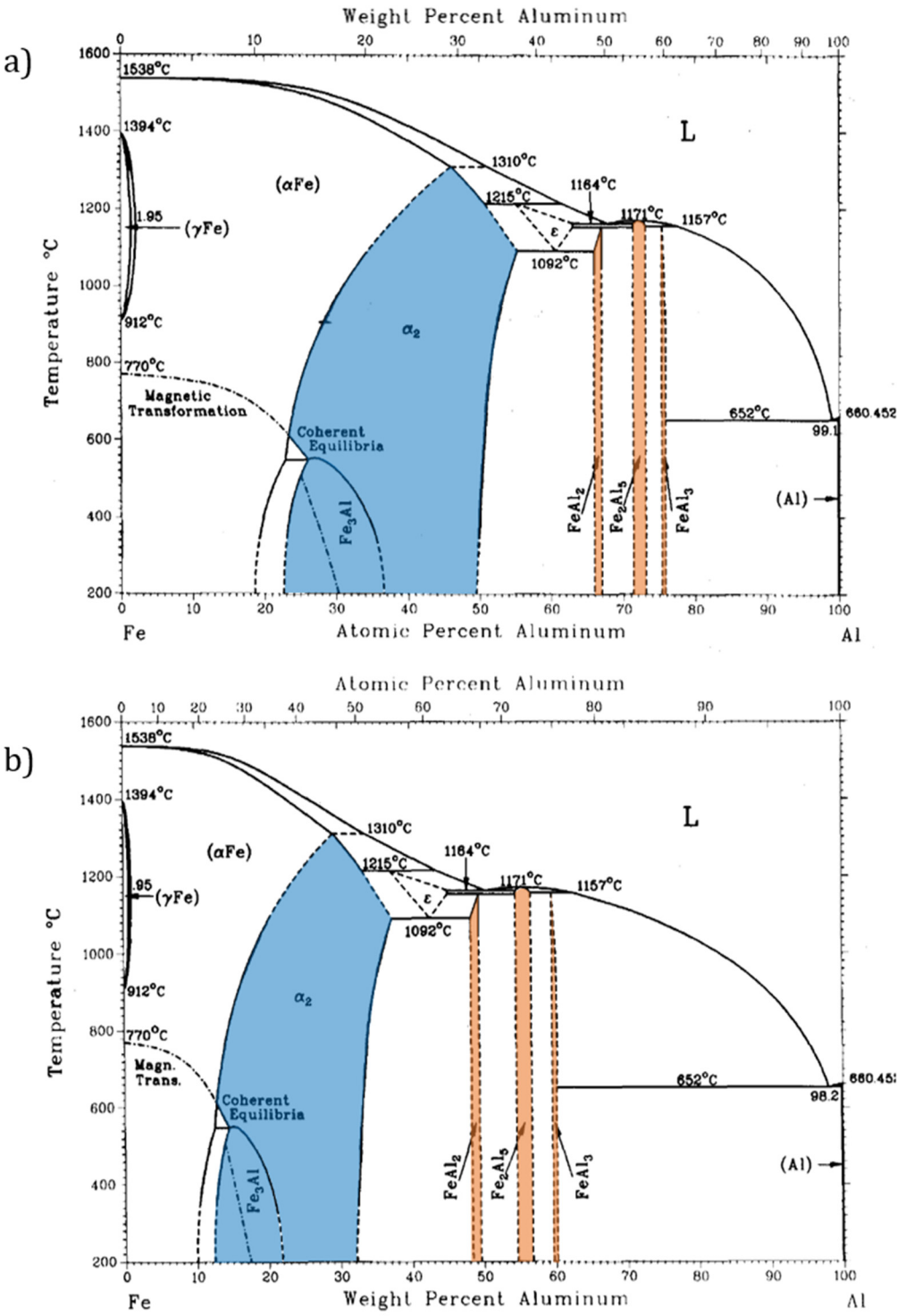

Figure 1.3 Phase diagrams of Fe-Al scaled to atomic **(a)** or weight **(b)** composition. Highlights indicate frequently observed phases in the context of this work. Blue indicates ranged composition, while red indicates stoichiometric compounds. Figure modified and taken from [31].

1.4. Thesis outline

The aim of this thesis is to contribute to the viability of highly desirable metal PCM systems by addressing the following objectives: (A) to elucidate the mechanism of performance degradation associated with molten metal corrosion, (B) to propose and develop mitigation strategies that allow stable operation, (C) to characterize the performance of encapsulated PCM units experimentally and on application relevant scale, and (D) to contribute to the development of a scientific framework for performance and stability evaluation of encapsulated PCM units.

Objective (A) is approached in the following Chapter 2. It contains a review of the important mass transfer models of intermetallic layer growth for the Al-Fe system. Besides being a promising PCM material, liquid aluminum is an active corrosion medium, which dissolves up to 3 % Fe, and 9 % Ni at 750 °C. Further exists an ongoing scientific debate about the reaction conditions governing the formation rates of various iron aluminides. We experimentally explore the operation of stainless-steel capsules with Al and its alloys as PCM. Experimental design is directed towards the investigation of the reactivity and dissolution of encapsulation elements in the molten PCM. Cylindrical test capsules made of stainless steel contained the molten PCM during prolonged exposure to a set of assumed operation temperatures. Iron aluminide formation on the interior capsule surface is quantified, and used to estimate impacts on heat storage performance. Characterization is carried out by Scanning Electron Microscopy (SEM), Energy Dispersive X-ray (EDX) spectrometry, DSC, and Vickers Hardness (HV) micro-indentation. Finally, an efficient numerical model is used to predict the storage performance including degradation into the future, up to 8760 full-load-hours. This is then used to propose design guidelines for encapsulations with good long-term performance stability.

In Chapter 3 diffusion barrier coatings derived from ceramic particle suspensions and deposition methods thereof are developed, addressing (B). Focus is put on expanding the range of viable storage unit dimensions and thereby foster even higher heat release rates. The α-modification of aluminum oxide (α-alumina) is known to be thermodynamically inert to molten aluminum up to 1500 °C.[32] Silicon nitride (Si_3N_4) reacts to form a stable passivation layer of aluminum nitride (AlN).[26] Finally, boron nitride (BN) has been proposed to avert its conversion kinetically as the thin layered hexagonal crystals are very slow wetting and AlN formation at the interface reducing

the observed reactivity.[33] A challenge was identified in providing a suitable binder phase, and deposition thereof as homogeneous and well adherent coatings. Stable particle suspensions with iso-propanol (iPrOH) or deionized water (H_2O) were obtained by adjusting the pH to modify the electrostatic particle interactions. Binders were derived from aluminum isopropoxide ($Al(iPrO)_3$), or sodium silicate (Na_2SiO_3). Coatings were characterized by SEM imaging of cross-sections on Si wavers, and of cross-sections and top-view microstructures on stainless steel substrates. EDX and DSC were again employed, probing the chemical composition and thermo-physical properties of the PCM after prolonged exposure of the coated cylinder to the liquid metal. BN based coatings were confirmed to suppress inter-diffusion for several weeks, prevented 90 % of the capacity loss occurring in the control group, in a scaled-up pilot experiment with a total of 200 MJ latent heat capacity in encapsulated Al-26%Cu-5%Si.

Objective (C) is the focus of Chapter 4, where storage performance of coated and uncoated PCM capsules under repeated load cycles are evaluated and discussed. A novel method for the calorimetric analysis of the PCM unit's performance is presented and important insights on solidification behavior and heat transfer are discussed. With regard to the developed coatings, the cyclic load conditions represent an important test with increased severity. We show that the performance and stability can be monitored during cyclic testing by evaluating the variation of heat flow calculated from carefully placed temperature measurements. The method is derived with regard to reported and confirmed difficulties of PCM performance assessment via conventional DSC measurements.[34]–[37] The temperature dependent enthalpy of an encapsulated PCM storage may change during operation due to chemical interactions not only with the interface, but through contaminations from the gas phase. Both can lead to a change in the PCM's solid density making the extrapolation of mg-sized DSC samples to storage performance difficult. Additional insight comes from comparison of temperature gradients with a numerical model, allowing characterization of the evolution of the transfer resistance at the PCM-encapsulation interface. In the case of intermetallic layer deposition, increased transfer resistance has a negative impact on LH-TES performance. We show that the developed cyclic testing approach is crucial to the field of LH-TES by presenting high frequency load cycles that permit stable operation without diffusion barrier. Results from validated

heat modelling which were used in the design of a 1.4 MJ lab scale prototype storage are appended.

The conclusions in Chapter 5 summarize and crosslink the obtained insights. Objective (D) is addressed throughout all Chapters.

1

2

Chapter 2:
Degradation management

Material from this chapter was accepted for publication, 13 April 2019: S. Binder, S. Haussener, Design guidelines for Al-12%Si latent heat storage encapsulations to optimize performance and mitigate degradation, Applied Surface Science (2019) (https://doi.org/10.1016/j.apsusc.2019.143684).

2.1. Introduction

The interface reaction forming iron aluminide in pure and alloyed systems has been studied in the context of aluminum processing,[27],[38] iron-aluminum part joining,[39] diffusion bonding,[40] preparation of advanced composites,[40] refractory coatings by hot dip aluminizing,[40] permanent mold casting,[41] and high-temperature and high-strength material with good oxidation resistance.[42]–[45] Recently, iron aluminide formation has been identified as corrosion mechanism in high-temperature TES systems which use steel-encapsulated metal PCM.[8],[46] In such systems, the PCM serves to store and release heat with a high energy density, which is associated with h_f of the solid-liquid transition. PCM-TES inherently stabilizes the discharge temperature of the stored heat near T_m of the PCM alloy. Examples of technologies featuring metal PCM-TES systems are found in, but are not limited to, CSP production[8] and AA-CAES.[12],[47]–[49] In the case of AA-CAES, the implementation of a suitable thermal storage has the potential to increase electricity storage round-trip efficiency from 40-55 % in conventional CAES to 60-75 % in AA-CAES.[47] Adapting a more general perspective, energy saving potential by thermal energy storage in Europe has been estimated to be 1.2 TW_{th} under a 10-year implementation scenario.[5] PCM-TES is expected to play a significant part in this scenario by contributing to advanced heat storage system performance.[11]–[13]

Aluminum alloys are a low-cost option for metallic PCM and suitable alloys have been identified and listed.[23],[50] Al-12%Si offers a large heat of fusion, good thermal conductivity, low tendency for under-cooling, and a melting temperature (see Table 2.1) suitable for heat-to-work conversion processes. The main obstacle to exploiting aluminum alloys is their reactivity towards encapsulation materials, which results in conversion of latent storage material to non-melting aluminides. In applications such as AA-CAES and CSP, a strong focus lies on economy of scale and rigorous system optimization before practical implementation is needed. Precise forecasting of performance evolution is essential to determine design and operational parameters. Reliable dynamic and quantitative modelling of mass transport and the conversion of phase change material to non-functional intermetallic phases is crucial for the economic assessment. Studies investigating PCM/encapsulation stability and compatibility have assessed the storage/release cycling stability of metals via DSC measurement of h_f.[51]–[56] Sun et al. have exposed Al-34%Mg-6%Zn to melt/solidification cycles while in contact with pieces of steel sheets. [51] They found a reduction of the mass specific heat of fusion of 11% over 1000 cycles. In some cases, the formation of intermetallic compounds at the encapsulation/PCM interface have been observed but the effect on the systems heat storage capacity has not been quantified or modelled.

Below 800 °C, elemental iron (Fe) can incorporate up to 23 at% aluminum (Al) in solid solution. Two intermetallic compounds with the nominal composition Fe_3Al and FeAl coexist below 460 °C when the Al content is further increased. Above 460 °C FeAl replaces the other compound completely. This compound has a temperature-dependent thermal conductivity typical of ferrous alloys and exists in a compositional range of 23 to 51 at% and up to 1310 °C. At higher Al concentrations, three intermetallic compounds with narrow stoichiometric existence domains ($\Delta X_{Fe} < 3$ %) are observed: $FeAl_2$, Fe_2Al_5 (η), and $FeAl_3$. In pure and low alloyed systems, the η-phase has been predominantly identified. At least 8 ternary phases have been distinguished if silicon (Si) is added to the system.[57] Among these, there is the monoclinic modification with the nominal composition $Al_{63.5}Fe_{20.5}Si_{16}$ (τ). Quaternary phases which further include Cr have been characterized more recently to exist in a compositional range of 70-76at% Al, 6-13at% Fe, 8-16 at% Si, and 3-11at% Cr (ξ).[58]

Experimental studies of formation kinetics at the interface of liquid aluminous alloys and solid iron or steel have been typically employing metallographic cross sectioning. Kinetics have been quantified over the range of hours.[40],[41],[43],[59]–[63] The growth of a homogeneous, flat interface layer by inter-diffusion is limited by its own thickness (w) and follows the differential Eq.(2.1).

$$\frac{\mathrm{d}w}{\mathrm{d}t} = \frac{k_p}{w} \qquad \text{Eq.(2.1)}$$

Eq.(2.1) is found by considering Fick's 1st law of diffusion and is readily solved when the parabolic growth coefficient (k_p) is considered constant, i.e. for a fixed temperature and concentration within the layer:[64]

$$w(t) = \sqrt{2k_p(t - t_0) + {w_0}^2} \qquad \text{Eq.(2.2)}$$

Eq.(2.2) is the basis for calculation of k_p from constant temperature experiments. The thickness of the layer after an initial transient growth phase (w_0), and the time after which the layer growth is diffusion controlled (t_0), have been assumed to be small compared to the scale of the respective measurements, so that Eq.(2.2) is well approximated by Eq.(2.3).[40],[62]

$$w(t) = \sqrt{2k_p t} \qquad \text{Eq.(2.3)}$$

Temperature-dependent diffusion in the compound layer affects k_p, which has been accounted for by thermal activation term.[62],[59],[63]

$$k_p = k_{p,0} \cdot e^{-\frac{Q_\mathrm{a}}{R_\mathrm{gas}T}} \qquad \text{Eq.(2.4)}$$

Eq.(2.4) includes a pre-exponential factor for parabolic layer growth ($k_{p,0}$) with the same units as k_p, the corresponding activation energy for layer growth (Q_a^t), and the gas constant (R_gas), and the absolute temperature (T).

Reported experiments on iron aluminide formation kinetics have been interpreted using Eq.(2.1) to (2.4) or variations thereof.[27],[40],[43],[51],[59]–[64] Bouche et al. immersed Fe samples in molten Al and described the layer growth with Eq.(2.3), within the period of measurement (30s to 3600s).[40] They have ascribed the existence of a Fe_2Al_5 layer with a width of $w_0(t_0$=30 s)=140 µm to a short transient initial phase, and subtracted w_0 and t_0 from the respective experimental data before evaluating k_p.

Bouayad et al. calculated apparent activation energies of 73 kJmol^{-1} for Fe_2Al_5 in the solid iron/liquid aluminum system.[62] Springer et al. characterized the temperature dependence of the same phase in a system with low carbon steel and calculated an activation energies of 190 and 17 kJmol^{-1}, with the first value referring to the interaction with pure aluminum and the second to Al-5at%Si.[59] Yin et al. have determined activation energies for k_p by systematically varying temperature and Si concentration in the melt. They immersed iron specimens in molten aluminum containing 0, 0.5%, 1.0%, 1.5%, 2.0% and 3.0% of Si and found activation energies for the growth of Fe_2Al_5 of 207, 186, 169, 168, 167 and 172 kJmol^{-1}, respectively.[63] Pasche et al. used x-ray micro-tomography and digital image threshold integration to resolve the ab initio microstructural evolution for pure Fe-Al[1,2]. They fitted Eq.(2.2) to the experimental layer growth within two separate domains and found best agreement when choosing the time of transition from fast to slow growth to be t_0=2500 s. The corresponding range-dependent parabolic growth constants ($k_{p,1}$, and $k_{p,2}$) were $4.4 \cdot 10^{-12}$ m^{2}s^{-1}, and $4.0 \cdot 10^{-13}$ m^{2}s^{-1}, respectively. They suggested a change in growth mechanism, with a nucleation-controlled initiation phase, with a transition phase where growing features coalesce and densify, and a final bulk growth phase. Other authors pragmatically account for the faster initial growth compared to the purely diffusion-controlled mechanism by fitting data to a variation of Eq.(2.2) with adjustable exponent.

Eq.(2.5)
$$w(t) = \sqrt{2k_p^*} \cdot t^{n^*}$$

In this approach, the empirical growth coefficient (k_p^*) looses any analytical link to diffusion parameters. Values for the growth exponent (n^*) have been reported between 0.45 for pure aluminum/pure iron at 771 °C, to 0.49 for low-alloyed steel and iron saturated melt at 786 °C.[62] An analytic analysis of the intermetallic layer thickness between solid Fe and liquid Al was presented by Yeremenko et al. [64].

Eq.(2.6)
$$\frac{\mathrm{d}w}{\mathrm{d}t} = \frac{k_1}{w} - a_1 \cdot e^{-b_1 \cdot t}$$

Eq.(2.6) includes an exponentially decaying dissolution term, where k_1, a_1, and b_1 are physically motivated lumped parameters. This model has allowed making qualitative predictions about intermetallic layer formation kinetics, such as the existence of a steady state layer thickness, in a case where layer growth is stably balanced by

dissolution between two semi-infinite media. Then, intermetallic layer thickness does not increase at the cost of a constant dissolution rate. This is not likely or acceptable for PCM-encapsulation system, and neither transient boundary condition, nor an exact analytic solution have been presented.

Heat storage applications vary the temperature of the storage medium during the charge and discharge process. Dynamic variability of temperature at which diffusion takes place is a prerequisite in order for an intermetallic layer growth model to be useful as a tool to predict PCM storage capacity and performance. The presented models lack this capability due to ill-defined regime limitations of non-physical exponents, which are presumably temperature dependent. Most intermetallic layer growth models are based on the evaluation of data acquired over the duration of seconds to hours only.[42],[43],[45] In contrast for PCM-TES applications, the evaluation of the solid encapsulation integrity and the storage capacity needs to be predicted for a significant part of the lifetime. Models are thus required, which accurately predict the growth of intermetallic layers on the scale of month to decades. Here, we present experimental data on Al-12%Si encapsulated in high-temperature stainless steel ANSI 316L (316L) over the duration of 120 days at 700 °C, and 100 days at 600 °C. The developed mass-transfer model for intermetallic layer growth and dissolution fits experimental data on this time scale. Physical model parameters allow the prediction of important performance factors over a large range of relevant operating and design conditions. Strategies for effective and practical PCM-TES systems are proposed.

2.2. Experimental methodology

2.2.1. Synthesis and measurements

Experiments consisted of encapsulating Al-12%Si in 316L cylinders and holding it in the molten state at constant temperature for up to 120 days (Figure 2.1). Casting grade Al-12%Si alloy was obtained (Reinhold Frei AG, Switzerland) with the wet chemical elemental analysis provided by the supplier (see Table 2.1). Our DSC and micrographic analysis confirmed the slightly hyper-eutectic composition. Segments of 60 mm length of 316L cylinders, 21.3mmx2.65mm (outside diameter and wall thickness), were filled with Al-12%Si by direct casting and closed with standard threaded steel caps. A box furnace (Borel, TL 1100) with constant temperature control heated a batch of 21 specimens to 700 °C. Additional temperature measurements with a K-type thermocouple confirmed similar and constant temperature around the samples in a distance of 5 mm from the surface. Deviations from the set point were below 1 °C, after the furnace had equilibrated for 60 minutes. Individual samples were removed and quickly cooled down at shorter intervals during the initial phase, i.e. the early stages of reaction in the system. Swift removal of samples minimized heat loss, and measured air temperature within the furnace never dropped by more than 20 °C. The temperature generally stabilized within seconds after closing the furnace.

2.2.2. Characterization

Cross-section micrographs perpendicular to the cylindrical axis at half tube height (30 mm) were polished to a grit 2500 paper and examined via optical microscopy (Olympus ZYC Binocular). Digital macro imaging was carried out with a custom stage, macro lens (3.2x magnification), and a digital camera with autofocus (Samsung Galaxy S5, 16 MP). The outside diameter of each specimen was measured twice with a mechanical caliper (accuracy: 10 μm), and the average served as image calibration reference for the cross-sectional images of the same sample. The standard deviation of the outside diameter over 21 tubes was 54 μm, and their average 21.19 mm. This variation led to an error from false calibration of 0.3 %, if assumed to be random and independent. Similarly, the error from unbiased reading of the caliper

was below 0.1 %. The thickness of the intermetallic layer at the steel/Al-12%Si interface was calculated by manual pixel selection and conversion to physical units using the outside diameter as calibration reference. The resolution of 16 megapixel led to a pixel size in the calibrated image of 10-12 µm, depending on working distance. For the largest measured layer thicknesses (approximately 1.6 mm) the relative and absolute errors added up to 18 µm for a single measurement. Twelve independent measurements were obtained from every cross-section. Measurements were distributed evenly around the circumference of the cross-section (see Figure 2.1). The cumulative error including calibration, substrate variation, and image resolution was calculated to be below 6 µm, following a Gaussian error propagation formalism.[65]

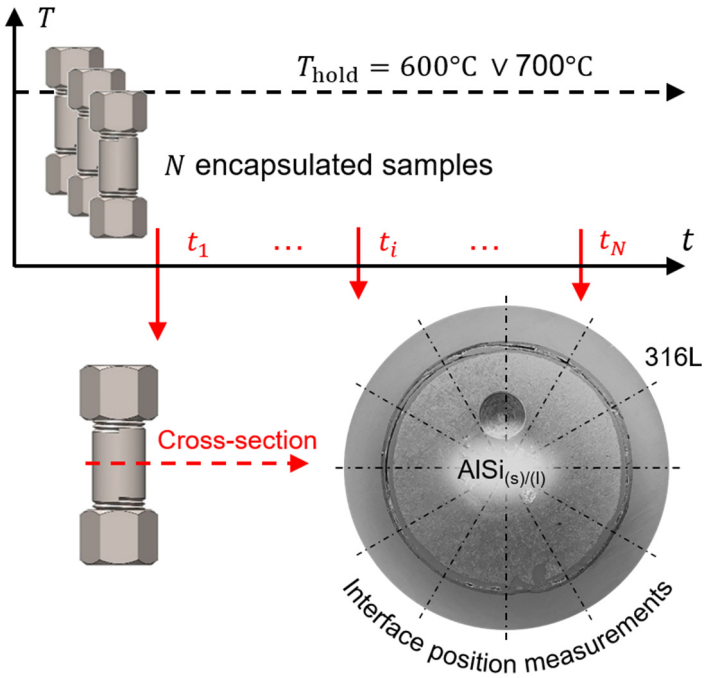

Schematic of the experimental procedure. encapsulated Al-12%Si cylinders were brought to reaction temperature (600 °C or 700 °C), with subsequent cooling. Metallographic section at the mid plane reveals of an intermetallic layer at the interface. Samples for DSC analysis of T_m and h_f were taken at the polished cross-section (circular hole in the upper half). Figure 2.1

SEM imaging was carried out at the interdisciplinary center for electron microscopy (CIME, EPFL, Switzerland). Images were obtained up to 5000x magnification (Zeiss, Merlin with Gemini column) with both Secondary Electron (SE) and Backward Scattering Electron (BSE) detection. The composition of the present phases was

investigated via EDX. Line-scans were carried out in radial direction across the intermetallic layer. Phase compositions were calculated as average of at least 10 independent point measurements, per cross-section and phase. Phase transformation temperatures and heats of fusion were obtained by DSC (NETZSCH Pegasus F1 404, 10 K/min), between 400 °C and 700 °C (3 cycles). Samples for DSC were obtained by drilling into the metallurgical cross-section and collecting the turnings. Preparation of monolithic samples additionally confirmed that surface oxidation had no influence on the measured value of h_f. Rough surfaces were polished on a 600-grit silicon carbide paper to optimize thermal contact to the sintered alumina pan. In both cases, the total mass per sample was kept between 15 and 25 mg. Three independent samples were measured from every disc, distributed evenly between the center and the periphery in radial direction. From the resulting 9 values (3 samples, 3 DSC cycles each), average h_f values and respective standard deviations (σ_{h_f}) were calculated.

Table 2.1 Thermal and physical properties of eutectic aluminum-silicon binary alloy and steel encapsulation. Properties are measured by: §wet-chemical analysis, *SEM-EDX (in this work), **DSC (in this work).

	Al-12%Si	316L / 1.4404
Measured composition, [at%]	86.5Al-12.9Si-0.4Fe-0.3Mn§	67.9Fe-18.4Cr-9.6Ni-1.5Mo-1.1Mn*
Eutectic composition, [at%]	87.8Al-12.2Si[66]	
Melting temperature, T_m [°C]	574** (576[52])	-
Heat of fusion, h_f [Jg^{-1}]	462** (560[52])	-
Solid heat conductivity, k_s [$WK^{-1}m^{-1}$]	180[23]	16[67]
Liquid heat conductivity, k_l [$WK^{-1}m^{-1}$]	70[23]	-
Solid heat capacity, $c_{p,s}$ [$JK^{-1}g^{-1}$]	1.038[52]	0.5[67]
Liquid heat capacity, $c_{p,l}$ [$JK^{-1}g^{-1}$]	1.741[52]	-
Standard density, $\rho_{st.}$ [kgm^{-3}]	2700[52]	8000[67]

2.2.3. Modelling

The experimentally investigated system was modelled as concentric cylinder slabs consisting of two reactive phases, representing the Al-12%Si (a) and 316L (f).

The center of the a-phase consists purely of A-particles, while the f-phase consists purely of F-particles. The intermetallic layer formed by their reaction was treated as homogeneous phase (φ) with volumetric composition $\phi_{\mathrm{A}}^{\varphi}$=1-$\phi_{\mathrm{F}}^{\varphi}$. A layer of Ω-particles forms a passivation layer (ω), which is soluble in a and has a thickness (w_{ω}). Chemical equilibrium at the interface plane of neighboring phases is rapidly reached, compared to the rate of transport across the layer. We adapted a volumetric frame of reference with constant atomic density, so that the total volume differential for each type of particle ($\mathrm{d}V_i$) remained equal to zero (Eq.(2.7)).

$$\mathrm{d}V_i = \mathrm{d}V_i^a + \mathrm{d}V_i^{\omega} + \mathrm{d}V_i^{\varphi} + \mathrm{d}V_i^f = 0 \qquad \text{Eq.(2.7)}$$

The initial radius of the PCM-encapsulation interface (r_0) is used as constant point of reference (Figure 2.2). The evolution of φ is described by the migration of its lower and upper bounding radius (r_1 and r_2) over time. The radius of the outer surface of the steel (r_3) remains constant.

It is convenient to also define the width of the intermetallic layer (w_{φ}), as well as the partial terms representing the width of converted PCM (w_1) and encapsulation (w_2) respectively (Eq.(2.8)).

$$\begin{aligned} r_1(t) &= r_0 - w_1(t) \\ r_2(t) &= r_0 + w_2(t) \\ w_{\varphi} &= w_1 + w_2 \end{aligned} \qquad \text{Eq.(2.8)}$$

The dissolution rate of ω ($\mathrm{d}V_{\Omega}^{\omega}/dt$) is limited by diffusional transport of Ω (J_{Ω}^{d}, superscript d for dissolution) across the width of the diffusion boundary layer (d_{Ω}^{a}) in a, Eq.(2.9).

$$J_{\Omega}^{\mathrm{d}} = -D_{\Omega}^{a}\frac{\phi_{\Omega,\mathrm{eq}}^{a} - \phi_{\Omega}^{a}}{\delta_{\Omega}} \cdot (2\pi L_z), \text{with } \delta_{\Omega} = \ln\frac{r_1}{r_1 - d_{\Omega}^{a}} \qquad \text{Eq.(2.9)}$$

J_{Ω}^{d} is proportional to the under saturation of Ω in a ($\phi_{\Omega,\mathrm{eq}}^{a}$-$\phi_{\Omega}^{a}$) and the diffusion coefficient of Ω in a (D_{Ω}^{a}). As d_{Ω}^{a} is small compared to r_1, the unitless logarithmic quotient δ_{Ω} tends towards zero, which must be dealt with numerically by choosing the time step carefully. We choose the cylinder length to be unity (L_z=1 m). Diffusion of A and F within ω and Ω in φ are low. φ starts to form rapidly when ω approaches dissolution ($w_{\omega} \to 0$). w_{φ}^2 is instantly large compared $D_{\Omega}^{\varphi}t$ so that after the initiation of degradation de-passivation becomes irreversible. Figure 2.2c) shows the

continuous transition from passivation to intermetallic layer growth around the time $t_{0,\varphi}$.

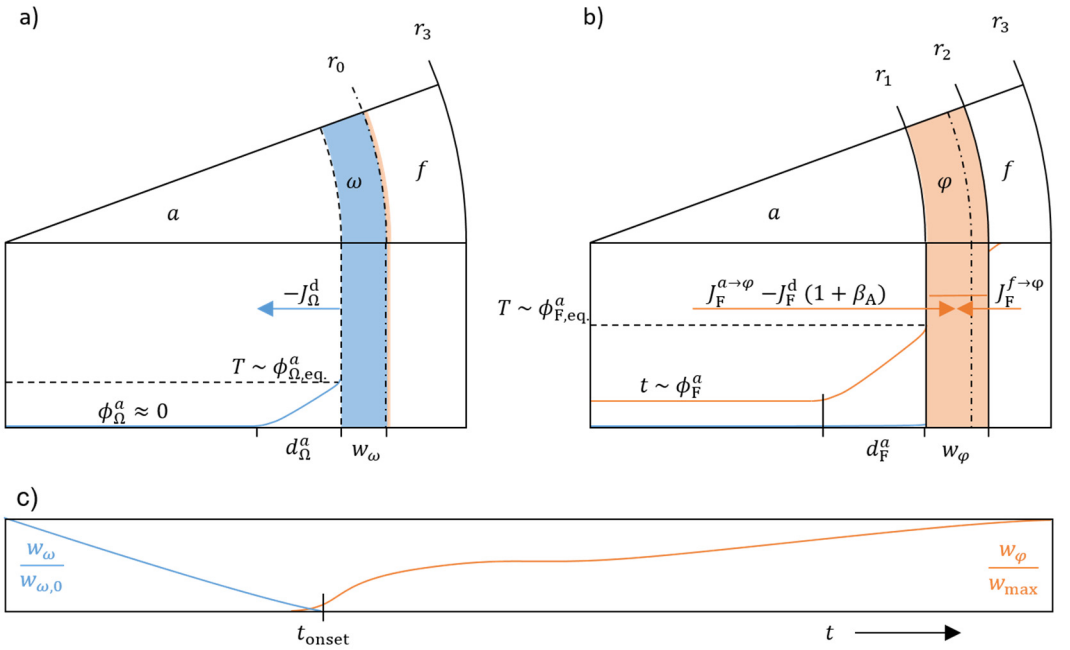

Figure 2.2 **a)** Section of the cylindrical model domain, before the onset of iron aluminide formation. Presence of a layer of ω efficiently suppresses cross-diffusion of A and F. Its dissolution proceeds approximately linear in time ($J_\Omega^d \approx$ constant). The initial interface position (r_0) is indicated by a dash-dot line. **b)** Growth of φ starts when w_ω approaches complete dissolution. **c)** Illustration of the continuously modelled temporal domain with y-axis the normalized layer thickness and the x-axis the time. $t_{0.\omega}$, marks the time when cross-diffusion and formation of φ become appreciable, defined by a threshold of 2 µm.

For the dissolution of φ, we treated d_F^a similar to Eq.(2.9). However, the concentration of F in a (ϕ_F^a) can approach the temperature-dependent saturation concentration ($\phi_{F,eq.}^a$), therefore the transport of F through δ_F (J_F^d) is given by Eq.(2.10).

Eq.(2.10)
$$J_F^d = -D_F^a \frac{\phi_{F,eq}^a - \phi_F^a}{\delta_F}\,(2\pi L_z), \text{with } \delta_F = \ln\frac{r_1}{r_1 - d_F^a}$$

The corresponding diffusivity of F in a (D_F^a) is treated as constant with regard to ϕ_F^a. The growth of φ is limited by the diffusion of A from a to φ ($J_A^{a\to\varphi}$), as well as the diffusion of F from f to φ ($J_F^{f\to\varphi}$). Using the rule for a network of resistors in series gives the limiting volume flow terms:

$$J_{\mathrm{A}}^{a\to\varphi} = \left(\frac{\delta_{\mathrm{A}}}{D_{\mathrm{A}}^{a}} + \frac{\delta^{\omega}}{D_{\mathrm{A}}^{\omega}} + \frac{\ln(r_c/r_1)}{D_{\mathrm{A}}^{\varphi}} + \frac{\ln(r_2/r_c)}{D_{\mathrm{F}}^{\varphi}} \cdot \beta_{\mathrm{A}}\right)^{-1} \cdot \left(\phi_{\mathrm{A,eq}}^{\varphi} - \phi_{\mathrm{A}}^{a}\right) \cdot (2\pi L_z)$$
$$\text{with } \beta_{\mathrm{A}} = \left(\frac{\phi_{\mathrm{A}}^{\varphi}}{\phi_{\mathrm{F}}^{\varphi}}\right), \delta^{\omega} = \frac{r_1 + w_{\omega}}{r_1}, \text{and } r_c = \frac{r_1 + r_2}{2} \qquad \text{Eq.(2.11)}$$

The volumetric stoichiometry ratio (β_A) ties together $J_{\mathrm{A}}^{a\to\varphi}$, and $J_{\mathrm{F}}^{f\to\varphi}$, as well as $J_{\mathrm{A}}^{\mathrm{d}}$ and $J_{\mathrm{F}}^{\mathrm{d}}$, so that the initial stoichiometry of φ ($\phi_{\mathrm{A,eq}}^{\varphi} = 1 - \phi_{\mathrm{F,eq}}^{\varphi} = 0.779$) is conserved. Diffusion boundary layers within the liquid a were assumed to stabilize instantaneously as the interface adapts its dynamic equilibrium velocity.[64] The width of Fe pooling zone inside unsaturated Al melt has been determined to be 3.2 µm at 800 °C, respectively.[60] We lumped the temperature dependence of diffusion boundary layers into the Arrhenius relation for diffusion and assume a constant pre-exponential contribution for A, F and Ω ($d_{\mathrm{F}}^{a} = d_{\Omega}^{a} = 2$ µm).

$$J_{\mathrm{F}}^{f\to\varphi} = J_{\mathrm{A}}^{a\to\varphi} \cdot \frac{1}{\beta_{\mathrm{A}}}, \text{with } J_{\mathrm{A}}^{\mathrm{d}} = \beta_{\mathrm{A}} \cdot J_{\mathrm{F}}^{\mathrm{d}} \qquad \text{Eq.(2.12)}$$

By combining Eq.(2.7) to (2.12), the volume rate balance is defined. Figure 2.2 illustrates the volume rate balance for ω and φ in terms of the incoming and outgoing volume flows. Flows contributing to the formation or dissolution of φ depend on w_{ω}, w_{φ}, ϕ_{F}^{a}, $\phi_{\mathrm{F,eq.}}^{a}$, and vice versa.

Temperature-dependent diffusivity of the i-th species inside the k-th phase is estimated using an Arrhenius type law, given by Eq.(2.13).

$$D_i^k = D_{i,0}^k \cdot e^{\frac{-Q_{\mathrm{m}}}{R_{\mathrm{gas}}T}} \qquad \text{Eq.(2.13)}$$

The activation energy for mobility (Q_{m}), and the pre-exponential factor ($D_{i,0}^k$) were optimized for A and F in a and φ, and for Ω in a. We further used Eq.(2.14) for the temperature-dependent equilibrium solubility of F and Ω in a ($\phi_{\mathrm{F,eq}}^{a}$ and $\phi_{\Omega,\mathrm{eq}}^{a}$).

$$\phi_{i,\mathrm{eq}}^{k} = \phi_{i,0}^{k} \cdot e^{\frac{-Q_{\mathrm{s}}}{R_{\mathrm{gas}}T}} \qquad \text{Eq.(2.14)}$$

The activation energy for solubility (Q_{s}), and the pre-exponential solubility factor (ϕ_0), where optimized for F and Ω in a. The evolution of the partial volume ($V_{i,k}$) was calculated according to the explicit finite difference method for a 1-dimensional domain, described in [68], corresponding to Eq.(2.1), and subsequent recalculation of r_k, w_k, and $\phi_{i,k}$, as well as the temperature dependent properties D_i^k, and $\phi_{i,\mathrm{eq}}^{k}$.

Eq.(2.15)
$$V_{i,k}\big|_{\mathrm{it}+1} = V_{i,k}\big|_{\mathrm{it}} + \left.\frac{\mathrm{d}V_{i,k}}{\mathrm{d}t}\right|_{\mathrm{it}} \delta t$$

To avoid numerical difficulties a lower threshold for layer width ($w_{\min}$) of 50 nm was used, below which layers seize to participate as resistance to diffusion, and the outgoing and incoming volume flows are set to zero. To further enhance performance, the time step (δt) was adapted to the cell center-to-center distance (δr), giving stable solutions independent of variation of δt within the permissible range defined by Eq.(2.2).

Eq.(2.16)
$$\frac{D_i^k(T_{\mathrm{b}}) \cdot \delta t}{\min \delta r_k{}^2} < \frac{1}{2}$$

Optimization of Q_{s}, Q_{m}, D_0, and ϕ_0, was carried out using the experimentally obtained values of interface positions r_1 and r_2, measured at 600 and 700 °C. In total 68 average values were weighted with their respective standard deviation (σ_{r_1} and σ_{r_2}), to give a single optimization function (χ^2) according to the maximum likelihood formalism for arbitrary functions.[65]

Systematic parameter variation was carried out for r_0, the median boundary temperature ($\tilde{T}_{\mathrm{b}}$), the charge-discharge cycle frequency (f_{c}), and the cycle half-amplitude (ΔT_{b}) to identify correlated trends in system performance predictors. Temperature dependence of diffusion properties ($\phi_{\mathrm{F},0}^a$, $Q_{\mathrm{F},s}^a$, and $D_{i,0}^k$, Q_{m}, $i = \{\mathrm{A}, \mathrm{F}, \Omega\}, k = \{a, \varphi, \omega\}$) were simultaneously randomized. A standard normal distribution with standard deviation (σ_j) for the j-th parameter (P_j) equal to 0.5, or 1 % of P_j was drawn numerically, $\sim\mathcal{N}(P_j, \sigma_j \cdot P_j)$. 32 parallel simulations were done for each discrete combination of r_0 and T_{b}. Sensitivity of the solution was expressed in terms of average output parameters, corresponding standard deviations, and correlation functions ($\rho_{X,Y}$).

2.2.4. Performance extrapolation

Mixed properties of phase $k = \{a, \varphi\}$, such as the density (ρ^k) and sensible heat capacity (c_p^k) were updated by linear interpolation between the properties of Al-12%Si and 316L (Table 2.1), based on their composition by volume. Eq.(2.17) to (2.20) give the derived system performance parameters. For T_{m} and h_{f}, fitting of DSC results gave first order coefficients for variation of the respective property with ϕ_{F}.

The incubation period after which intermetallic formation set in was defined as the time ($t_{0,\varphi}$) at which w_φ reached the threshold of 3 µm. The latent heat storage density ($\hat{h}_\mathrm{f}$) was defined as quotient of the estimated absolute latent heat ($h_\mathrm{f} \cdot V^a \rho^a$) and the total system mass. An empirical first order mixing coefficient for h_f when Al-12%Si incorporated 316L was defined based on experimental observation. $\partial h_\mathrm{f}/\partial \phi_\mathrm{F} \coloneqq \gamma_\mathrm{f}$ was calculated from DSC results (h_f^*) and Fe concentration in the PCM measured by EDX (ϕ_Fe^*). γ_f was then used in Eq.(3.11) together with ϕ_F calculated numerically.

$$\hat{h}_\mathrm{f} = \gamma_\mathrm{f} \cdot \phi_\mathrm{F} \cdot h_{\mathrm{f},0}^* \qquad \text{Eq.(2.17)}$$

The overall sensible energy density ($\hat{q}_s$) was estimated using the sensible heat capacities of the pure species ($c_{\mathrm{p},i}$) and the partial volume fraction ϕ_i^k.

$$\hat{q}_\mathrm{s} = c_{p,i} \cdot \phi_i^k \qquad \text{Eq.(2.18)}$$

Relative heat transfer limitations were quantified in terms of the Biot number (Bi). Eq.(2.19) compares the surface heat transfer coefficient (u_surf) and the equivalent conductive resistance of *a*, *φ*, and *f*.

$$\mathrm{Bi} = \left(\frac{2r_1}{k_a} + \frac{w_\varphi}{k_\varphi} + \frac{w_f}{k_f}\right) \cdot u_\mathrm{surf} \qquad \text{Eq.(2.19)}$$

The thermal conductivity of a (k^a) was estimated at 70 $\mathrm{WK^{-1}m^{-1}}$, corresponding to what has been reported for molten Al-12%Si.[23] Those of φ and f were [1, 10] $\mathrm{WK^{-1}m^{-1}}$ (k^φ), and 10 $\mathrm{WK^{-1}m^{-1}}$ (k^f). u_surf was varied within the bounds of [10, 100] $\mathrm{WK^{-1}m^{-2}}$, representing passive and active convection. Finally, the latent charging power density ($\hat{p}_\mathrm{f}$), in units of $\mathrm{Wm^{-3}}$, is defined as:

$$\hat{p}_\mathrm{f} = \frac{1}{V^a + V^\varphi + V^f} \cdot \left(\frac{2r_1}{k_a} + \frac{w_\varphi}{k_\varphi} + \frac{w_f}{k_f} + \frac{1}{u_\mathrm{surf}}\right)^{-1} \cdot 2\pi r_2 L_z \cdot (T_\mathrm{b} - T_m) \qquad \text{Eq.(2.20)}$$

2.3. Results

2.3.1. Growth kinetics

The intermetallic layers formed at 700 °C covered the entire interface in all cross-sections, starting with the first observation after one day. Fresh corrosion layers were crack-free and homogeneous in composition. Figure 2.3a) show SEM footage and EDX elemental analysis indicating a largely constant composition over a

layer width of more than 200 µm. A relatively thin transition zone is visible adjacent to the steel. Strong interfaces were formed with both aluminum alloy and steel, which is evidenced by the thermal shrinkage fracture in Figure 2.3b) occurring in the aluminum matrix, in parallel to the 2-day-old intermetallic layer. The bulk of the growing layers was mostly dense with some porosity appearing in proximity of the sharp phase boundaries.

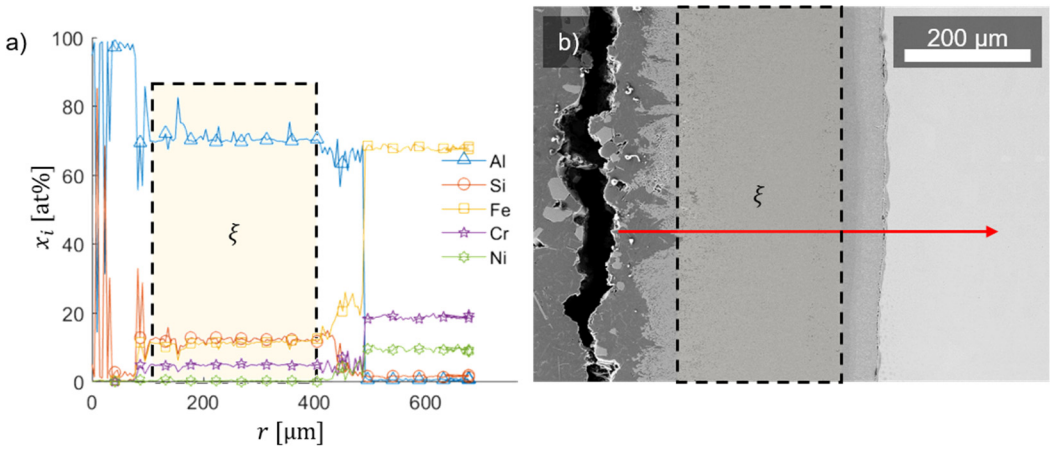

Figure 2.3 **a)** EDX Elemental analysis across the intermetallic layer, formed between molten Al-12%Si and the cylindrical encapsulation from 316L stainless steel after 2 days at 700 °C. The bulk intermetallic composition matches what has been identified as ξ phase.[58] A transition zone with variable composition is found adjacent to the steel. Positions of line scan corresponds to the red arrow in the SE contrast image. **b)** SE contrast image showing from left to right: solidified Al matrix (dark grey), ξ-phase, transition zone, and 316L steel. Brightness increases with Fe content. The layer appears relatively dense and homogeneous, compared to the eutectic microstructure of Al and Si. Cavities and a large tangential fissure on the left indicate thermal shrinkage.

Initial growth was rapid and produced mainly a phase composed of 70 at% Al, 12 at% Si, 12 at% Fe, and 4.5 at% Cr, with trace amounts of Ni, Mn, and Mo in the balance. The measured composition places it in the existence domain reported of the quaternary ξ phase.[58] Layers developing at 600 °C showed similar composition, but relatively higher variability in thickness. The relative standard deviation of the total average width ($\sigma_{w_\varphi}/w_\varphi$), reached 300% during the localized initiation phase and decayed to 20 % after 60 days when the patches were coalesced. In contrast, at 700 °C initiation appeared rather immediate and homogeneous, resulting in a relative variability of $\sigma_{w_\varphi}/w_\varphi$ < 5%, independent of time.

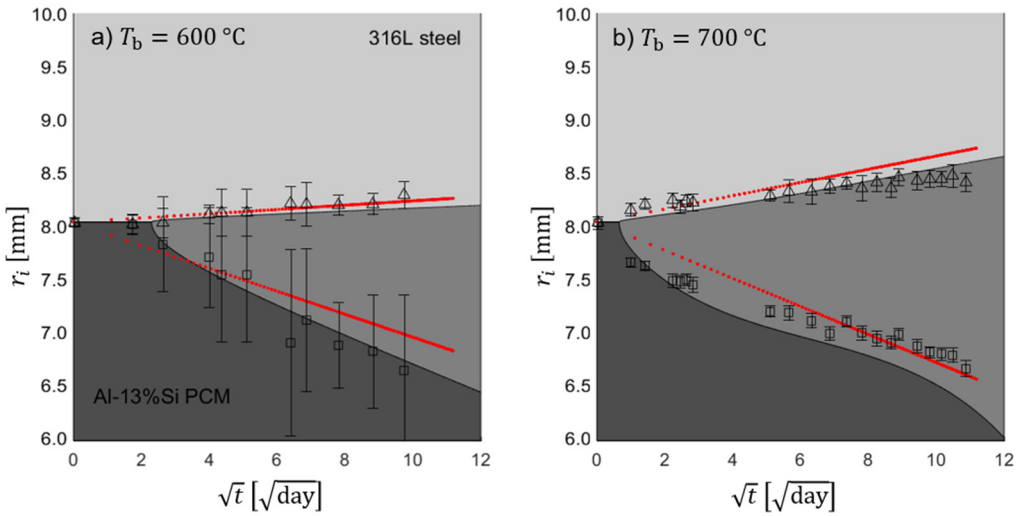

Figure 2.4

Measured and modeled interface location and thickness for the encapsulating steel (light grey), intermetallic (grey), and Al-12%Si PCM alloy (dark grey) for isothermal experiments at **a)** 600°C and **b)** 700°C. The measurements indicate average radial location of the bounding interfaces (square/triangle - markers with error bar) with the PCM and the encapsulating steel. Error bars are derived from the variation of 12 independent distance measurements per point. The computational model (black lines separating the shaded regions) and the standard parabolic growth model (red lines) were fitted to the isothermal experimental. Differences between the two models are associated to the de-passivation (initial delay, pronounced in a) and to dissolution and saturation (changes in slope).

Figure 2.4 shows measured interface migration and compares numerical modelling with analytic fits. The larger standard deviation of the 600 °C samples indicated by the error-bars (Figure 2.4a) is due to localized initiation and resulting island growth. Parameters fitted to the average values were considered to represent volume averaged model coefficients. Table 2.2 summarizes experimental results on layer thickness and sampling conditions. Fitting the overall layer thickness to the parabolic growth model from Eq.(2.3) gave good agreement, when k_p was not constraint by Eq.(2.4). When a temperature-dependent parabolic model, according to Eq.(2.3)-(2.4), was fitted to the position of r_1 from our data set, it gave the best agreement for Q_a equal to 2.3 kJ/mol, similar to what has been reported by Springer et al..[30] We judged the low activation energy to be an artefact related to solubility. Studies that focused on temperature activation in have reported Q_a in the range of 70 to 200 kJmol^{-1}K^{-1}.[62],[63] Our advanced mass transport model predicted optimized activation energies for species mobility of Q_m between 93 kJmol^{-1}K^{-1} for Al and 170 kJmol^{-1}K^{-1} for Fe, and fitted the data on average better than Eq.(2.3). Table 2.3 gives a complete record of the fitted material properties. Temperature dependent solubility of the encapsulating steel is fitted with an activation energy of 114 kJmol^{-1}. A diffusion activation energy of 93 kJmol^{-1} reproduced the experimentally observed temperature dependence of $t_{0,\varphi}$ of 0 to 3 days between 600 °C and 700 °C. Non-monotonic growth rate dw_φ/ dt, ascribed to re-dissolution of φ and varying with the initial PCM volume (compare Figure 2.4b and Figure 2.5a) were accommodated by the set of optimized material property parameters listed in Table 2.3. A maximum likely-hood parameter of χ^2=0.869 was obtained when comparing numerical calculations of interface migration of r_1 and r_2, over a duration of ~120 days. The corresponding experimental data comprised 480 independent measurements with the parameters varied within T=[600…700°C], t=[0…121 days], and r_0=[8…11.5mm].

Summary of sampling conditions, measured average intermetallic layer thickness, and standard parabolic growth coefficient, according to Eq.(2.3), and determination of fit parameter. Standard deviation form 12 circumferential measurements are indicated in parenthesis. *Partial initiation with only few measurements falling on growth islands. Table 2.2

$T_{\mathrm{hold}} = 700°\mathrm{C}, r_2(t_0) = 8\ \mathrm{mm}, k_p = 2.0 \cdot 10^{-12}\ (R^2 = 0.809)$
t_i [day]: 0, 1, 2, 5, 6, 7, 8, 26, 32, 40, 47, 54, 61, 68, 75, 79, 89, 96, 103, 110, 118.
w_φ [µm]: 0(0), 493(42), 577(17), 754(45), 702(26), 737(40), 765(26), 1084(52), 1137(48), 1207(72), 1376(43), 1292(37), 1352(64), 1458(53), 1447(82), 1471(77), 1550(51), 1622(58), 1640(59), 1676(67), 1743(53).
$T_{\mathrm{hold}} = 600°\mathrm{C}, r_2(t_0) = 8\ \mathrm{mm}, k_p = 8.9 \cdot 10^{-14}\ (R^2 = 0.886)$
t_i [day]: 0.001, 3, 7, 16, 19, 26, 41, 47, 61, 78, 95.
w_φ [µm]: 0(0), 2(6), 197(305), 404(384), 581(408), 580(408), 1304(714), 1084(465), 1315(308), 1379(434), 1644(586).
$T_{\mathrm{hold}} = 700°\mathrm{C}, r_2(t_0) = 10.5\ \mathrm{mm}, k_p = 8.3 \cdot 10^{-12}\ (R^2 = 0.893)$
t_i [day]: 0, 3, 7, 16, 25, 58, 113.
w_φ [µm]: 0(0), 755(59), 816(5), 938(148), 825(70), 1297(68), 2110(2.5).

Activation energies and pre-exponential factors obtained by optimizing the temperature-independent coefficients of the numerical model through a maximum likelihood analysis with $\chi^2 = 0.869$. Table 2.3

Diffusivity of in	A a	F a	Ω a	A φ	F φ
Activation Energy, Q_{m} [kJmol^{-1}]	95	135	193	93	170
Pre-exp. Factor, D_0 [m^{2}s$^{-1} \cdot 10^{-6}$]	3.5	0.26	770	0.81	10
Solubility F in a					
Activation Energy, Q_{s} [kJmol^{-1}]	-	114	-	-	-
Pre-exp. Factor, $\phi_{\mathrm{eq.},0}$ [1/1000]	-	97	-	-	-
Rules of Mixing F in a					
$\partial h_{\mathrm{f}}/\partial \phi_{\mathrm{F}}$ [Jg^{-1}/ at%]	-	4.4	-	-	-
$\partial T_{\mathrm{m}}/\partial \phi_{\mathrm{F}}$ [K/at%]	-	23	-	-	-

Consecutive EDX analysis of the Fe content in the PCM showed its rapid incorporation up to around 2.6 at% during the initial 3 days, after which it's it stayed relatively stable (see Figure 2.5a). While Fe levels stagnated, Ni increased continuously at a slow rate up to 2 at% after more than 100 days. Cr remained absent in SEM-EDX analysis of the solidified melt. The corresponding reported saturation concentrations are 3.2 at% for Fe, 9.0 at% for Ni, and 0.7 at% for Cr, in pure Al at 700 °C.[26] Si concentration also seemed to increase continuously to 16 at% after more than 100 days. This may be explained by higher incorporation rate of Al compared to Si into the growing intermetallic layer. However, it is also possible that Si is progressively overestimated in EDX spectroscopy, due to changes chemical interactions and microstructure in the solidified PCM. DSC results showed that h_f decreased from its initial value of 462 J/g (with a standard deviation of 7 J/g) to 398 J/g, when exposed to 700 °C for more than 3 days. For longer exposure times, no significant decrease was noticeable (see Figure 2.5b).

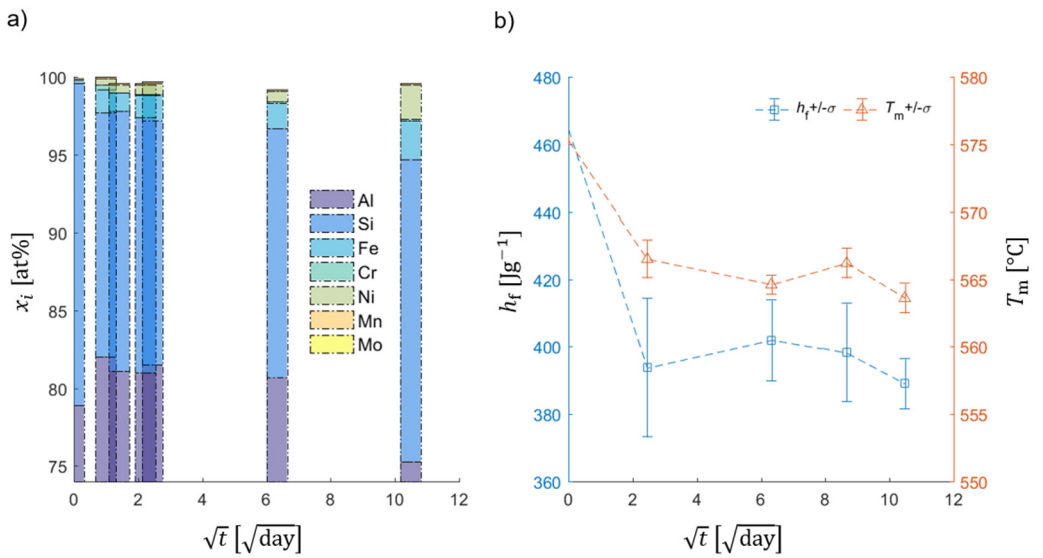

Figure 2.5 **a)** Elemental composition of the PCM alloy during exposure to 700 °C isothermal condition, as determined by energy dispersive x-ray photon spectroscopy. The Fe concentration stagnates at 2.6 % after 3 days and the Si concentration increases as Al incorporates into the melt-adjacent phase. Levels of dissolved Fe and Ni increase over time, while Cr, Mn, and Mo stay below uncertainty of EDX quantification. **b)** Decrease in h_f and T_m (from DSC) correlate with the increase in Fe in the PCM. h_f decreased from 462 J/g to 398 J/g. T_m decreased by 11.6 K.

The same qualitative behavior was observed for T_m, which decreased from 576 °C to 566 °C during the initial period. h_f and T_m changed in correlation with the concentration of Fe, but not with that of Ni. The Cr concentration was too low to give any significant correlation. This permits to address degradation in the design phase by assuming the thermo-physical properties of the ternary alloy resulting from saturation of Al-12%Si with Fe.

2.3.2. Model validation

Experimental validation of our advanced diffusion model was conducted at 700 °C for an initial radius $r_0 = 10.5$ mm (Figure 2.6a), which provided an increase in melt volume of 72 % compared to the original case (Figure 2.1) of $r_0 = 8$ mm. Modelling predicted a depression of growth velocity ($|\mathrm{d}r_{1/2}/\mathrm{d}t|$) with increasing melt volume on the melt exposed side of the intermetallic layer due to increased extent of dissolution. The effect was dampened on the steel exposed side by the thickness and stoichiometry of the layer. The experimental results were in good quantitative agreement regarding the evolution of layer width. However, the model underestimated the effect's intensity, leading to a later arrival of the corresponding inflection points. We hypothesize that the assumed simplified PCM and encapsulation composition used in the model might be causing this. In the real system, the incorporation of Fe and Ni into the melt appeared to happen at distinctly different time scales (section 2.4.1, Figure 2.5a). Dissolution in the model has to occur mono-modal due to the representation of the encapsulation by the single virtual F-particle. Nevertheless, the agreement is satisfactory given the time scale of the experiment. Models which do not consider dissolution will typically overestimate layer growth based on a parabolic fit of experimental data collected during only early growth. However, the parabolic model underestimated the growth when applied to our experimental data for low temperatures (Figure 2.4a), as it is not designed to accommodate delayed reaction onset. At higher temperatures (Figure 2.6a), $t_{0,\varphi}$ is negligible, but for larger radii, prolonged periods of dissolution may lead to an overestimation of interface movement ($\mathrm{d}w_{1/2}/\mathrm{d}t$). This effect is radius dependent as the rate of dissolution is affected by degree of saturation ϕ_F^a. If d_F, r_1 and T_b are assumed constant, the partial change of rate of saturation is proportional to the invers of the volume ($\partial\dot{\phi}_F^a \sim \partial r_0^{-2}$).

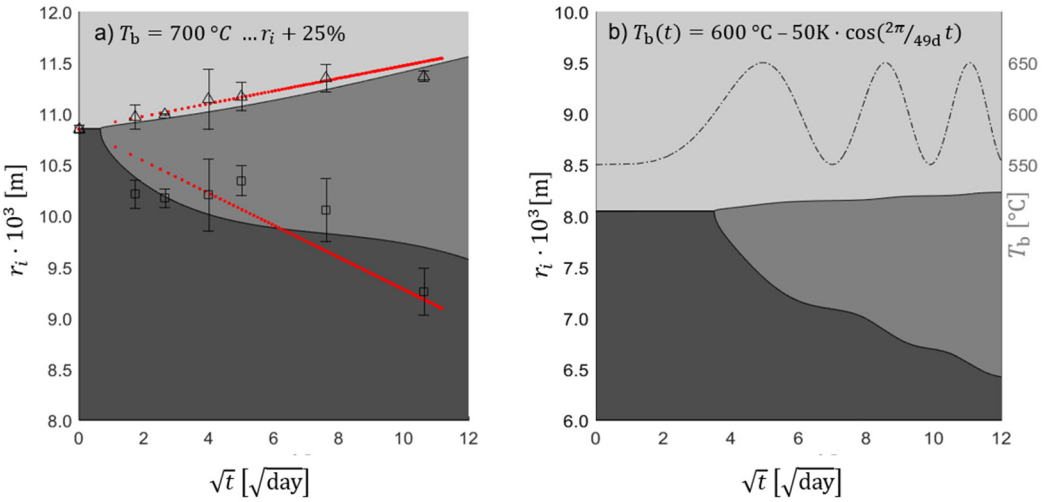

Figure 2.6 **a)** The predicted evolution of r_1 and r_2 (smooth lines, separating shaded areas) with modified initial condition $r_0 = 10.5$ mm compared to the validation experiment (square / triangle with error bars). Agreement in qualitative behavior is notable: The velocity dw_1/dt is positive after $t_{\varphi,0}$. Later its magnitude decreases temporarily before it finally reaccelerates. In the experimental data, dw_1/dt is negative between 5 and 30 days. The parabolic growth model forms a straight line in the same plot (red dots). **b)** Sinusoidal variation of T_b centered at 600°C ± 50 °C (dashed gray line) predicted a prolonged onset period, compared to the 600 °C isothermal data. $dr_{1/2}/dt$ changed in the prediction with an oscillatory contribution from T_b.

The de-passivation period, $t_{\varphi,0}$, was experimentally observed to be longer for 600 °C compared with 700 °C (compare Figure 4a and b). Predicted $t_{\varphi,0}$ increased by a factor of 5 compared to the 600 °C isothermal case when a sinoidal T_b variation with 50 K amplitude was applied. This transient model case had 3 cycles of slow heating and cooling, with a period of 49 days (see Figure 6b). The de-passivation and activation of the intermetallic formation reaction was observed after 16 days only, during the first sinusoidal heat up phase. For the following cycles, the growth of φ slowed down and almost stopped with a notable transition occurring around T_b=575 °C. This modelling result agrees closely with the reported phase transition of Al-12%Si occurring at 576 °C and measured in this work to be 574 °C. Reported experimental observations agree with this result of our model in that intermetallic growth slows in a non-continuous way when the system is brought below the liquidus temperature.[59]

The initial observation of a pronounced effect of the temperature boundary conditions on $t_{0,\varphi}$ motivated further investigations by systematic parameter

variations, which are detailed in Section 4.3. The effect of solubility in the validation case shows that partially reversible and transient scenarios can be modelled with the same set of property parameters obtained for isothermal conditions. A sign change of the second derivative of w ($\mathrm{d}^2w/\mathrm{d}t^2 \sim 0$) or, in other words, slowing and re-accelerating boundary movements have not been addressed by Eq.(2.3)-(2.6). A net shift of r_1 and r_2 towards higher values (towards the outer encapsulation surface) was observed when the solubility increased, and is an intuitive result of the validation case. The parameter variation in the next section aims to present characteristics of the system that cannot be as easily predicted, but which are crucial to the high performance of the Al-12%Si LH-TES PCM.

2.3.3. Parameter variation

The following results of computational parameter variation guide the design of PCM encapsulations, which balance high performance, efficient resource utilization, and longevity. We characterized encapsulation performance in terms of latent heat storage density $\hat{h}_\mathrm{f}$ and latent charging power density $\hat{p}_\mathrm{f}$. PCM degradation is associated with the width w_1, encapsulation corrosion with width w_2. Biot number, sensible storage capacity $\hat{q}_\mathrm{s}$, all as a function of design and operation choices. Figure 2.7 shows $\hat{h}_\mathrm{f}$ at the end of the modelled period (Δt) of 365 days of isothermal operation. T_b was selected from the interval $[575, 735]$ °C and r_0 from $[8, 48]$ mm. $\hat{h}_\mathrm{f}$ was lowest for small radii and high temperatures. This trend was true in absolute quantity and in relative measure with regards to the initial value $\hat{h}_{\mathrm{f},0}$. $\hat{h}_{\mathrm{f},0}$ approaches $h_{\mathrm{f,Al\text{-}12at\%Si}} = 462\ \mathrm{Jg}^{-1}$ when r_0 increases. $\hat{h}_\mathrm{f}$ varied between 325 and 375 J/g when r_0 was 48 mm, while its value reduced to zero under the unfavorable conditions of $T_\mathrm{b} = 735$ °C and $r_0 = 8$ mm. This case was comparable to our laboratory conditions, had the experiment been prolonged by 9 more months. It illustrates that the formation of φ has no intrinsic limitation until conversion of the PCM is complete, or the mechanical stability of the encapsulation is compromised.

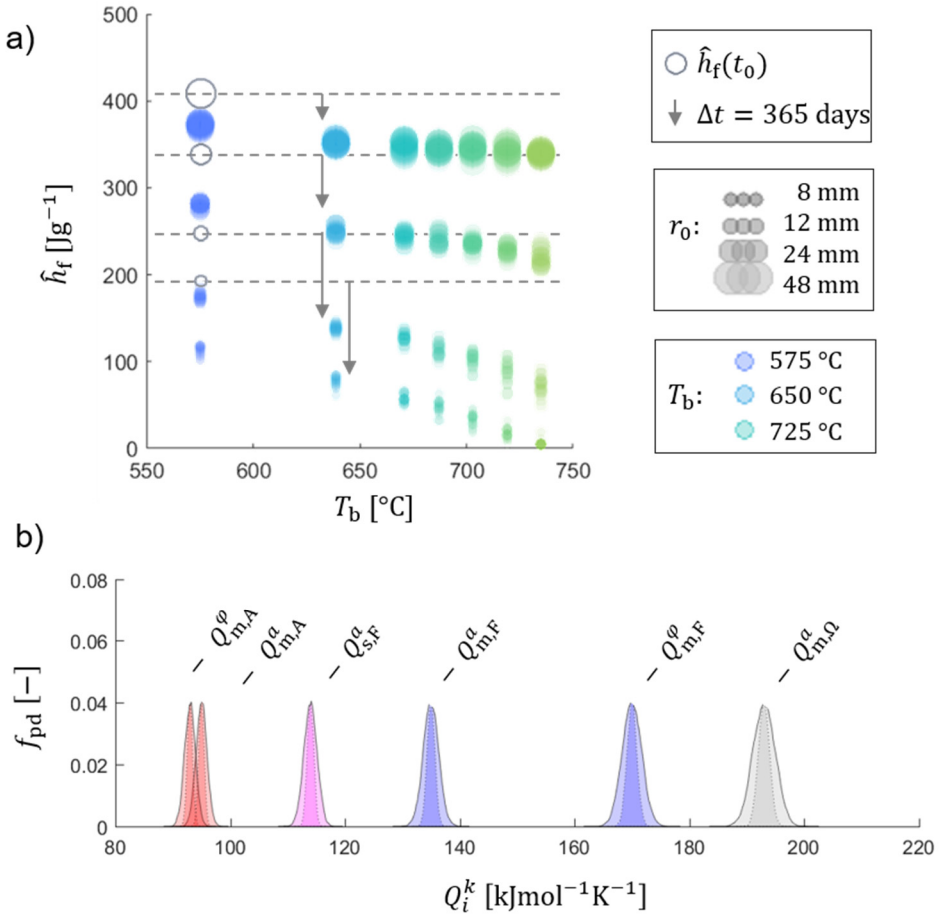

Figure 2.7 **a)** Extrapolation of $\hat{h}_f$ to 365 days of operation for combinations of $8 < r_0 < 48$ mm (marker size), and $575 < T_b =< 735$ °C (marker color and x-axis). $\hat{h}_f$ changes from the initial condition at $(\hat{h}_{f,0}, r_0)$ (open circles), with increasing T_b. Decrease in $\hat{h}_f$ was more pronounced for small r_0, and large T_b. Each discrete variation (r_0, T_b) is composed of 32 points representing independent numerical simulations with simultaneously randomized material parameters Q_s, Q_m, D_0, and ϕ_0. **b)** Probability distribution of the mobility and solubility activation energies used for the numerical extrapolations. Mean μ_X are fitted to experimental data, while $f_{pd} \sim \mathcal{N}(\mu_X, \sigma_X)$ assumes $\sigma_X \sim 1\%$ or 0.5% (respective shaded areas).

For larger values of r_0, we found an important kinetic stabilization of $\hat{h}_f$, when T_b was larger than 650 °C. This behavior is related to prolonged periods of dissolution, kinetically depressing layer thickness and stabilizing melt volume (see Figure 2.8 and 2.9). This permits operation in a quasi-stable regime where the combination of melt volume and $\phi_F^a(T_b)$ gives extended periods of low effective degradation ($dw_\omega/dt \approx 0$) by negative partial layer growth ($dw_1/dt\,, dw_2/dt < 0$), and constant dissolution rate ($J_F^d \approx$ constant), as long as the chosen encapsulation thickness is large enough (see Figure 2.8a).

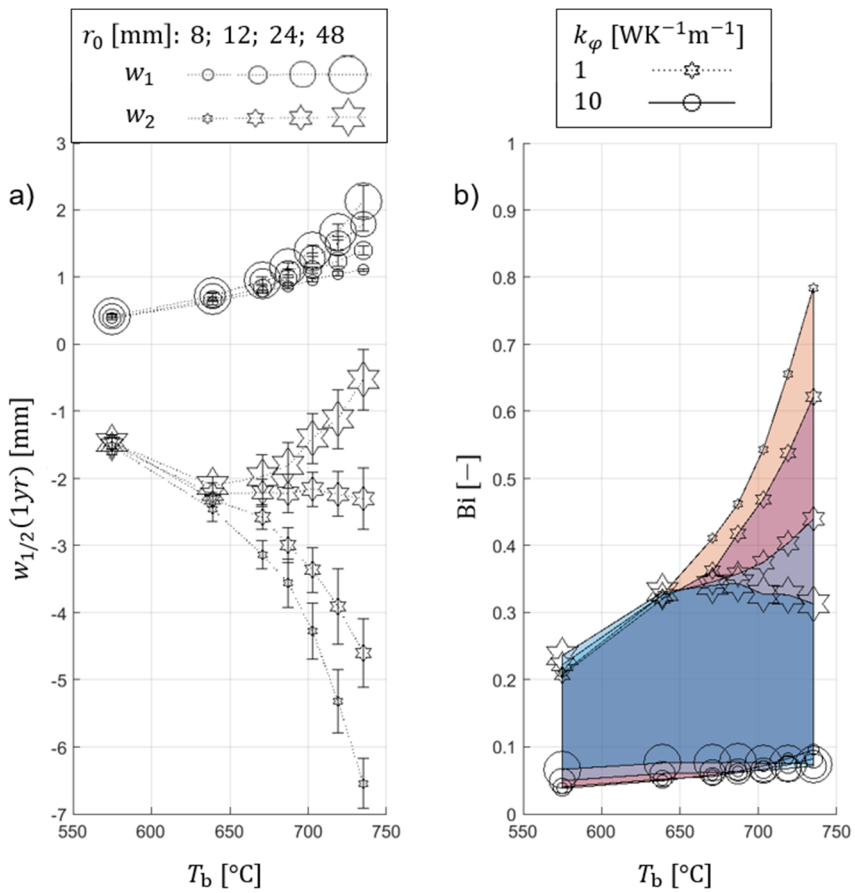

a) w_1 and w_2 represent corrosion of the encapsulation (positive values) and conversion of the storage medium (negative values), as a function of r_0 and T_b. w_1 increases with r_0 and T_b, while w_2 increases with T_b for small r_0 but has a maximum close to 650 °C for $r_0 = 48$ mm. **b)** Biot number as a function of temperature and initial radius for u_b=100 WK^{-1}m^{-2} and varying intermetallic layer conductivity k_φ. Surface heat transfer is limiting in all cases. The maximum value of Bi=0.8 is reached for $k_\varphi = 1$ WK^{-1}m^{-1} at the minimal radius and maximal temperature, where w_ω was also largest.

Figure 2.8

In many TES technologies with low conducting PCM, conduction in the bulk is limiting for heat storage and release rates. In contrast, we find a maximum for the Bi ~ 0.35 at $T_b \sim 650$ °C and r_0=48 mm (see Figure 2.8b) for k_φ=1 $WK^{-1}m^{-2}$ and u_b=100 $WK^{-1}m^{-2}$, owing to the high intrinsic conductivity of Al-12%Si. Reported values for bulk conductivity of FeAl vary from 10 $WK^{-1}m^{-1}$ at ambient temperature, to 18 $WK^{-1}m^{-1}$ at 1000 °C.[69] The assumptions of k_φ=1 $WK^{-1}m^{-2}$ represents a case where the effective conductivity of φ is reduced by an order of magnitude or more, for example mimicking layer porosity that is significantly larger than 50 %.[70] u_{surf} is on the typical scale of forced gas convection. We find Bi<0.4 for all values of r_0, if T_b is below 650 °C. Above this temperature, Bi reaches a value of 0.8 for r_0=8 mm. Intrinsic access to low Biot numbers alleviates the need for internal fins or secondary high conductivity phases, as are often discussed for salt based PCM encapsulations.[71]

We resolved the corrosion layer width in terms of w_1 and w_2, which facilitates dimensioning of the encapsulation with regard to storage capacity and encapsulation integrity (see Figure 2.8a). The magnitude of w_1 strictly increased with T_b for $r_0 \leq$ 12 mm. Larger radii amplified the effect of temperature-dependent solubility, as is seen by the decrease of w_1 for r_0=48 mm as T_b increases beyond 650 °C. We found that the investigated system was highly tunable with respect to $\hat{p}_f$, i.e. at 48 mm and 639 °C a value of $\hat{p}_f$=190 kWm^{-3} was reached. Reducing r_0 by a factor of 2, we found $\hat{p}_f$= 365 kWm^{-3} while reducing $\hat{h}_f$ to 70 %. Further reducing r_0 to 12 mm gave $\hat{p}_f$= 666 kWm^{-3}, with 37 % of $\hat{h}_f$. We gained a similar boost when increasing T_b to 671 °C (738 kWm^{-3} while conserving 64 % of $\hat{h}_f$ compared to the reference case). In general, small radii favored power and large radii favored energy density. Both $\hat{h}_f$ and $\hat{q}_s$ decreased with increasing T_b (Figure 2.9a), however the ratio of changes $\partial\hat{h}_f/\partial\hat{q}_s|_{r_0}$ shifted in favor of $\hat{h}_f$ for larger r_0. The shift towards lower sensible energy density with decreasing r_0 resulted from the low specific heat capacity of the steel encapsulation compared to that of the PCM. In this case, maintaining the mechanical integrity of the encapsulation required adding more steel to the system.

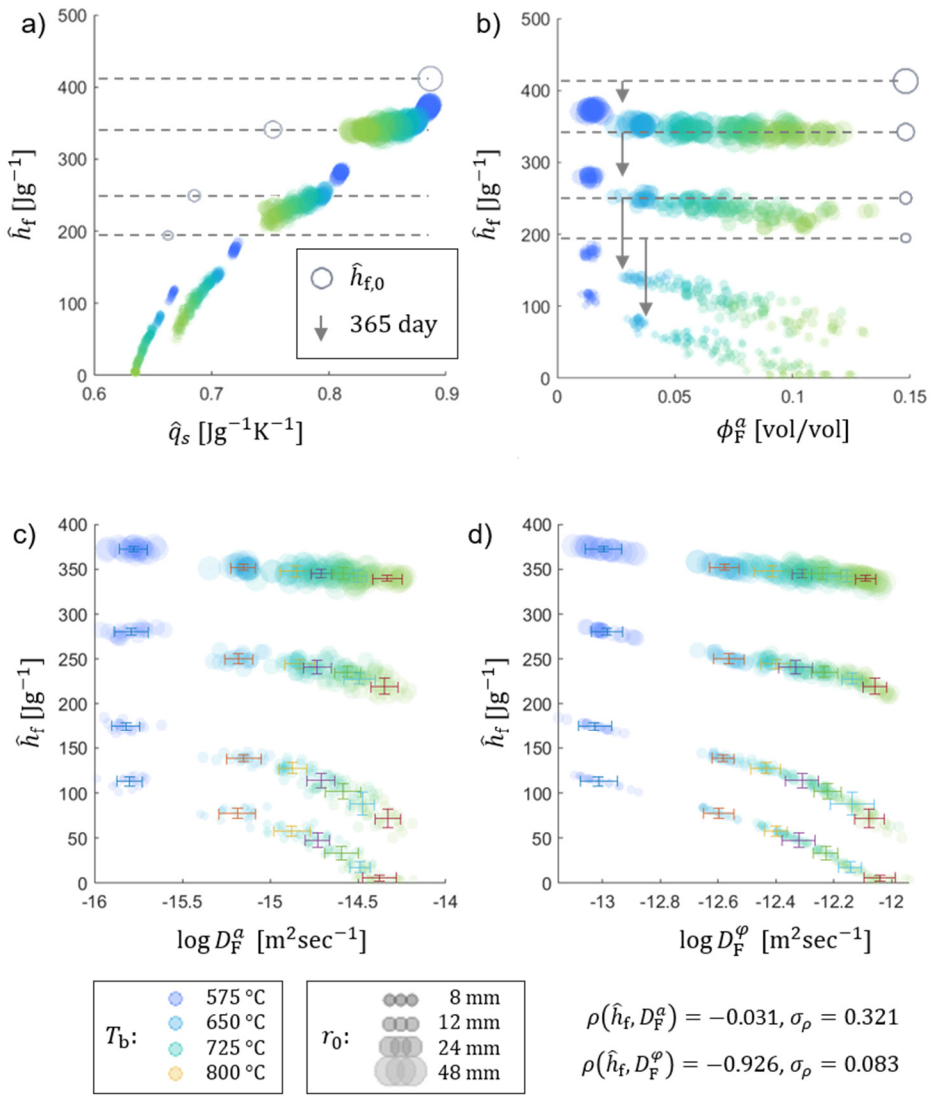

a) $\hat{h}_f$ as a function of vs $\hat{q}_s$, after 365 days of simulated operation for combinations of r_0 and T_b. Large r_0 and low T_b lead to high $\hat{h}_{f,0}$ (open circles) and conserve storage density per overall system-mass. **b)** $\hat{h}_{f,0}$ as a function of ϕ_F^a. $\hat{h}_f$ decreases with increasing ϕ_F^a and T_b. The trend is more pronounced for small r_0. **c)** $\hat{h}_f$ as a function of D_F^a. $\hat{h}_f$ decreases with increasing D_F^a. **d)** $\hat{h}_f$ as a function of D_F^φ. $\hat{h}_f$ decreases with increasing D_F^φ. Error bars in c) and d) indicate σ_X from probabilistic modelling (X=$\hat{h}_f \vee D_F^a \vee D_F^\varphi$, respectively).

Figure 2.9

Figure 2.9b shows a continued decrease of $\hat{h}_{\mathrm{f}}$ with ϕ_{F}^{a} and T_{b} for small radii, which was largely suppressed for r_0=48 mm. It is further apparent that similar degrees of saturation were reached for a given T_{b}, independent of r_0. This is understood in terms of absolute dissolution ($\sim T_{\mathrm{b}} \cdot r_0^2$) of otherwise converted material. A significant correlation between $\hat{h}_{\mathrm{f}}$ and diffusivity is uniquely observed with D_{F}^{φ}, giving a correlation factor ($\rho(\hat{h}_{\mathrm{f}}, D_{\mathrm{F}}^{\varphi})$) of -0.926 (Figure 2.9d). The covariation of $\hat{h}_{\mathrm{f}}$ and D_{F}^{a} ($\rho_{\sigma}(\hat{h}_{\mathrm{f}}, D_{\mathrm{F}}^{a})$=-0.031, Figure 2.9) was not pronounced. The transport of encapsulation elements to the reaction site at the liquid interface limited the conversion of phase change medium. Mitigation strategies for corrosion of this and similar PCM systems may thus focus on limiting diffusion from the encapsulation through the interface layer into the PCM domain.

Figure 2.10 shows the influence of cycling conditions on the passivation lifetime. Cycling may half the onset time when transitioning from large to small frequencies, in the case of hot start. Cycling may increase the onset time by an order of magnitude depending on the cycles phase shift with regard to the high and low temperature semi-period. From the model definition, it is expected that dissolution time will increase over-proportionally ($t_{0,\varphi}$ increases considerably) when the temperature is further decreased, i.e. when T_{b} is very close to T_{m}. At high frequency, $t_{0,\varphi}$ asymptotically approaches a value close to 1 day for the high amplitude case (600$\pm$75 °C), independent of the phase shift. The traces bifurcate in function of the phase shift near $f_{\mathrm{c}}\sim$1 day. Variability introduced by property randomization is exaggerated near the critical phase shift bifurcation frequency (further called passivation half-life frequency, f_{pass}), hinting at a discrete nature of the underlying mechanism. The favorably shifted cycles (i.e. the cycles starting with the cold period) then ascend parabolically with lower frequencies, while hot initiated cycles experience a depression of their passivation lifespan by half. The suggested mechanism entails that exploiting passivation prolongation excludes the desired high-energy storage turnover, however, we find that the scenarios present in Figure 2.10 are in fact relevant to applications which demand characteristic capacity to power ratios on the order of 6-12 h, such as for CSP applications. Al-12%Si has a suitable melting temperature for certain novel CSP varieties[8], and plant optimization scheduling is at the foundation of the technology. Figure 10b shows the passivation lifetime in dependence of cycle shape, over a range of amplitudes. The phase shift of the three compared waveform cycles in Figure 2.10b) is identical and the same is true

for the average cycle temperatures. De-passivation by dissolution does not scale linearly with temperature, which explains the impact of cycle shape. But the same seems to be true for re-passivation.

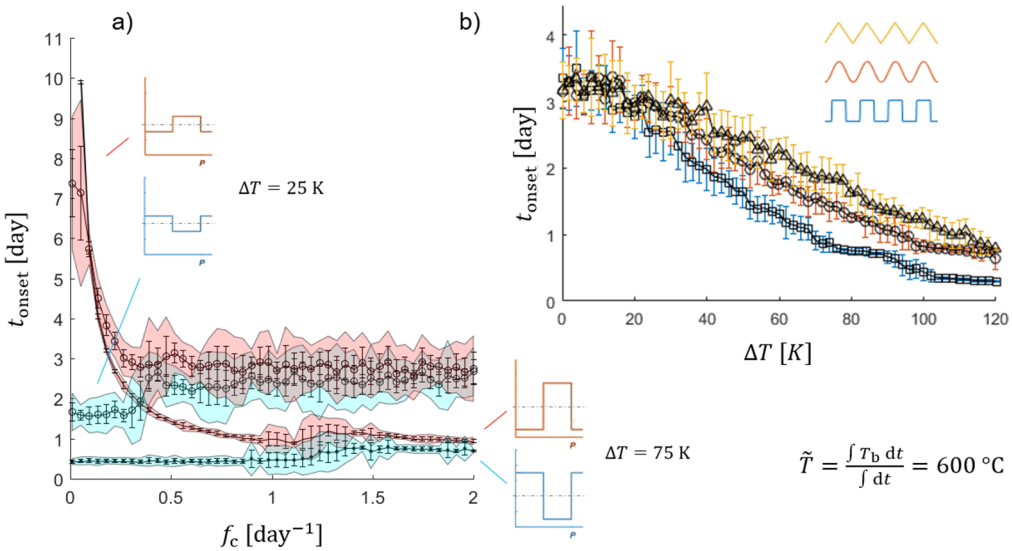

a) The modelled effect of load cycle frequency on degradation onset for a square wave profile of high ($\tilde{T}$ ± 75 K) and low ($\tilde{T}$ ± 25 K) cycle amplitudes. The delay is affected by the phase shift of the cycle (red and blue colored results), leading to a bifurcation of the observed $t_{0.\omega}$ by a factor of >20 in the high amplitude case. For high frequencies $t_{0.\omega}$ approaches 3 days and 1 day, respectively, for low and high amplitudes. **b)** Load cycle shape and amplitude influence the lifetime of the passivation layer as shown for f_c=2 (where the effect of the cycle phase shift is weak).

Figure 2.10

Decisive for the exploitation of the discrete nature of the mechanism as a tool to achieve permanent PCM passivation is the regenerative power of the encapsulation. Dissolution of oxide in our model is not irreversible by nature, but the dimensions of it make replenishing passivation constituent from the bulk PCM extremely unlikely. Oxide layer formation on steel has been characterized to approach steady state or react to chemical changes in the environment on the time scale of seconds,[72] to hours[62],[73]. Crucial to the stability of this encapsulated PCM system may be to let it breath, i.e. by utilizing differential thermal expansion to transport oxygen to the interface, instead of using a hermetically sealed container design. But before these questions may be answered, it is necessary to validate these predictions in transient cycling experiments and foster and refine an in-depth understanding of the mechanisms at the latent-encapsulation interface. It seems likely that the relation of

high frequency passivation lifetime ($t_{0,\varphi}(f_c > f_{\text{pass}}) \coloneqq t_{0,\varphi,\infty}$) and half-life frequency follows the general idea of Eq.(2.21) at least below f_{pass}.

Eq.(2.21)
$$t_{\text{on.},\infty} \sim \frac{1}{f_{\text{pass}}}$$

Given the magnitude of the effect spanning from approximately 12 h to 20 days of degradation free operation, this perspective obtained through numerical extrapolation of experimental data motivates to peruse transient cycling experiments with carefully selected cycle definitions.

2.3.4. Microstructure

The intermetallic layer microstructure (Figure 2.11) in an SEM cross-section study is substantially richer in features than our model assumes. Nevertheless, beside the application relevant insights into interaction of heat transfer performance and passivation with the solubility of the generic *a* and *ω* phases, the optimized predictors for species mobility point to Fe mobility in the layer as determining factor as the most mobile species. Figure 2.11b-d show close ups of a long growing isothermal layer, notably exhibiting staggered porosity gradients within each consecutive layer of a distinct phase. Similar porosity gradients have been associated with diffusion couples when atomic mobility is unequal.[74] In our case, optimized values for D_{F}^{k} were 4 orders of magnitude lower than for D_{A}^{k}. We did not observe spalling of the intermetallic layers, despite the presence of fissures in all layers, after quenching and cross-sectioning. Tangential orientation of these fissures resulted in cylindrical shells, with various degree of segmentation. Their shape and mechanical connectivity fixed them to the interface. In the center of the PCM, the τ phase appeared in the form of 10-20 µm wide particles (see Figure 2.10c). τ was observed having compositions in the range of 65.0-66.0 at% Al; 13.1-14.4 at% Si; 16.1-17.3 at% Fe, with Cr, Ni, Mn, and Mo giving the trace balance <5 at%. Initially rapid formation of ξ-phase was partly replaced by the formation of an η layer on the Fe-rich side of the interface. It increased to one third of the layer phase composition after 110 days at 700 °C. η composition varied within 68.1-69.4 at% for Al, and 27.0-28.1 at% for Fe. The trace balance comprised Cr, Ni, Mn, Mo, and Si and was smaller than 4%. This fraction is likely overestimated given the abundant presence of sub-micron particles (see Figure 2.11d). In the volumetric frame of reference, these particles are expected to

drift towards the center of the cylinder, if the η matrix treats them as inert markers and J_A is locally larger than J_F. The optimized value of ϕ_F^{φ} was 0.22. ϕ_{Cr}^{316L} measured by SEM-EDX was 0.196. The product $\phi_F^{\varphi} \cdot \phi_{Cr}^{316L}$ lied in the observed range of ϕ_{Cr}^{ξ} (4.3-4.9 at%), which suggests that the Cr supply may determine the ξ formation. The absence of Cr in the melt (see Figure 2.5a) supports this hypothesis. This result agrees with the correlation for D_F^{φ} found through fitting interface migration kinetics and implies that encapsulation elements are limiting for φ formation. These findings are consistent with the picture of low mobility of F compared to A (Table 2.3), and further suggest that at least initially Cr is limiting for layer growth.

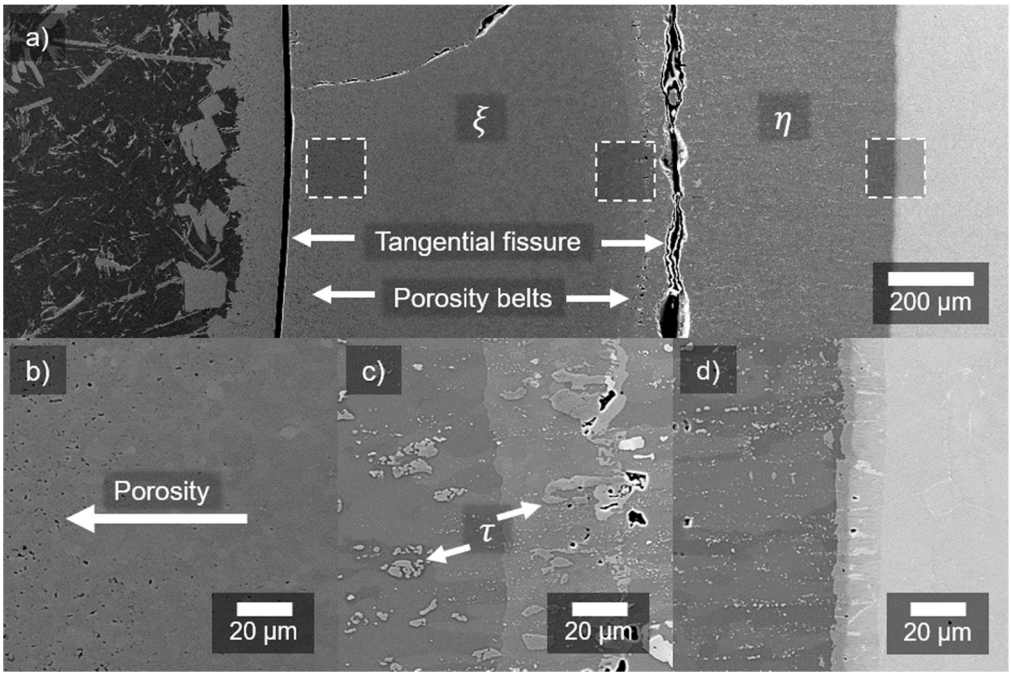

a) Electron microscopic investigation of the intermetallic layer developed after 110 days at 700°C, exhibiting an oriented microstructure between 316L (left) and Al-12%Si (right). η and ξ domains are separated by a sharp phase boundary (center). Tangential cracks appear close to belts of porosity, on the Al-rich side of both large domains. Precipitates in the Al matrix (right) contain Fe, Si, and Ni (SEM-EDX). The total thickness of the intermetallic layer is 1520 µm. **b)** A 10-15 µm thick transformation zone is visible between steel and η, with a third porosity belt on the Al-rich side. **c)** Additional porosity is concentrated in a narrow region in the η phase, close to the boundary to ξ, τ precipitates are present on either side η-ξ boundary. **d)** Porosity within ξ increases gradually towards the interface with Al-12%Si.

Figure 2.11

2.4. Conclusions

We experimentally and numerically investigated the interface of molten Al-12%Si encapsulated in a 316L, and found important implications in terms of performance preservation and degradation, adding to the attractiveness of the system in latent heat thermal energy storage applications. Degradation in the form of molten metal corrosion and intermetallic layer growth has, until now, caused the entire class of Al alloy PCMs to be regarded as unpractical. We find after experimental and numerical investigation that reactive dissolution by the PCM provides a mechanism that, given a consistent set of design and operation decisions, can counteract intermetallic layer growth and simultaneously stabilize capacity and power density. For cylindrical encapsulations of a radius larger than 4-5 cm, solubility prevents thermal resistance built up from intermetallic deposits, at the expense of approximately 1 mm of sacrificial encapsulation thickness per year. The synergetic effects of this strategy results in high heat transfer rates trough high operation temperatures and Bi numbers staying below 0.5. Bi are further predicted to decrease as the result of aging. The excellent properties of the PCM and the reducing interface resistance (thanks to strong chemical interaction with the encapsulation) produce a high-density thermal energy storage system that outperforms high surface area geometries in terms of heat storage capacity, power density and material utilization. Our modelling results reveal that the envisioned scenario requires the heat source to supply heat in excess of 650 °C to the storage to prevent buildup of heat transfer resistances. Transient load-cycle experiments are required to validate these modeling predictions.

The advanced diffusion model was developed to incorporate de-passivation and re-dissolution phenomena. The model was fitted to multiple months of experiments in order to find diffusion coefficients of Fe and Al in the intermetallic layer, and allow for accurate predictions up to 1 year at isothermal conditions. Optimized diffusion coefficients agreed with literature and reproduced experimental observations over a range of parameters, for which typically used models resort to domain splitting or the use of unphysical parameters. Additional experiments validated our advanced model, which was then used to extrapolate performance indicators up to a period of one year of full-load-charging, i.e. at a temperature higher than T_{m} of Al-12%Si.

The experimental characterization of the metal-metal interface showed in all cases the formation of a dense intermetallic layer, covering the entire internal surface and permitting precise and efficient numerical modelling. Phase identification by comparing SEM-EDX found that first the ξ phase, and subsequently τ and η contributed to the width of the intermetallic layers. Thermo-physical showed that h_f and T_m were primarily affected by the incorporation of Fe into the PCM. Ni seemed to incorporate to a lesser extent, whereas Cr was absent in the spectral analysis of the solidified melt. Fe concentration stabilized close to reported saturation concentration of Fe in pure Al, as early as one week into experiments. Probabilistic modelling yielded a unique correlation of storage density with D_F^{φ}, indicating that mobility of encapsulation species inside the corrosion product may be a critical factor. Microstructural investigation by SEM-EDX confirmed assumptions of the zero-dimensional diffusion model. We found a radially oriented grain structure, which agreed with the symmetry prerequisites exploited by the model. Multiple layers were distinguishable at the metal-metal interface, and within any given layer porosity was observed on the Al-rich side only. Porosity anisotropy has been linked to greater atomic mobility of the diffusion partner on the porous side, in marker-drift experiments.[74]

Upscaling of encapsulation radii to r_0= 12 mm, 24 mm, and 48 mm was calculated to result in initial latent heat storage densities of 53 %, 72 %, and 89 % compared to h_f of the PCM alloy ($h_{\mathrm{f,Al\text{-}12\%Si}}$=462 $\mathrm{Jg^{-1}}$). Results from numerical modelling of 8760 h (one year) of full-load-charging predicted a drop in the energy density to 15-38 %, 49-60 %, or 72-80 %, for the three respective radii. For any given radius r_0 degradation increased with charging temperature. However, the relative change in degradation of $\hat{h}_\mathrm{f}$, of 15-38 %, 12-23 %, and 9-17 %, decreased with increasing r_0, for any given temperature. These predictions over a year of full load charging assume constant operation at the maximum charging temperature. Operational lifetime, however, can be expected to increase to several years before reaching the calculated full-load-charging degradation, which is evident considering that in any utilization schedule the PCM must reside below T_m for a reasonable fraction of the time.

We find an important synergy between the high thermal conductivity of Al-12%Si and the solubility effect on intermetallic layer growth. Inherently good heat transfer allows for more compact encapsulations than with other PCM alloys. Compact

encapsulation, i.e. such with low aspect ratio, facilitate dissolution of internal intermetallic layers. This reduces the main source of heat transfer impediment, which in turn extends the lifetime of compact encapsulation geometries, while at the same time conserving energy density. This mechanism is evidenced by our finding of a maximum Biot number for the largest encapsulation equal to 0.4, with a decreasing trend for larger T_b. For the smallest radii, Bi was increasing from 0.4 to 0.8 over the same temperature range.

We conclude from the combined experimental and numerical investigations that encapsulation of Al-12%Si in 316L cylinders is a viable approach for high thermal conductivity and high heat of fusion PCM-thermal energy storage applications. The optimized and validated model relies on entirely physical parameters and made quantitative predictions of the reaction between PCM and encapsulation. The model was used to guide the design of encapsulated PCM storage units outside of the experimentally investigated operational and design conditions. We calculated noticeable stabilization when increasing r_0 to 12 mm.

Trends indicated significant performance advantages and degradation suppression when further increasing the radii to 24 mm and 48 mm. Combined encapsulated PCM Latent heat storage densities of over 300 kJ/kg and charging power density over 360 kW/m^3, not accounting for the heat transfer fluid, were on competitive levels after 8760 h full-load-charging in the aggressive scenario of constant operation at equal to $T_m + 120$ K. Further investigations should focus on refined modelling and validation when transient, or non-isotropic temperature boundary conditions are applied.

Appendix A contains additional data not originally used in the journal publication. We consider them now important for the field of iron aluminide intermetallic phases, i.e. with regard to nucleation and crystallographic orientation of grains initiated an the solid-liquid interface.[75]

A2

Appendix to Chapter 2: Crystallographic structure investigation

A2.1. Diffraction-nanostructure relations

Characterization of the atomic coordination of materials by analyzing patterns produced in Neutron Scatter Experiments (n-scattering) has been demonstrated to have superior resolution on the atomic scale compared to other diffraction techniques.[76],[77] Penetration into dense samples beyond the capability of other techniques such as X-Ray Diffraction (XRD) and Electron Backwards Scattering Diffraction (EBSD) is related to the scattering cross-section of the probing particle.[78] Elastic scattering of particle waves on crystal lattice planes has been described in terms of Bragg's law, Eq.(A2.1).[79]–[82] The angle of diffraction θ and the lattice plane spacing d is related to the wavelength λ of the incident particle, where n=1,2,3,... is the scattering order.

$$2d = \frac{n\lambda}{\sin\theta} \qquad \text{Eq.(A2.1)}$$

In contrast to x-ray scattering that most often uses monochromatic photons from the Cu K_α transition, n-scatter facilities may use monochromators or beam chopping and time-of-flight (TOF) registered detection of polychromatic pulsed neutron sources.[78] A number of beam filters with low-/high-pass characteristics and various resulting optimized geometries exist, but TOF detectors generally have the advantage in terms of neutron collection yield without the need for large single crystal Bragg-prisms. As

a result, findings from energy disperse neutron spectroscopy have been reported in terms of *d*-spacing, rather than Bragg angle.[83],[84] Diffraction patterns obtained from monochromatic x-ray experiments are converted into d-space using Eq.(A2.1) and the characteristic wavelength of the source, i.e. in most cases this is $\lambda(\mathrm{K}_{\alpha,\mathrm{Cu}})$=1.5406 Å.[81],[82],[84],[85] The wavelength corresponding to the particles kinetic energy (E_ν) is described by the Planck equation (A2.2).[86]

Eq.(A2.2)
$$E_\nu = h_\mathrm{P}\nu_\mathrm{n}$$

Broadening of peaks in diffraction patterns has been used to estimate degree of atomic long-range order in x-ray diffraction experiments.[87] Eq.(A2.3), known as the Scherrer equation, relates the mean size of ordered domains contributing to diffraction (τ_S) to the De Broglie wavelength (λ_B) and the peak broadening (β_br) estimated as the full-width at half-height of a given Bragg-reflex.

Eq.(A2.3)
$$\tau_\mathrm{S} = \frac{K\lambda_\mathrm{B}}{\beta_\mathrm{br}\cos\theta}$$

K is the unit-less instrument factor, with value below and close to 1. $K \sim 0.9$ has been used in the absence of a determined value.[87] τ_S is dominated by the lower size crystalline domains. Eq.(A2.3) has been applied for quantification of randomly oriented sub-micron crystallites of low aspect ratio. Precision can be improved by adjusting *K* to the second decimal, but this has been suggested to be material dependent.[87] Besides uncertainties about the materials formed and the appropriate calibration factors, the disperse nature of the source decouples λ_B and θ by adding the time of flight degree of freedom. Independent variation of neutron energy and collection angle has been pursued as an important field of n-scattering research.[78],[88] From the (at the time of measurements) 6 available detector banks we will focus on bank 3, 4, and 5, and on the *d*-space vicinity corresponding to diffraction angles where $\cos\theta$ in Eq.(A2.3) amplifies the effect of peak broadening from crystallinity (Figure A2.1 and Table A2.1).

We will not attempt to achieve accurate quantification of grain size distribution in the freshly formed aluminide phases. Rather, new signals are attributed to the corresponding intermetallic phases and preliminary implications will be compared to the ongoing discussion about the nature of the elongated crystallites in the early growth phase of iron-aluminides at the solid-liquid interphase for Fe and Al, respectively.[38],[40],[75]

The detector bank parameters of the GEM n-diffraction facility, Harwell campus, UK. Table A2.1

Detector Bank	Scattering angle, 2θ [deg]	Azimuthal angle, ϕ [deg]	Secondary flight path L_2 (m)	Solid angle, Ω $[sr]$	Resolution $\frac{\Delta Q}{Q}$ [%]	Minimum accessible momentum Transfer, $Q_{\min}$, [Å^{-1}]
Bank0	1.21–3.18	$\pm$ 90.0	2.757–2.767	0.008	5–10	0.04
Bank1	5.32–12.67	$\pm$45.0	2.365–2.376	0.056	4.7	0.17
Bank2	13.44–21.59	$\pm$43.4	1.477–2.100	0.093	2.4	0.43
Bank3	24.67–45.61	$\pm$42.5	1.077–1.893	0.478	1.7	0.79
Bank4	50.07–74.71	$\pm$44.4	1.028–1.436	0.988	0.79	1.56
Bank5	79.07–106.60	$\pm$44.5	1.376–1.383	1.135	0.51	2.35
Bank5X	106.02–114.19	$\pm$42.7	1.377–1.387	0.378	0.5	2.95
Bank6	142.50–149.72	$\pm$69.3	1.544–1.738	0.280	0.34	3.50
Bank7	149.98–171.40	$\pm$66.6	1.035–1.389	0.443	0.35	3.57

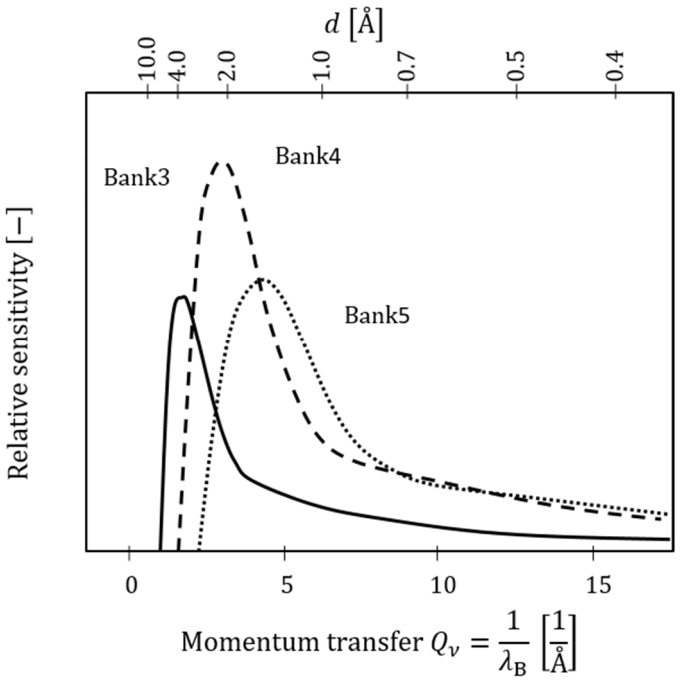

Figure A2.1 Relative sensitivity of selected detector banks at GEM-ISIS, Harwell UK.

While time resolved studies of nucleation and growth have been carried out in the past,[38] our experimental setup has the potential to simultaneously scan a relatively large volume, unambiguously confirm phase identities, while also giving inside about crystallographic anisotropy, thus making use of the unique possibilities of the n-scattering technique and contributing to ongoing scientific interest.

A2.2. Time resolved n-scattering

Neutron diffraction patterns were obtained at the General Materials Diffractometer (GEM), at the ISIS pulsed neutron source, at Harwell campus, UK. Neuron bursts were ejected from a tantalum spallation target when it was impacted with high-energy protons from the ISIS' Penning H^- ion source, operating at 665 keV. Electrons were stripped when the beam was passed through a 0.3 μm thin Al_2O_3 foil before entering the synchrotron for homogenization and acceleration to 800 MeV. High-energy neutron pluses from bombardment of the tantalum target at 50 impacts per second were passed to the GEM detector array after collimation and moderation. A beam current of 178 μA worth of protons was directed at a 6 mm wide Al cylinder

(99.99%) contained in a solid iron cylindrical shell (99.9%) of 9 mm outside diameter. The 35 mm long Al core was machined to fit into the Fe shell with 0.1 mm clearance. The geometry exposed 660 mm^2. Al-Fe interface area to the beam (Figure A2.2).

The tantalum holder with sample at the center of the diffractometer was evacuated to minimize oxidation during the subsequent melting of the Al core. Integration during 24 sec typically gave 1.024 μAs of collective scattered neutron yield on 7270 detectors for scattering angles of 2θ between 1.1° and 169.3° (Figure A2.3). Figure A2.4 shows the applied temperature sequence and the neutron collection current. It can be seen from the figure, that the neutron current was interrupted, notably at the beginning of the experiment, when T_m(Al) was reached briefly. The temperature was lowered in response to mitigate dataloss, and heating was resumed when the neutron beam was back online. Data treatment and analysis was done after the experiment was recorded in MATLAB 9.1 (R2016b). Spectra were averaged over windows of constant neutron counts and smoothed with sliding average algorithm to facilitate automated peak detection and peak width calculation using built in MATLAB functions.

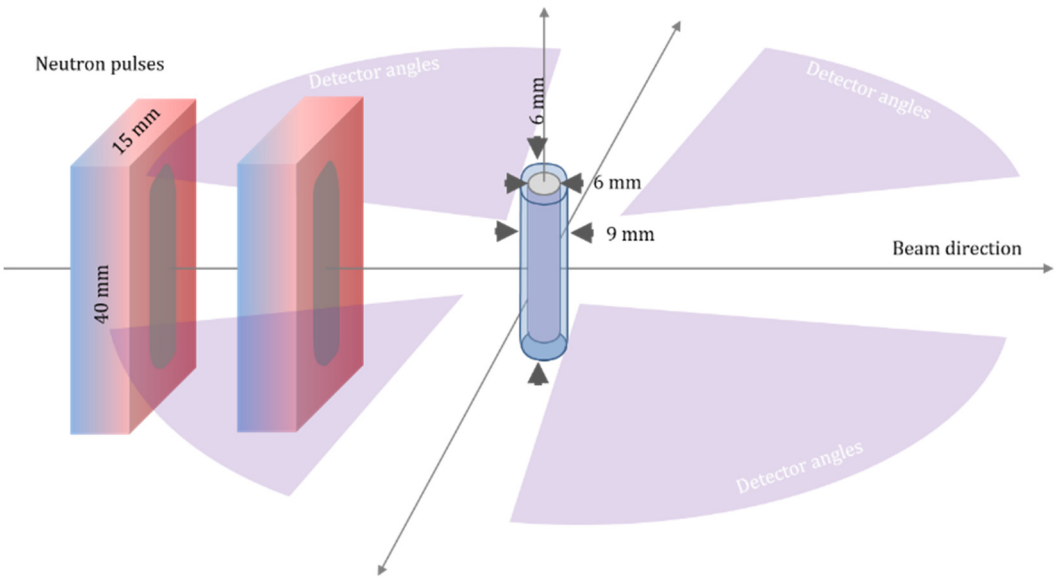

Figure A2.2 Sample geometry and orientation relative to energy disperse, incident neutron pules, and time-of-flight spectroscopic detection regions.

A2

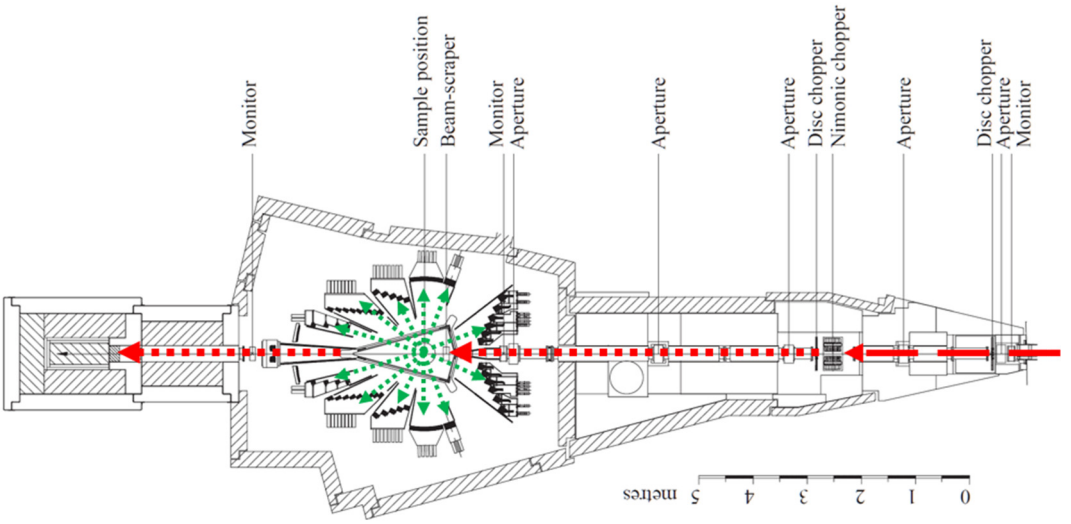

Figure A2.3 Incident (red) and scattered (green) trajectories of pulsed neutrons in the General Materials Diffractometer at the ISIS neutron source, at the Rutherford Appleton Laboratory in Oxfordshire, United Kingdom. Figure taken and modified from [76].

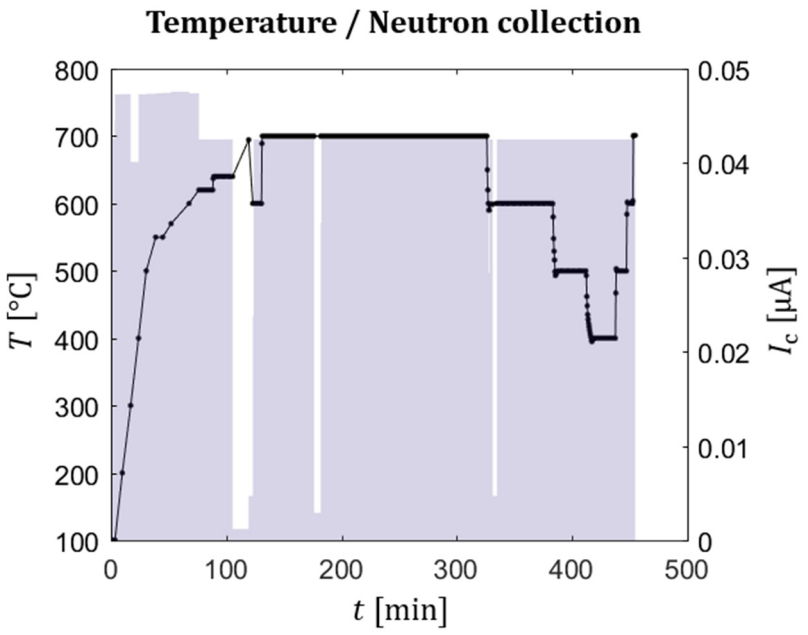

Figure A2.4 Sampling temperature and collective neutron yield with nearly constant colection current during 8 h.

A2.3. Results

At first, we examined the obtained spectra and compared those obtained from the different detector banks in terms of resolution and signal to noise ratio. Peaks assignment and final peak width at half-height of relevant the η-Fe_2Al_5 phase and the related α-FeAl phase is summarized in Table A2.2. Figure A2.5 shows a sequence of spectra obtained from detector bank 4. Peaks no. 22, 23, and 24 are appearing and growing in size.

Significant peak broadening was extracted from banks 4, and 5. Although quantification was not possible without knowing K, qualitative peak width evolution from both banks were consistent and significant for peaks 13, 15, 16, 20, 21, and 23. Corresponding d-spacing and β_{br} is listed in Tabel A2.2. Figure A2.6 underlines the finding that the broadening of the Bragg-reflex at 0.2055 nm corresponds to the c-axis the η-unit cell. Further examination revealed that peaks 13, and 15 as well as others, may show more complex peak width evolution. If significant, these preliminary findings may indicate the possibility to determine either recession of certain crystallographic directions, or more likely anisotropic defect accumulation in perpendicular directions to growth.

Table A2.2 Peak assignment of signal integrated over the duration of 700 °C hold. *Significant peak broadening. **Seemingly significant trends, yet more detailed evaluation is necessary.

Peak No.	d [Å]	β_{br} [Å]	I_{max} [μAs]	Phase
13**	1.027	0.030	674	FeAl [85]
15**	1.186	0.026	1668	Fe_2Al_5 [85]
16*	1.452	0.034	872	FeAl [85]
17	1.551	0.067	178	Fe_2Al_5 [85]
20*	2.055	0.044	4420	FeAl [85]
21*	2.147	0.172	370	Fe_2Al_5 [85]
23*	3.253	0.269	200	Fe_2Al_5 [85],[89]
24	3.885	1.364	146	Fe_2Al_5 [85],[89]

A2

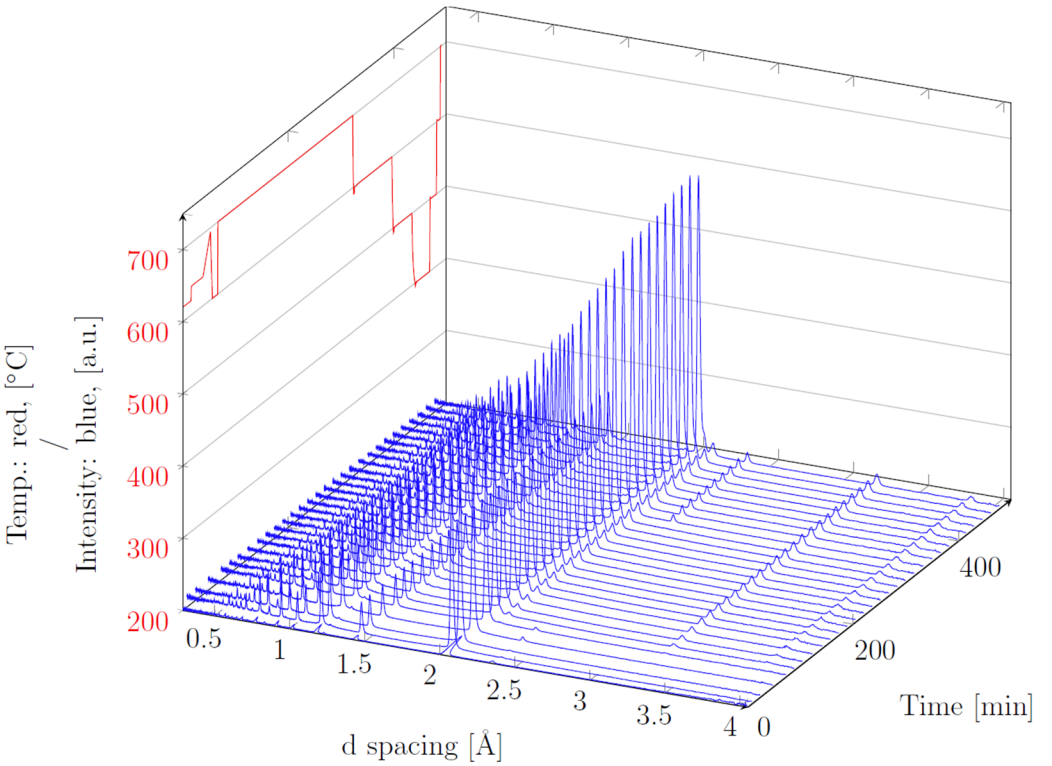

Figure A2.5. Stacked n-scatter spectra of Fe in contact with liquid Al. The signal at 2.3 Å belongs to the Al metal and vanishes as the temperature increases beyond the melting point. Peak no. 23, and 24 are well separated and visible to the right.

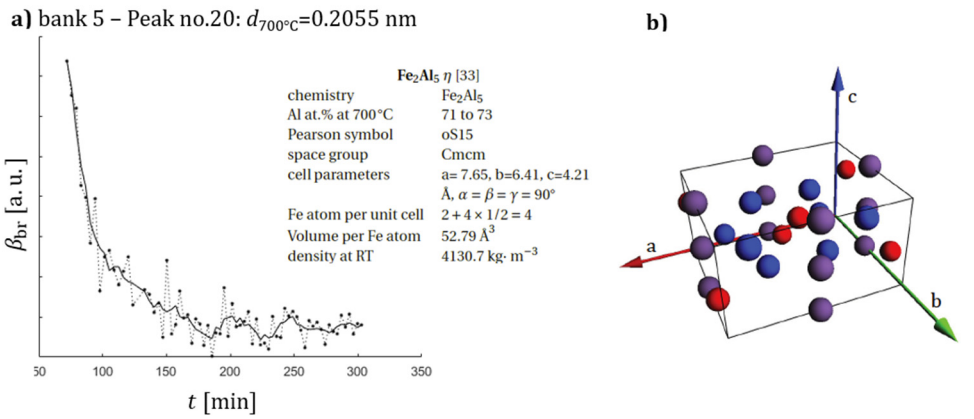

Figure A2.6. **a)** Evolution of neutron diffraction peak width during 700 °C temperature hold. **b)** Orthorhombic unit cell of Fe_2Al_5 with face centered Al sites and c-axis lattice parameter 0.421 nm. Adapted from [38].

In a recent study a model for the growth of the η-Fe_2Al_5-phase was presented that explained the sawtooth microstructure with nucleation, and growth into the iron substrate. They employed EBSD and transmission electron microscopy in conjunction with a cross-sectioning technique which allowed to analyze grain orientation and arrive at conclusions about the differential crystallographic stresses resulting from the advance of individual columnar η-grains deep into the solid iron microstructure. [75] Others had previously proposed anisotropic diffusion along the c-axis, possibly accounting for the deviations from parabolic growth rate.[30] These findings may be crucial evidence contributing to secured mechanistic understanding of non-standard growth kinetics and unexplained morphology of η.

A2

Chapter 3:
Coating deposition

3.1. Introduction

To exploit a higher surface to volume ratio for even faster heat transfer of LH-TES with Al alloys as PCM, the intermetallic interface reaction may be mitigated by the deposition of an inert barrier layer on the surface of encapsulations before introduction of the PCM. Such a barrier layer replaces the corrosion prone PCM-encapsulation interface with two new interfaces with distinct requirements. One is the interface of PCM and barrier layer, where the prerequisite is high resistance to the molten metal. On the other hand, a strong adhesion to the encapsulation is required in the presence of thermal cycles.

Protective coatings with the purpose of passivating steel against liquid aluminum have been introduced by hot dip aluminizing at 750 °C followed by a temperature treatment at 700 °C. The result was a thin layer of Al_2O_3 bonded to the steel substrate by 300 µm to 400 µm of Fe_2Al_5 and $FeAl_3$. This protective layer was stable to liquid aluminum attack during 10 days of immersion, while the control substrates were fully converted and dissolved in the Al bath within 10 h.[44] A combination of a similar hot dip step followed by plasma electrolytic oxidation has been used by Frutos et al. to give similar protective coatings, but with a thicker ceramic top layer.[90] The oxidation step was achieved with a custom-built 20 kW ceramic synthesis setup. These authors introduced a plasma discharge cathode into their aluminized cylinder to reach the high local temperature necessary to form a 40 µm thick ceramic layer, consisting

mostly of α-Al_2O_3. Overall layer thickness was approximately 500 µm and consisted of mostly Fe_2Al_5. Both approaches gave stable layers but produced thick aluminide layers as support for the presumably functional Al_2O_3 layer. Notably the Al rich intermetallic phases was reported to exhibit reduced thermal conductivity compared to the constituents, due to strong phonon scattering.[30]

Thin films of Al_2O_3 have been deposited by dip-coating, employing sol-gel chemistry for the preparation of a stable and viscous sol from $Al(iPrO)_3$ metal-organic precursor.[91] A single deposition has yielded films of 500 nm to 600 nm thickness. Heat treatment at 950 °C transformed the amorphous film to the refractory α-Al_2O_3 phase. Multiple deposition-annealing cycles have been employed to avoid cracking or spalling of coatings during crystallization/densification, in order to achieve a total α-alumina thickness of 10 µm by sol-gel dip-coating.[91] Generally, sol-gel dip coating yields dense, coherent thin films with homogeneous thickness, but requires long annealing at high enough temperature to transform the amorphous green coating deposited from metal-organic precursors into chemically stable crystalline phases.

Crystalline yttrium stabilized zirconia (YSZ) thin films up to 700 nm thickness have been deposited using aerosol assisted chemical vapor deposition in a continuous process. Deposition rates of 10-30 nm/min depend on substrate temperature, carrier gas composition and flow rate. Annealing temperatures between 600 and 1000 °C for 20 h have been reported. [92] The method additionally requires constant flow rate of the precursor aerosol, which may limit scalability and application to 3-dimensionally shaped substrates.

Porous ceramic YSZ membranes thicker than 1 µm have been prepared by a single dip-coating step from stabilized particle suspensions. Polycrystalline commercial YSZ powder was dispersed in dilute aqueous nitric acid (HNO_3), treated by ultra-sonication, and further refined by ball milling for 7 days. Grain size distribution of 50-100 nm were characterized by SEM. Suspension stability had been found best between pH 3-4, assessed by comparing the sedimentation height at a fixed time.[93]

3.1.1. Colloidal processing

Electrostatic stabilization of colloidal particle suspensions requires sufficiently high charge density. The pH of the dispersing solvent has therefore to be adjusted with regard to the Iso-Electric Point (IEP)*. Table 3.1 summarizes IEPs of some ceramic materials.[94]

Table 3.1. Collection of pH values of zero surface charge for several ceramic materials in aqueous solution.[94]

Material	IEP
α-Al_2O_3	8-9
$3.Al_2O_3.2.SiO_2$	6-8
$BaTiO_3$	5-6
CeO_2	6.7
Cr_2O_3	7
CuO	9.5
Fe_3O_4	6.5
La_2O_3	10.4
MgO	12.4
MnO_2	4-4.5
NiO	10-11
SiO_2 (amorphous)	2–3
Si_3N_4	9
SnO_2	7.3
TiO_2	4-6
ZnO	9
ZrO_2	4-6

Deposited colloidal particle layers are initially dried at low temperature, to allow the solvent to escape without altering the as-deposited microstructure. In some cases, a calcination treatment at ca. 400 °C removes non-volatile organic additives like

* The IEP is the pH at which the surface of a suspended particle is on average neutral. To achieve stable suspension, one has to choose a pH far away from the IEP.

polymeric surfactants.[94] Sintering is usually done above two thirds of the homologous temperature (T_{rm}), but never below 0.4 T_{rm}, see Eq.(3.1).

Eq.(3.1) $$T_{rm} = \frac{T}{T_m}$$

For steel substrates, Eq.(3.1) poses serious problems if high melting ceramics should be compacted by sintering. The introduction of an inter-granular phase which cures below the maximum service temperature of steel can be an alternative. Aqueous Na_2SiO_3 solution has been used as binder, effectively hardening and forming strong monoliths with varied filler compositions of Al_2O_3, silicon dioxide (SiO_2), titanium dioxide (TiO_2), iron(III) oxide (Fe_2O_3), manganese(IV) oxide (MnO_2), magnesium oxide (MgO), calcium oxide (CaO), sodium oxide (Na_2O), potassium oxide (K_2O), phosphorous oxide (P_2O_5), and sulfur oxide (SO_3).[95] Non-stoichiometric sodium silicate ($nNa_2O.mSiO_2$) has been investigated as corrosion protection layer, applied by dip-coating to galvanized steel.[96] The authors concluded that deposition from solutions with m/n in the range of 1.5-2 gave the densest coatings, but did not clarify how porosity was quantified. However, they indicated that higher ratios of m/n should allow for a higher degree of polymerization in the $nNa_2O.mSiO_2$-sol, which was confirmed by ^{29}Si Nuclear Magnetic Resonance (NMR) spectroscopy.

The glass transition temperature (T_g) of the binder phase is of interest when a barrier layer for high-temperature cycle conditions is derived from a filler phase that does not match the thermal expansion coefficient of the substrate (Table 3.2). The $nNa_2O.mSiO_2$ system has been investigated by DSC and dilatometry, finding that T_g varied within [410°C…510°C]† for n=1, and $m/(n+m):=x_{SiO_2}$ within [0.5…1] (Figure 3.1). A similar dependence was found in the ternary non-stoichiometric iron sodium silicate ($pFe_2O_3.nNa_2O.mSiO_2$) with m/n fixed at 81/19. When the weight fraction (f_{wt}) of Fe_2O_3 was varied within [0…0.18] they found T_g varying within [460°C…520°C], with the variation being less pronounced at higher concentrations.[97]

† [Y_1…Y_2] denotes the interval between Y_1 and Y_2

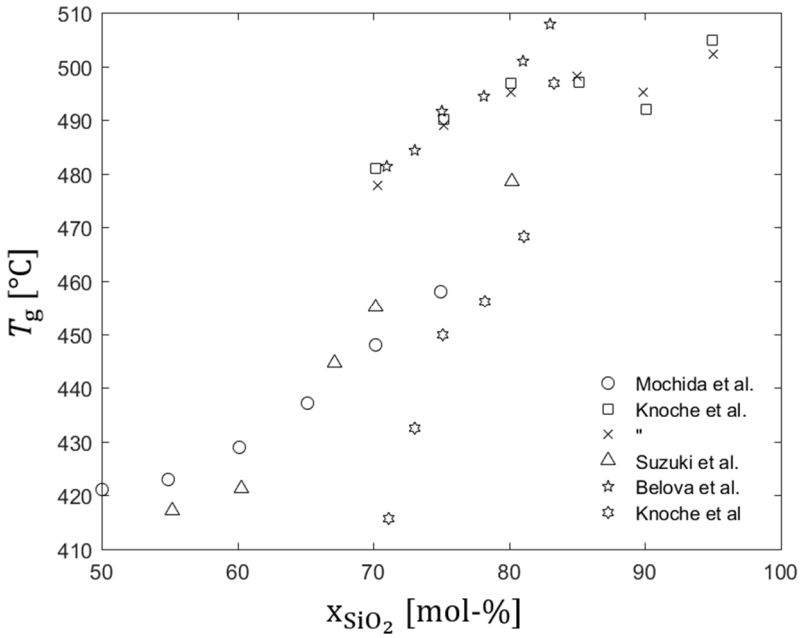

Variation of the glass transition temperature in the $nNa_2O.mSiO_2$ system. The mole fraction (x_{SiO_2}) is equal to m/(n+m). Data collection is cited from Belova et al.[97] Figure 3.1

Selection of thermal expansion properties of metals and ceramics. $< \alpha >$ is the average thermal expansion coefficient at ambient condition. Further values refer to the anisotropic lattice directions. Table 3.2

	Material	$< \alpha >$ [ppmK^{-1}]	α_1 [ppmK^{-1}]	α_2 [ppmK^{-1}]
Metals	Al	23[98]		
	Si	3.2[99]		
	Al-12%Si	19-20[98]		
	316L	15.9[28]		
Ceramics	Al_2O_3	5.4[100]		
	ZrO_2	9.5[101]		
	AlN	3.1[100]		
	h-Si_3N_4	1.6[99],[100]		
	h-BN	14.2[102]	30[103]	-3[103]
	Graphite		20[103]	-1[103]

3.1.2. Refractory material selection

The barrier materials should be chemically stable in the environment around T_m of the PCM. They should resist chemical attack by the molten PCM, as well as reactive gaseous species originating from the heat transfer fluid (mostly O_2, and CO_2). Ultimately, the coating should efficiently limit inter-diffusion and reaction of encapsulation elements and PCM at minimal thickness. The oxidation of Al by O_2 (Eq.3.2) favors the metal oxide over a wide temperature range, judging by the Gibbs free energy.

Eq.(3.2) $$\frac{4}{3}Al + O_2 \rightarrow \frac{2}{3}Al_2O_3, \Delta G^0_{800\,°C} \sim -900\ kJmol^{-1}$$

Using the Ellingham diagram (Figure 3.2), one can predict the metal oxides that are thermodynamically favored, when competing in redox reaction with Al_2O_3, i.e. CaO should be stable against reduction by molten aluminum over a wide temperature range (see Eq.3.3).

Eq.(3.3) $$2Ca + O_2 \rightarrow 2CaO, \Delta G^0_{800\,°C} \sim -1050\ kJmol^{-1}$$

However, this condition may not be sufficient when considering the specific reactivity of, say, CaO towards atmospheric H_2O.

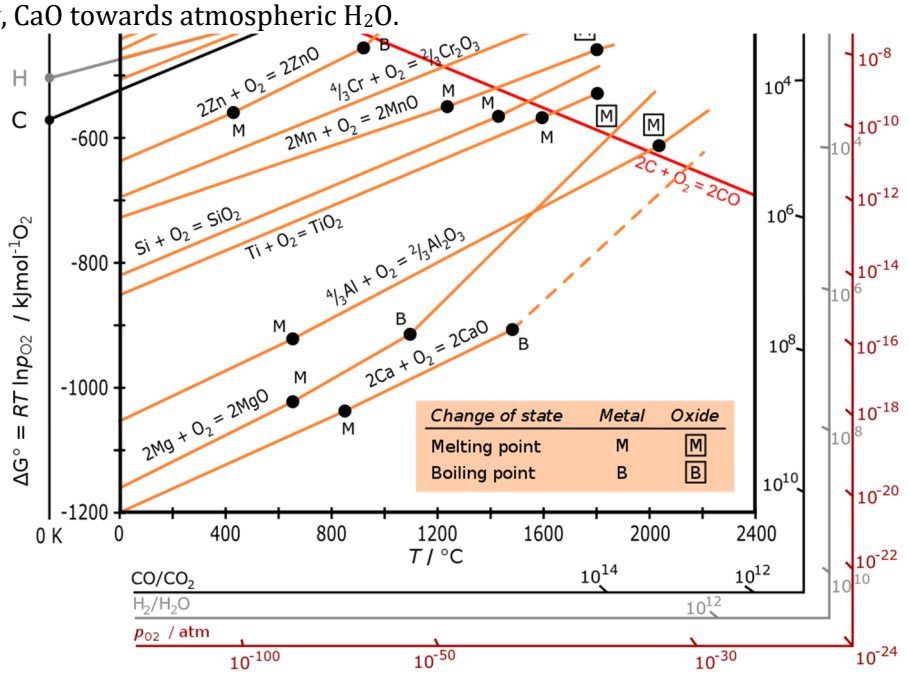

Figure 3.2 Ellingham diagram for ceramic metal oxides with respect to their corresponding metal and oxygen. Taken and modified from [104].

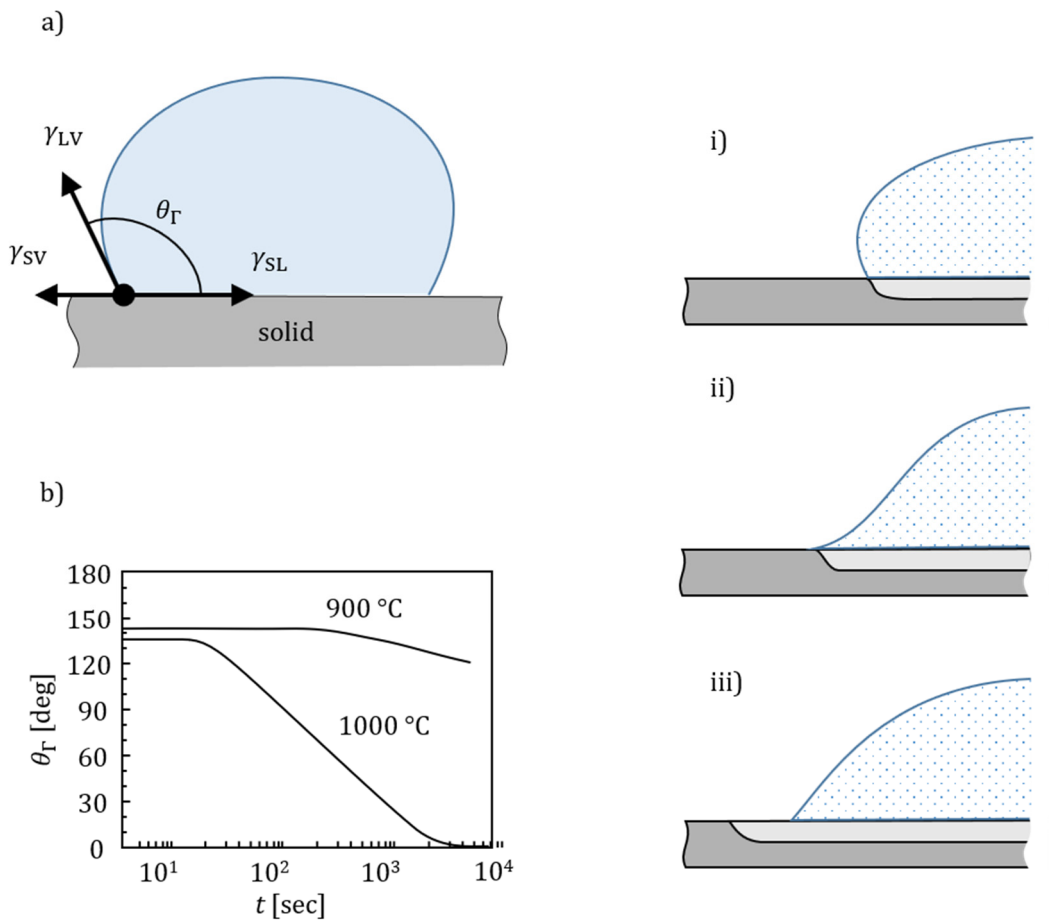

a) Interface energy balance determining the ideal equilibrium wetting angle. **b)** Reactive wetting angle of *h*-BN with liquid Al with time and temperature dependence. Decrease of $\theta_\Gamma(t)$ at 1000 °C proceeds via i) initiation ii) continuous formation of AlN and iii) depletion/saturation. Data adapted from [33].

Figure 3.3

In practice, ceramic compounds have been identified that have use as refractory material for Al melts, due to combinations of energetic and kinetic properties. Stability in agreement with energetic considerations has been experimentally confirmed for bulk alumina and zirconia in molten aluminum to 1000 °C.[26] *h*-BN, and *h*-Si_3N_4 have been found practically inert to liquid aluminum attack, despite not being thermodynamically stable.[26] AlN is chemically stable against liquid Al up to 2000 °C in reducing atmosphere, and up to 1000 °C in dry air.[105] *h*-Si_3N_4 and *h*-BN have been reported to form an AlN layer at the interface with Al melt, which increases wettability.[106] The wetting angle (θ_Γ) in this case has been determined to be time

dependent (Figure 3.3b). This has been ascribed to kinetic AlN layer formation, which mediates wetting. Figure 3.3a show the interface energy/force balance which determine θ_Γ (in the stationary case). The wetting of *h*-BN with Al (shown in Figure 3.3b) can be explained in terms of the energy balance in a) if one considers wetting angle during the stationary initiation phase i) to be that of *h*-BN/Al and the one in iii) that of AlN/Al. Similar results have been obtained for the reactive wetting of graphite by Si[107], Si_3N_4 by Si[108], Sapphire‡ by Al[108], SiC by Al[108]. A similar picture the stagnant wetting of BN by Al (iii) has been drawn in the case of graphite wetted by Si.[108] The mediating layer extended beyond the final location of the triple phase boundary, which was explained by its propagation via diffusion of the wetting metal in-plane of the reaction layer.

No individual materials fit all requirements for a resilient and effective diffusion barrier. Beside energetic and kinetic stability towards the PCM mechanical compatibility or adhesion may play a key role. For example, AlN layer formed in the reactively wetted systems have been consistently thin, the material has an attractive thermal conductivity, and is reported as widely inert to molten Al. However, the large thermal expansion mismatch (Table 3.2) make it unlikely the material to yield coatings that are tolerant to the expected thermal cycles.

3.2. Experimental

Inert ceramic barrier coatings were deposited from particulate suspension, using a scalable reverse dipping method derived from the same principle as the popular dip-coating approach. The ceramics in Table 3.3 were tested as diffusion barrier coating separating liquid Al-12%Si from the encapsulating substrate. Stainless steel cylinders had a nominal composition of Fe-17wt%Cr-10wt%Ni-1.2wt%Mo-1.1wt%Mn (316L), and were 20 mm in outside diameter and 16 mm inside diameter (OD20t2). The selection of coating materials was based on thermal stability and chemical inertness. Test depositions were prepared from either metal-organic sol,

‡ Sapphire is single crystal Al_2O_3. Here the wetting angle did not decrease below 90 °. The change in θ_Γ from 150 ° to 110 ° has been attributed to the removal of surface Al_2O_3 layer of lower crystallinity.

ceramic powders, or a combination of the two. In some test's poly-(ammonium acrylate) was used as poly-ionic, steric dispersant.

Summary of ceramic particles used in this study. Table 3.3

Formula	Supplier,	description	Average size [nm]
α-Al_2O_3	ABCR,	powder, <1µm	214
t-ZrO_2	Sindhauser,	aq. dispersion	
h-Si3N4	ABCR,	powder, <5µm	290x3200
h-BN	ABCR,	powder, <1µm	19x4300
h-BN	ZYP,	EtOH/acetone dispersion	

3.2.1. Particle characterization

Particle size distribution was calculated from SEM images of supplied powders and conductive graphite tape, cf. Figures 3.4 and Figure 3.5. Secondary electrons were detected (Everhart-Thornley detector) operating the electron microscope (Zeiss Merlin, Gemini-I or -II) at vacuum, and at 1 kV acceleration voltage. Evaluation of the digital images was done in ImageJ by manually selecting particle boundaries along randomly oriented straight lines. At least 200 particles were evaluated for each of the supplied powders.

Composition of $nNa_2O.mSiO_2$ aqueous sols prepared as binder and dispersant for electrostatically stabilized colloidal suspensions of various ceramic particles. Table 3.4

NaOH		SiO_2		H_2O		$nNa_2O.mSiO_2$(aq.)	
mass	n	mass	m	mass	n_{H_2O}	Total mass	x_{SiO_2}
[g]	[mol]	[g]	[mol]	[g]	mol	[g]	[-]
20	0.25	31	0.516	76.5	4.3	127.5	0.508
20	0.25	40	0.666	90	5.0	150	0.571
20	0.25	45	0.749	97.5	5.4	162.5	0.600

3.2.2. Dispersion procedure

Aqueous $nNa_2O.mSiO_2$ solution was prepared by first dissolving NaOH (99%, anhydrous) in the prescribed amount of H_2O, necessary to yield the desired composition of x_{SiO_2} within [0.5…0.6] (Table 3.4). The dissolution was exothermic and cooling in a water bath was applied while the solution was stirred magnetically. Once dissolution was complete and the temperature fell below 40 °C addition of SiO_2 (<50 μm, amorphous, chromatography grade purity) was added in portions. Fast addition would lead to a slow dissolving chemically sintered silica pulp inhibiting magnetic agitation, and ultimately prolonging the time until dissolution. Heating was applied towards the end to facilitate dissolution when the solution was almost saturated. pH of all prepared $nNa_2O.mSiO_2$ solutions was on the alkaline limit of the indicator (>11). Solid content of the water glass was adjusted to be 40 % in all cases. Particles were added to the $nNa_2O.mSiO_2$ solution up to a highest solid loading of 65 %, by mass. All three types of particles were immediately wetted by the solvent and dispersed well when aided by mechanical stirring and ultra-sonication (Emmi-HT550, 250 W). After that, SiO_2 beads were added as milling media and the plastic containers were ultra-sonicated while rotation was effected by a mechanical stirrer for at least 1 h. The mass of the milling beads did not change by a measurable degree when checked after 48 h of milling. For the *h*-Si_3N_4 dispersion it is important to note a distinct onset of small amounts of gas evolution as evidenced by bubble formation after 5-7 days. This was confirmed on independent reactions and was not linked to the degree of stirring. The gas evolution was associated with the distinct odor of ammonia, however the extent of gas escaping was small as judged by the bubble formation and leveled off quickly. Mass balance of the entire reaction vessel confirmed that the amounts of ammonia escaping were negligible. The pH of the highly loaded dispersions was unchanged after several weeks, however the strong particle solvent interaction prevented almost the reaction of the indicator paper in some cases.

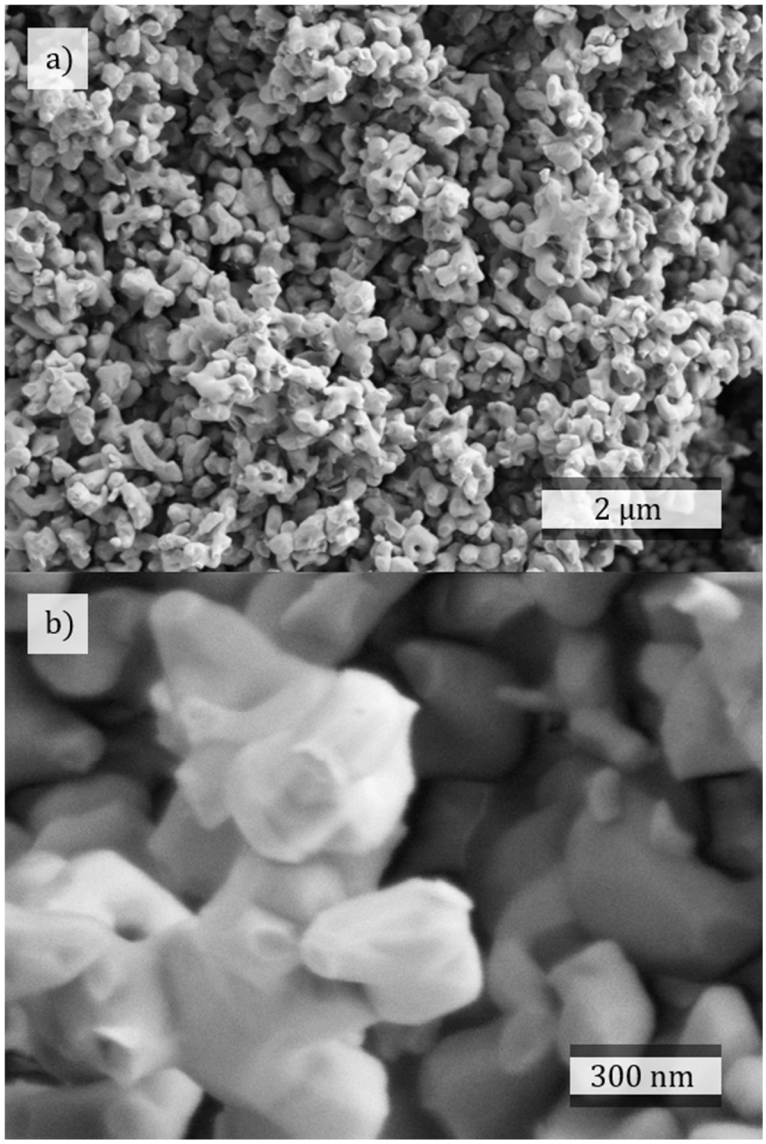

Figure 3.4

Secondary electron image of α-alumina particles, as received, deposited on conductive graphite tape. **a)** Agglomerates of facetted crystallites with aspect ratio close to unity. **b)** A large agglomerate of multiple polygonal crystallites inspected at high magnification, showing strong neck formation connecting grains of 200-300 nm diameter.

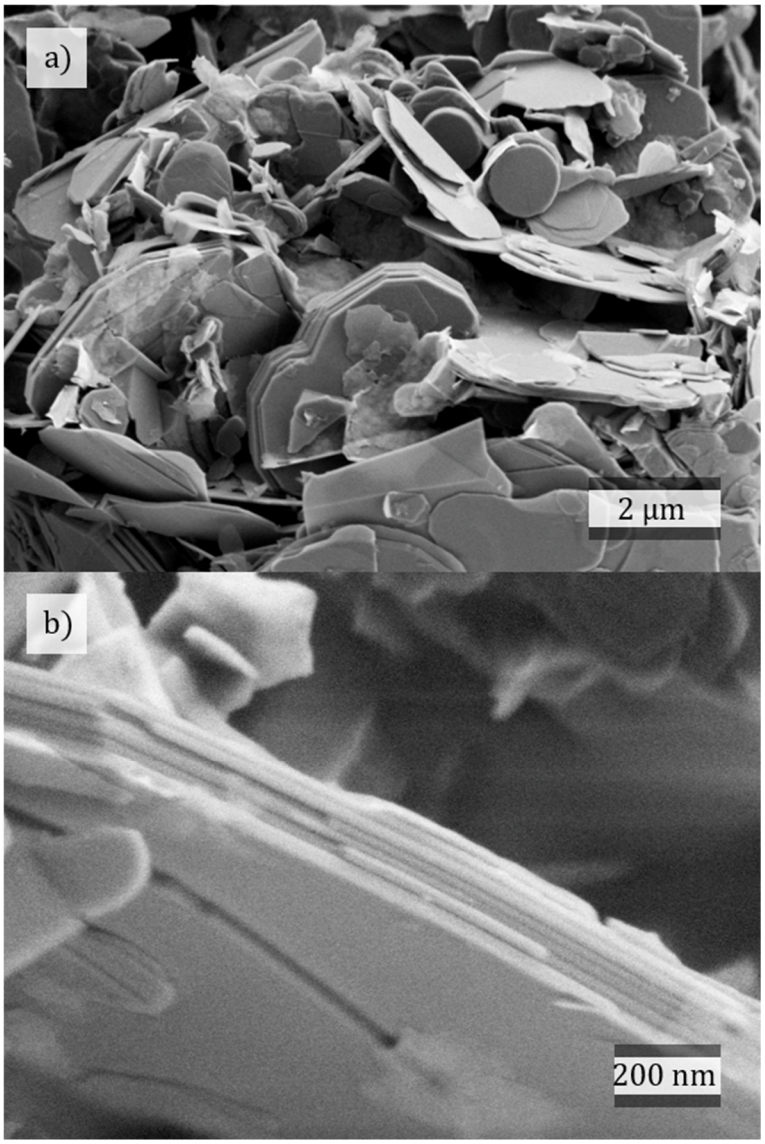

Figure 3.5 Secondary electron image of hexagonal boron nitride particles. **a)** Agglomerate of layered crystalline platelets with extremely high aspect ratio. **b)** Close up magnification of a large boron nitride plate-like crystal revealing a stack composing seven crystallites of 51 nm average thickness.

The suspended precursors were deposited on the inner surface of the cylinders on a length of 50-60 mm. The coating substrates were kept stationary, similar to the reverse dip-coating procedure demonstrated by other authors.[109] Key modification in the procedure presented in this work was the pumping of the precursor suspension into the inner volume of the hollow cylinders (Figure 3.6). In this way, only the inside surface of the hollow cylinders is coated, resulting in efficient use of the coating precursor. Planar substrates were coated inside a transparent syringe with removed piston replacing the hollow steel substrate as injection volume. This allowed the substrate to be fixed vertically within the cylinder and the process could be observed, as our suspensions did not adhere well to the transparent plastic syringe.

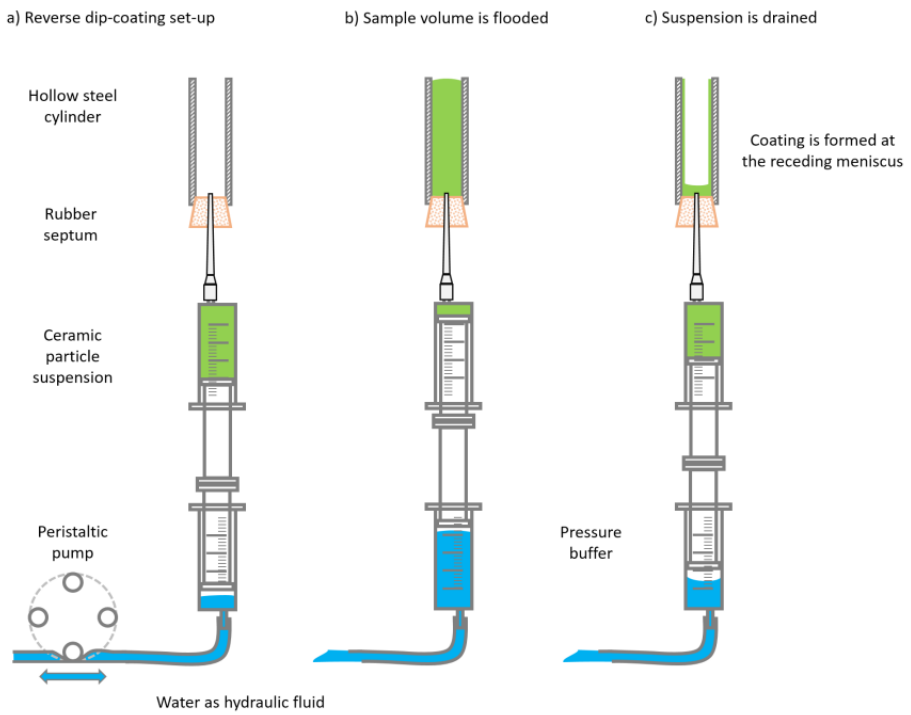

Figure 3.6 Injection-retraction procedure for coating deposition of sols and particulate suspension, making use of two plastic syringes and a peristaltic pump for smooth meniscus movement control. A gas bubble in the lower syringe-piston is shown expanding/shrinking as it absorbs dynamic changes in pressure. **a)** Empty hollow substrate equipped with rubber stopper and suspension inlet. **b)** Completely suspension flooded substrate cavity, before retraction of the coating precursor. **c)** End of the injection-retraction procedure with indication of receding meniscus and deposited coating material.

The thickness and microstructure of the coating are determined by the velocity of the meniscus, viscosity of the liquid, and evaporation and condensation processes, similar to dip-coating. Planar substrates were dried at ambient overnight and annealed at 800 °C for 5 h, or calcinated at 400 °C for 2 h. Heating to the respective holding temperature was done at 1 K/min. Coated and annealed CroFer® substrates were heated at 40 K/min to 800 °C and equilibrated. The adhesion of the coatings was put to the test by abrupt removal of the substrate from the furnace and placement on a calcium silicate refractory at ambient temperature. Cross-sections were prepared from coated single crystal Si-wavers (at CMI, Switzerland) or hardened tool steel blades (9 mm, NT Cutter, Japan). These two materials allowed for preparation of brittle fracture surfaces without plastic deformation of the substrate.

Coated encapsulations were prepared from 316L cylinders with outside diameter 30 mm and 2 mm wall thickness. A cylinder length of 12 cm was coated and calcinated at 400 °C. For deposition, cylinders were aligned vertically, and the lower opening closed with a rubber stopper. The injection volume was flooded completely with the suspension at maximum speed and after few seconds drained with controlled speed. Meniscus velocity was varied between 0.5 and 2.5 mm/s, by adjusting the volume flow rate of the hydraulically connected peristaltic pump (Heidolph, HEIFLOW). Al-12%Si was cast directly into the calcinated, coated encapsulation from a melt crucible held at 750 °C. Coatings were inspected by SEM and light microscopy of cross-sections prepared from PCM filled cylinders or empty ones by embedding in conductive resin. The coating thickness was determined from individually calibrated light microscopy images. Two orthogonal diameter measurements with 10 µm precision were used as calibration for each cylinder cross-section individually. Using the measurement precision as maximum absolute error of the diameter gave a relative calibration error of below $3 \cdot 10^{-4}$. Thickness values were calculated as average of at least 9 independent measurements. These lab-scale encapsulations held more than 150 g of aluminum alloy each. The column exerted an approximate hydrostatic pressure at the lower end of 3.2 kPa, when using 2640 kg/m^3.

Larger volume encapsulations for resistance to prolonged liquid metal attack were prepared by deposition on cylinders with 32 mm outside diameter, 2 mm wall thickness, and 74 cm length. Injection and draining of the large internal volume was effected using compressed air rather than a peristaltic pump. Calcination was done by forcing a 400°C hot air stream through the cylinders. A conically machined plug from porous refractory calcium aluminum silicate sealed all cylinders. The eutectic PCM Al-26%Cu-5%Si with a melting point of T_m=525 °C was used, for system design considerations.[18],[19] The cyclic boundary conditions in this test bed were given by $T_{min/max}$=30/550 °C, $p_{min/max}$=1/9 bar. Total PCM mass was 525 kg, of which 12 kg was encapsulated in boron nitride coated cylinders. After an initial pre-heating phase of several days, 5 charge-discharge cycles were completed (Figure 3.7).

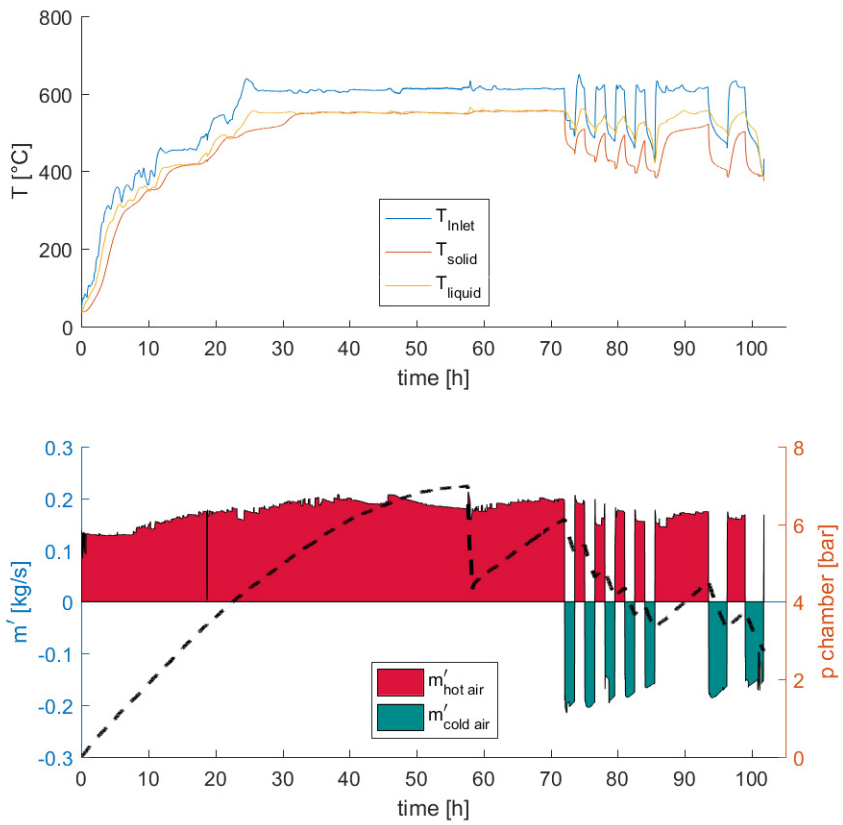

a) Temperature and **b)** pressure sequence in application scale test of boron nitride coated 316L steel encapsulations containing Al-26%Cu-5%Si phase change material.

Figure 3.7

3.3. Results

3.3.1. Boron nitride diffusion barrier

No thermal cracking or delamination was observed with boron nitride coatings in the initial lab scale thermal shock tests. Consistent coating quality was obtained by deposition at a velocity of 1.7 mm/s. Isothermal holds for more than 100 days exposed to liquid Al-12%Si did not penetrate the *h*-BN layer, as is evidenced by constant thermo-physical properties of the PCM in DSC measurements (Figure 3.9), as well as absence of Fe, Cr, and Ni signals in EDX spectra obtained on polished PCM surfaces in post-exposure cross-sections (Figure 3.8). In the uncoated control experiment h_f decreased by 60 Jg^{-1} (14 %), and Fe signals in cross-sections reached up to 3 % under similar conditions. No adhesion of the aluminum alloy to the *h*-BN was observed and when permitted by the geometry of the section, solid PCM cylinders often fell out of the encapsulation segment.

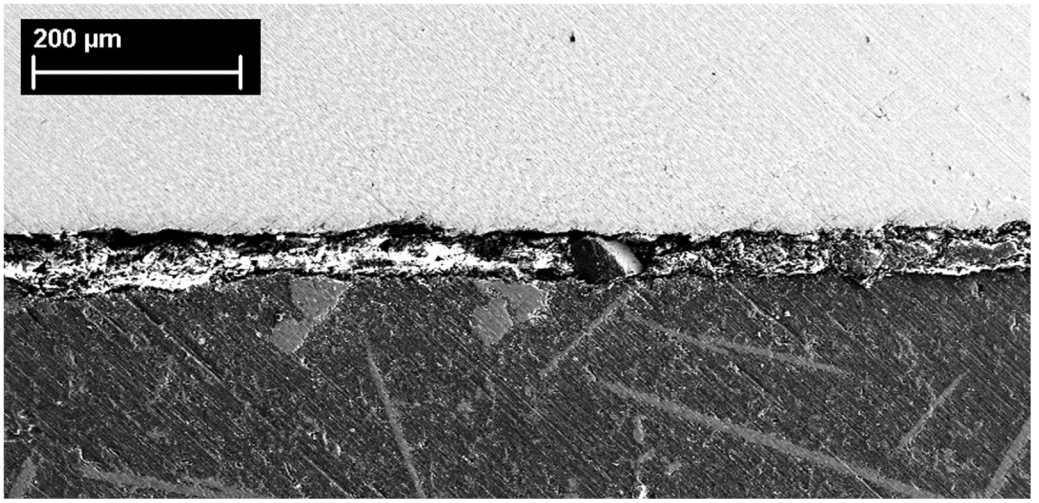

Figure 3.8 SEM image showing boron nitride layer sandwiched between Al-12%Si and 316L stainless steel after exposure to the aluminum melt for a few days. The layer shown is 63 µm thick.

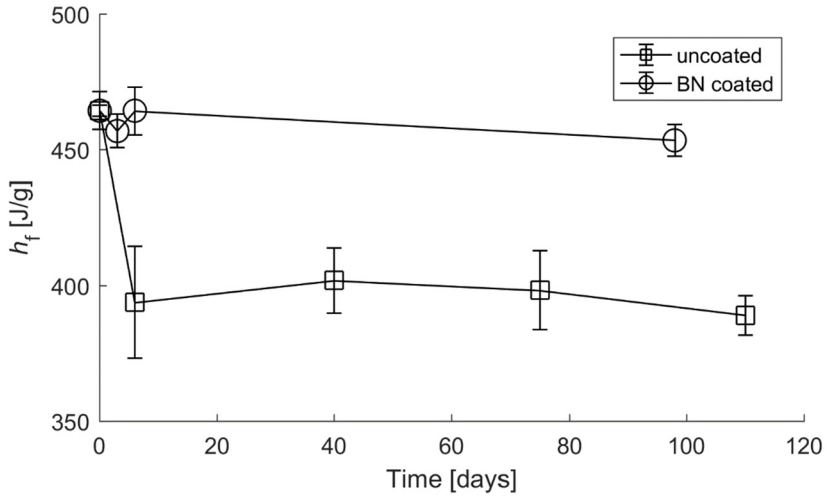

Figure 3.9 h_f from DSC of Al-12%Si alloys exposed to 700 °C for varying times. One can see that the mass specific heat of fusion is conserved for the BN protected alloy. The unprotected alloy suffers a drop in h_f of 14 %.

3.3.2. Sealing using porous calcium silicate and capillary force

The developed porous ceramic seals (Figure 3.10) alleviated the need to coat complex or exposed sites at the ends of the cylinder. The porous calcium silicate substrate filling the cylinder openings did not show fissures in post mortem cross-sections. Liquid PCM was prevented from penetrating across the sealing by the high energetic cost of wetting BN coated surfaces on either side of the gap between steel and seal. Static load from the liquid Al-12%Si column did not lead to leakage during 100+ days under isothermal lab conditions.

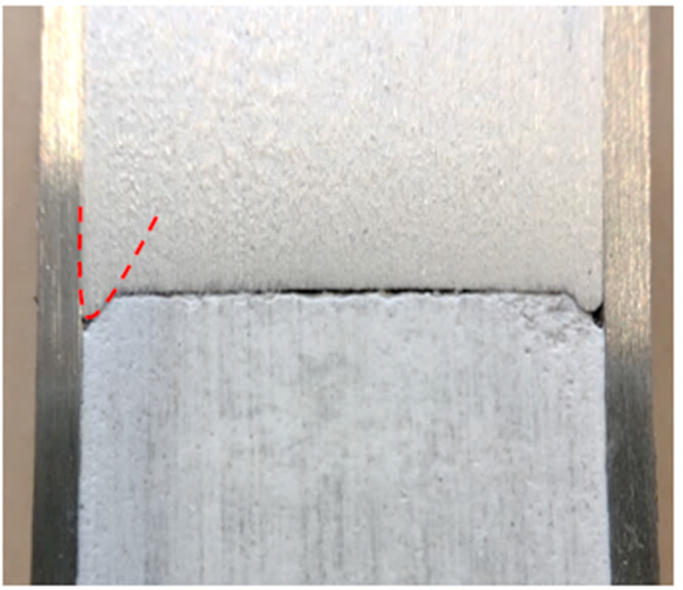

Figure 3.10 Longitudinal section of BN coated tube after exposure to molten Al-12%Si alloy at 700°C.

3.3.3. Scaled field test with temperature and pressure cycles

Barrier coatings tested on application scale and deposited from commercial BN suspension with the developed injection method prevented loss of LH-TES capacity of 90 % compared to the control group (Figure 3.11). These coatings were homogeneously thick, averaging at 76 µm. From 384 independent measurements, a standard deviation of 19 µm was calculated. Coatings were off-white when deposited, gray after calcination, and completely white after annealing. Figure 3.12 compares the cross-sections of encapsulations with and without coating. The microstructure is visibly changed in the control sample and formation of an intermetallic layer at the interface can be seen be the naked eye. The coated sample is free of visible corrosion.

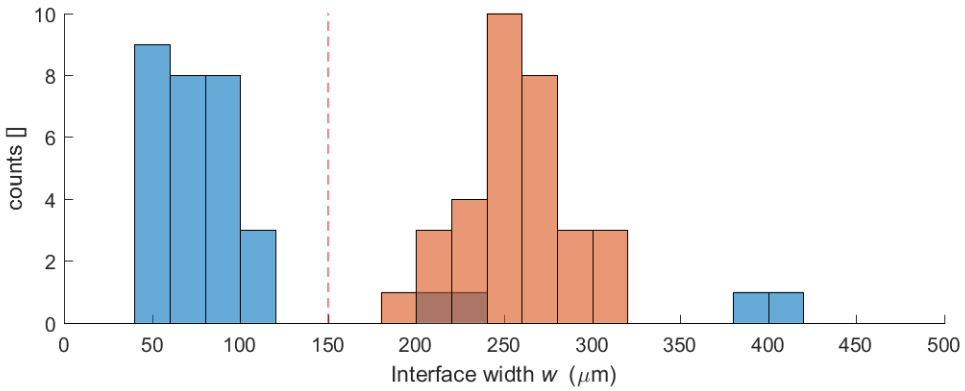

Comparison of interface layer thickness of coated (blue) and uncoated (orange) tubes. Without coating, an intermetallic layer thickness of 256 µm with a standard deviation of 29 µm was observed. BN coatings were 76 µm on average, with standard deviation of 19 µm. Out of 32 tubes, 4 showed locations were intermetallic developed while the BN was removed. Overall, the coated tubes showed 10 times less intermetallic layers compared by average thickness.

Figure 3.11

3

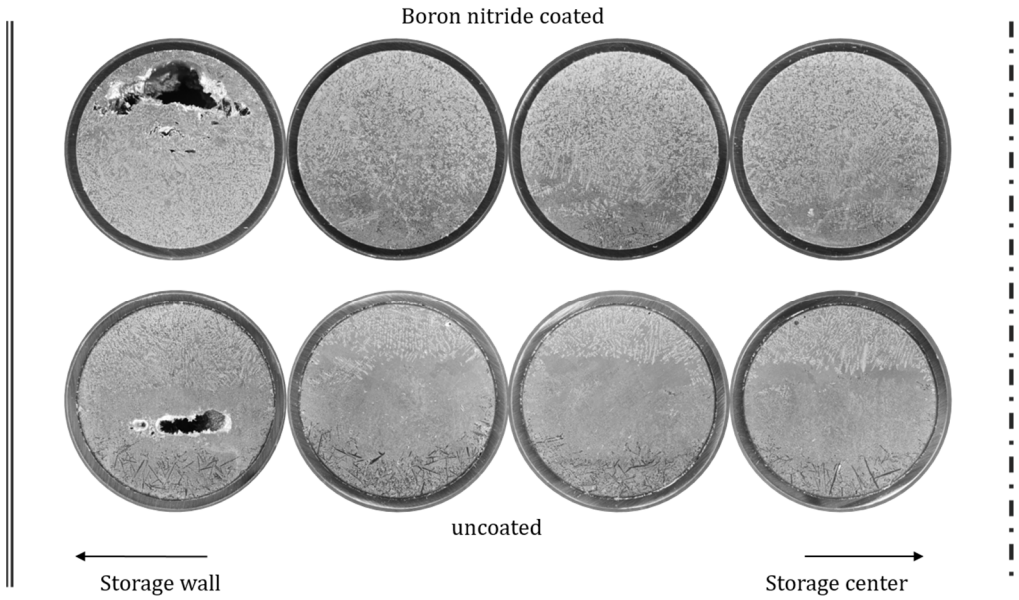

Cross sections of scaled up cylindrical encapsulations containing Al-26%Cu-5%Si PCM after testing under combined temperature and pressure cycles. The upper row shows a *h*-BN coated sample with relatively homogeneous eutectic microstructure. The control sample on the lower row exhibits intermetallic layer formation and phase segregation.

Figure 3.12

3.3.4. Silicon nitride derived sealing compound

Coatings deposited from *h*-Si_3N_4 suspensions on steel were extremely resilient to bending of the substrate and to thermal shock. Both dried and annealed layers tolerated repeated bending of the steel substrate to approximately 10 cm radius without showing signs of delamination. Even lower elastic bend radii were applied during fracture of the steel blade for cross-sectional imaging. The $nNa_2O.mSiO_2$ binder appeared amorphous in dry coatings in cross-section (Figure 3.13) and top view (Figure 3.14).

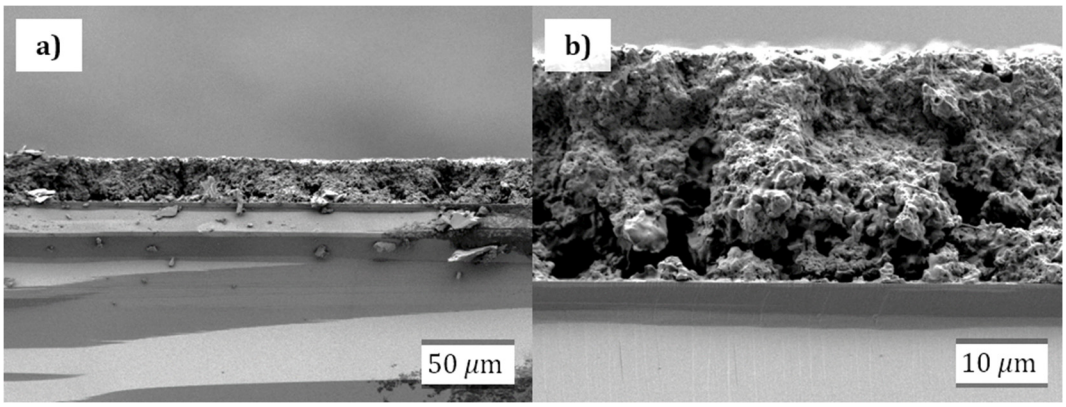

Figure 3.13 Cross-sectional microstructure of deposited *h*-Si_3N_4 layer on Si single crystal showing excellent bonding between substrate and coating. **a)** Homogeneously thick layer reaches close to the edge of the fractured substrate. Facets in the fracture surface of the substrate result from Si single crystal orientation. **b)** Dense coating of 26 µm thickness synthesized in a single coating step appears equally well to adhere on the substrate.

The microstructure of *h*-Si_3N_4 shows hexagonal facetted grains surrounded and bonded together by a continuous amorphous phase. Microstructural changes occur during annealing and enhance the layered appearance of the *h*-Si_3N_4 (Figure 3.14d). At the same time, the annealed layer appears compacted, compared to the as-dried state. The amorphous state of the inter-granular phase persisted throughout the experiments, including a reduced-scale liquid Al attack test during 2 days. After this time, the layer was intact and no iron aluminide had formed on the substrate. Some gray round stains of few mm diameter had developed on the otherwise beige *h*-Si_3N_4. This may be attributed to reduction of the amorphous binder[44, S. 2], or formation of AlN and deposition of mixed oxides. The layer was however adherent and unchanged in thickness, despite the stains.

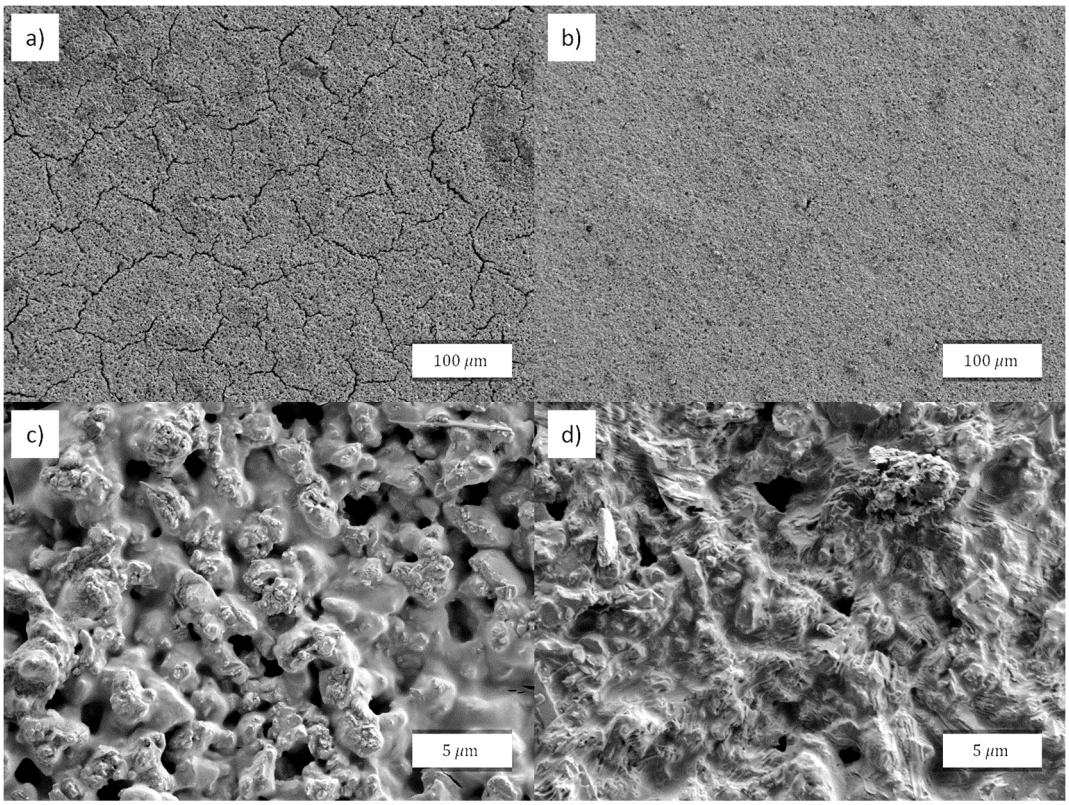

Deposited *h*-Si_3N_4 coating **a/c)** before and **b/d)** after annealing at 700 °C. Top view microstructure of as deposited films show open porosity. The crystalline particles are completely wetted by amorphous sodium silicate binder phase. Layers of hexagonal crystals after heat treatment appear as jagged edges through the binder at high magnification.

Figure 3.14

Procedures for the deposition of inert ceramic coatings onto metal surfaces were established from particle suspensions containing *h*-BN and *h*-Si_3N_4. High relative velocity of the suspension to the substrate was found to be a critical parameter in obtaining homogeneous, well adherent thick films. Solvent front velocities of 2 - 4 mm/s gave good results, while lower speed led to partly flocculated, uneven depositions. This was attributed to the thixotropic effect resulting from electrostatic gelling. Shear thinning reversibly breaks up the gel-network. Oscillatory viscosity measurements confirmed a shear speed dependent transition from viscoelastic to viscous deformation behavior (Figure 3.15). The nature of the stabilizing forces in the suspension remains however ambiguous. Both electrostatic and steric repulsion are favored in this system, considering either the IEP of amorphous SiO_2 (Table 3.1) or the possibility of ($nNa_2O.mSiO_2$)-oligomers absorbing on the particles.

Amorphous alumina coatings were well adherent and showed no reaction to the thermal stress sequence, but did not exhibit any delaying effect to liquid metal corrosion. Coatings containing amorphous alumina as binder phase and having a bulk phase of refractory α-alumina cracked and spalled in the thermal stress sequence, as did coatings with Si_3N_4 as refractory barrier phase.

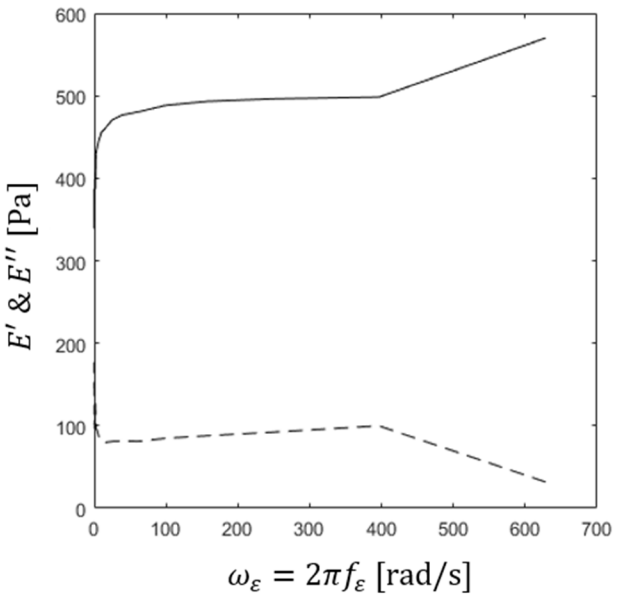

Figure 3.15 Aqueous particle suspension exhibits a step transition between storage and loss modulus in the low frequency range. Gelling occurred after few seconds of standing and is reversibly broken through agitation. No sedimentation occurred in aqueous suspensions with Al_2O_3 particle loading higher than 40 % by weight and pH above 11. Sodium silicate oligomers acted as surfactant and binder.

3.4. Summary and conclusions

The resilience of boron nitride coating in the thermal stress sequence and regarding liquid metal attack is best among the investigated materials. Chemical stability is inherently good and most likely aided by the non-wetting properties towards liquid metals. Thermal expansion mismatch between steel and h-Si_3N_4 was overcome by the addition of an inorganic, amorphous binder phase. This binder was derived from cost effective aqueous $nNa_2O.mSiO_2$ solution, and at the same time, served as dispersant for the refractory crystalline particles. Viscoelastic properties of the stabilized suspension show the colloidal nature of the system. Although h-Si_3N_4

particles are larger than 1 µm in the *a*x*b* plane, the thin platelets can be stabilized based on their minimum dimension in direction of the *c*-axis. This is consistent with state of the art colloid research.[94] In the second case a mixed steric-electrostatic stabilization mechanism could be the case. The chemical interaction of alkaline media on Si_3N_4 has been subject to investigations in recent years.[110] It would be interesting to investigate the precise composition of the amorphous phase after deposition for the formation of Si-(Na)-O-N compounds, and the *h*-Si_3N_4 crystallites for intercalation of the dispersant into the layered crystal. Exfoliation of *h*-Si_3N_4 has been considered unlikely, but similar treatments for *h*-BN by ball milling and ultra-sonication in urea has been proven successful recently.[111]

The injection method was found to be a versatile and scalable tool for the deposition of inorganic barrier layers on hollow cylindrical steel substrates. This geometry is highly relevant for the technology of LH-TES in encapsulated metal PCM. Scale up has been demonstrated spanning two orders of magnitude. Coatings obtained from the presented deposition method are homogeneous and reproducible. Thickness variation is generally low as calculated from the variation of 384 measurements. In the scaled demonstration, 90 % of corrosion is prevented during 5 days, compared to the control group. Complete suppression of degradation may be achieved with better control of operation parameters. It is not clear which role temperature fluctuations in the storage, pressure cycles, and handling during filling of the encapsulation and installation of the units played the major role in the final performance. The method presented in the next chapter will possibly enable the monitor the health of storage units during operation.

Compared to dip-coating, the injection method has the additional benefit of eliminating the need for large linear motion actuation, which allowed scaled up production of 10 encapsulations of 74 cm length cylinders in our own laboratory. These application sized samples were then filled with a custom PCM by an external company and tested under realistic conditions in a pilot AA-CAES plant.[18],[19] In these cases only the inside surface of the tubular encapsulation is exposed to the PCM, while the outside serves as heat exchange surface with the heat transfer fluid. The necessary precursor volume corresponds to the internal volume of the hollow cylinder. Actual consumption corresponds to the volume of the deposited film plus transfer losses. Most of the precursor is recovered in the process. In this study precursors were

generally re-used more than 20 times. With this efficient and scalable coating method a number of coatings were produced and tested for thermo-mechanical stability, and chemical compatibility with encapsulation and PCM.

Chapter 4:
Calorimetric cycling

4.1. First order transition modelling

Metallic PCMs possess favorable properties for LH-TES, which has been pointed out many times,[22],[23],[25],[50] and their superior conductivity and large capacity would make them preferable to salts, if it wasn't for the corrosiveness of liquid metals towards most applicable container materials.[25],[112] Many experimental and design studies have confirmed their performance in experimental storage applications,[18],[48],[52],[112]–[114] but reliable data on mitigation strategies for the specific liquid metal corrosion problem is scarce.

4.1.1. The Stefan problem

Knowledge of heat transfer characteristics in the PCM is critical for the design of performant LH-TES systems. The movement of the solid-liquid interface during phase transition is a determining aspect of such a system, and it's analytical treatment has been referred to as the Stefan problem.[115]–[118] The classical description assumes standard diffusion within each phase.

$$(\partial_t - \kappa_\nu \Delta_\mathrm{L}) T_\nu = 0, \text{for } \nu = \mathrm{w}, \mathrm{i} \qquad \text{Eq.(4.1)}$$

In Eq.(4.1), $\kappa = k/\rho c_\mathrm{p}$ is the thermal diffusivity, with ρ the mass density, ∂_t is the partial derivative in time, Δ_L is the Laplace operator. The phase at a given point (x, t) is either the liquid or the solid phase. They are designated w and i, for the canonical

model case of water and ice, respectively.§ Close contact of the two phases and conservation of energy at the moving boundary (Γ) gives the Stefan condition, Eq.(4.2).[116]

Eq.(4.2)
$$\left.\begin{array}{c} T_{\mathrm{w}} = T_{\mathrm{i}} = T_{\mathrm{m}} \\ \left(c_{\mathrm{p}}\kappa\ \partial_x T\right)_{\mathrm{i}} - \left(c_{\mathrm{p}}\kappa\ \partial_x T\right)_{\mathrm{w}} = h_{\mathrm{f}}\,\partial_t x_{\Gamma} \end{array}\right\} \text{for } x = x_{\Gamma}$$

the location of Γ. Initial Condition (I.C.) as in Eq.(4.3) and Boundary Condition (B.C.) as in Eq.(4.4) describe one-dimensional (1-d) domain of ice, initially isothermal at T close to T_{m}. At t_0=0 a zero-dimensional (0-d) constant temperature device at x_0=0 is turned to $\Delta T > 0$.

Eq.(4.3)
$$T_0 = T(x, t_0) = 0$$

Eq.(4.4)
$$T_{\mathrm{b}} = T(x_0, t) = \Delta T$$

The 1-d Stefan problem defined by Eq.(4.2) has been solved analytically. In the Neumann[119] solution, $x_{\Gamma}(t)$ takes the form of Eq.(4.5).

Eq.(4.5)
$$x_{\Gamma}(t) = 2\lambda_{\mathrm{N}}\sqrt{\kappa_{\mathrm{w}} t}$$

is obtained by solving Eq.(4.6).

4

Eq.(4.6)
$$\frac{\exp\left(-\lambda_{\mathrm{N}}^2\right)}{\operatorname{erf}\lambda_{\mathrm{N}}} - \frac{k_{\mathrm{w}}}{k_{\mathrm{i}}}\frac{\sqrt{\kappa_{\mathrm{i}}}\,(T_0 - T_{\mathrm{m}})\exp\left(-\kappa_{\mathrm{w}}\lambda_{\mathrm{N}}^2/\kappa_{\mathrm{i}}\right)}{\sqrt{\kappa_{\mathrm{w}}}\,(T_{\mathrm{m}} - T_{\mathrm{b}})\ \operatorname{erfc}\left(\lambda_{\mathrm{N}}\sqrt{\kappa_{\mathrm{w}}/\kappa_{\mathrm{i}}}\right)} = \frac{\lambda_{\mathrm{N}}\sqrt{\pi}\,h_{\mathrm{f}}}{c_{\mathrm{p,i}}(T_{\mathrm{m}} - T_{\mathrm{b}})}$$

Eq.(4.7) defines the Stephan number (St_{ν}), which is the ratio of sensible stored heat and h_{f}, when T_{m} is the reference temperature.

Eq.(4.7)
$$\mathrm{St}_{\nu} = \frac{c_{\mathrm{p},\nu}|T_{\nu} - T_{\mathrm{m}}|}{h_{\mathrm{f}}}$$

is the specific heat capacity of a phase ν at constant pressure, and T_{ν} is its temperature. A similar effort brings about the analytical solution to the radial Stefan problem. The Paterson solution[120] considers a three-dimensional (3-d) domain where a constant line heat source ($\dot{Q}_{\mathbb{O}}$) passes through the origin. The location of the

§ The subscripts (s) and (l) are reserved for solidus and liquidus.

moving boundary (r_Γ) is symmetric around the location of $\dot{Q}_{\mathbb{O}}$, assuming homogeneity of the medium. r_Γ is given in Eq.(4.8).

$$r_\Gamma(t) = 2\lambda_P\sqrt{\kappa_{(i)}t} \qquad \text{Eq.(4.8)}$$

Here, λ_P is a constant determined by Eq.(4.9).

$$\frac{-\dot{Q}_{\mathbb{O}}}{4\pi \exp\lambda_P^2} + \frac{k_{(w)}(T_0 - T_m)}{\exp\left(\kappa_{(i)}\lambda_P^2/\kappa_{(w)}\right)}\mathrm{Ei}\left(\kappa_{(i)}\lambda_P^2/\kappa_{(w)}\right) = \kappa_{(i)}\lambda_P^2\rho h_f \qquad \text{Eq.(4.9)}$$

Ei is the exponential integral function, Eq.(4.10).

$$\mathrm{Ei}(x) = \int_{-x}^{+\infty}\frac{e^{-t}}{t}\mathrm{d}t \qquad \text{Eq.(4.10)}$$

4.1.2. The enthalpy method

The enthalpy method has been adapted as numerical solution where I.C. are not isothermal or B.C. are not constant, i.e. where analytic approximations are difficult to obtain.[118] The explicit finite differences approximation for variable thermal properties follows Eq.(4.11). [117]

$$h_i^{j+1} = h_i^j + \rho^{-1}\frac{\delta t}{\delta x^2}\left\{k_{i-1}\left(T_{i-1}^j - T_i^j\right) - k_{i+1}\left(T_i^j - T_{i+1}^j\right)\right\} \qquad \text{Eq.(4.11)}$$

Where h_i^j is the enthalpy, at the location $x_i{=}i\cdot\delta x$ and time $t_j{=}j\cdot\delta t$, with δx being the discretizition length in space and δt the timestep. Critical for the stability of the solution is the criterion in Eq.(4.12).

$$\left(\frac{\rho c_p}{2k}\right)^{-1}\left(\frac{\delta t}{\delta x^2}\right) < 1 \qquad \text{Eq.(4.12)}$$

Every iteration of Eq.(4.11) is followed by updating the discretized temperature (T_i^j), according to the initially defined reference curve ($h(T)$) given in Eq.(4.13).

$$h(T) = \begin{cases} Tc_{p,s} & , \quad T - T_{(s)} < 0 \\ h_{(s)} + \left(T - T_{(s)}\right)\dfrac{h_f}{2\varepsilon} & , \quad T_{(s)} < T < T_{(l)} \\ h_{(l)} + \left(T - T_{(l)}\right)c_{p,(l)} & , \quad 0 < T - T_{(l)} \end{cases} \qquad \text{Eq.(4.13)}$$

Where $c_{p,s}$ and $c_{p,l}$ are the solid and liquid heat capacity, respectively. $h_{(s)}$ is the enthalpy at the solidus temperature ($T_{(s)}$) and $h_{(l)}$ is the enthalpy at liquidus

temperature ($T_{(l)}$). $h_{(s)}$ is equal to the product $T_{(s)}c_{\mathrm{p},s}$, and $h_{(l)}$ is equal to $h_{(s)} + h_{\mathrm{f}}$. The temperature interval of the phase transition is designated 2ε, so that $T_{\mathrm{m}} \pm \varepsilon$ is equal to $T_{(l)}$ and $T_{(s)}$, respectively.

Figure 4.1 shows that not only the sign but also the absolute value of the velocity of the phase boundary is depending on the direction of the heat transfer, i.e. the melting process is slower than the freezing process, for similar boundary conditions and the same material properties. This is due to the sequence of the two phases with respect to the system boundary, and the lower thermal conductivity of the liquid. Table 4.1 lists the properties used to compare the iterative result with the Neumann solution. Agreement is excellent, with the iterative solution, Eq.(4.11), adhering closely to the power law described in Eq.(4.8), characterized by the quality of fit parameter (R^2) of 1.000 for both melting and solidification.

Table 4.1 Material properties and discretization parameters required for calculating the time dependent location of the solid-liquid boundary for Al-12%Si.

$c_{\mathrm{p},s/l}$[52]	T_{m}*	h_{f}*	$k_{s/l}$[23]	ρ[52]	ε**
[Jg^{-1}K^{-1}]	[°C]	[Jg^{-1}]	[Wm^{-1}K^{-1}]	[gcm^{-3}]	[K]
1/1.5	574	460	180/70	2.25	2

*Measured in this work. **Arbitrary choice.

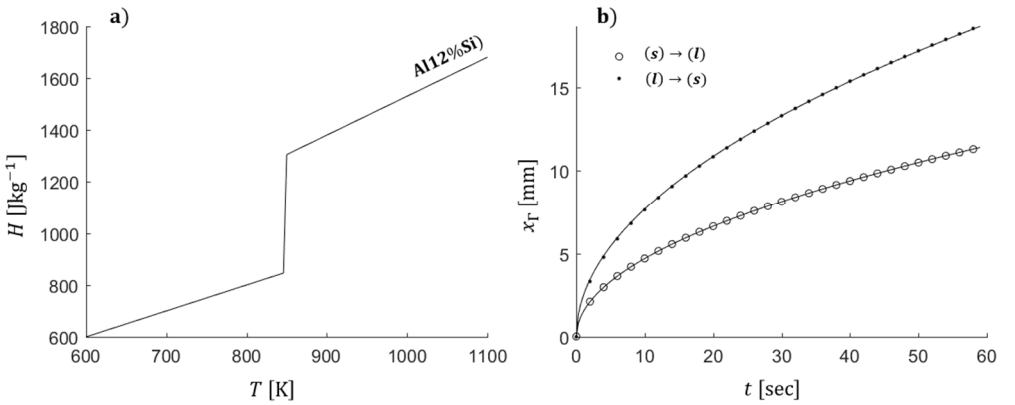

Figure 4.1 **a)** Linearized enthalpy curve for Al-12%Si according to Eq.(4.13) and using the material properties from Table 1. **b)** Comparison of phase boundary movement during melting (circles) and solidification (dots) from iterative calculation, showing excellent agreement with the Neumann solution (solid line).

4.1.3. Temperature history analysis

Thermo-physical properties that are fundamental to the application of LH-TES, i.e. the thermal conductivity, heat of fusion, heat capacity and melting temperature or transition range have been measured by DSC. Some authors have been looking for an alternative which is more suitable to the scale and complexity of encapsulating a PCM.[34]–[37],[122] Many authors have stated the drawbacks of the conventional DSC method, with regard to sample size, nucleation behavior, and interactions with the environment. In fact, the interaction of PCM and encapsulation becomes a critical factor for the performance of a given pair. Surfaces act as nucleating site for liquid media that exhibit under-cooling, effectively changing the physical behavior. Heat storage performance may be distorted in the inert environment of a ceramic DSC crucible. Other considerations go towards assessing corrosion interactions, as we have seen in Chapter 3. Several studies have been devising measurement schemes for the relevant LH-TES properties, mentioned above, which include the encapsulation, larger volumes, etc. probably best known in the literature is the so-called *T*-history method.[35] This method assumes Newtonian cooling, i.e. temperature variations in the body to be cooled are small compared to the temperature jump at the interface, which is asserted by considering the Biot number in the form of Eq.(4.14).[35],[123]

$$\mathrm{Bi}_2 = \frac{r_\mathrm{b} u_2}{2k_\mathrm{ep}} \qquad \text{Eq.(4.14)}$$

Bi_b is the Biot number for a cylinder of radius r_b, referring to outside boundary where heat exchange with the surrounding medium ($\dot{Q}_\mathrm{b}$) is proportional to the area specific heat transfer coefficient (u_2) and to the temperature gradient (g_2). k_ep is the conductivity of the cylinder, which in our case is the effective conductivity of the encapsulated PCM. The conductivity of the steel encapsulation should reasonably dominate the effective property for our sample and we see that Bi_2 is $\approx 5 \cdot 10^{-5}\, u_2$.** Values of Bi_2 close to 0.3 have been considered sufficiently low to calculate enthalpy curves and study the under-cooling behavior of various salts by immersion in

** Here 10 $\mathrm{WK^{-1}m^{-1}}$ was used as conservative assumption, considering also a transfer resistance to the encapsulated material. Al PCM conductivity is generally an order of magnitude higher.

water.[123] $\mathrm{Bi}_2 < 0.1$ may be preferable, for the surface to be heat transfer limiting.[35],[37] Our experimental approach should therefore have more than an order of magnitude of advantage regarding the approximations made by the *T*-history approach (Eq. 4.15).

Eq.(4.15)
$$h_\mathrm{f} m_\mathrm{p} = -u_\mathrm{b}\, A \int_{\nu=(s)}^{(l)} \left(T_\mathrm{p} - T_\infty\right) \delta t$$

Experimental approaches for low temperature PCM have been carried out using liquid cooling baths to control the surrounding temperature T_∞.[35]–[37] For high-temperature PCM, direct contact with liquid cooling fluid results in significant safety hazards. Our approach relies on ambient air and radiation and an even proximity of the sample chamber wall, where the temperature is controlled via embedded heating mantels. Plastic encapsulations of thin walled metal sheets are often used for packaging paraffins or salt hydrates. In contrast, high-temperature, metal-PCM systems make it necessary to consider the heat capacity of the encapsulation, due to the significant density of the used materials. Eq.(4.15) can be modified accordingly. The partial gradient (g_1), defined as $\left(T_\mathrm{b} - T_\mathrm{p}\right)$, is dependent on k_ep which may change in the presence of intermetallic layer growth. The corresponding partial transfer coefficient (u_1) is an effective lumped parameter characterizing the encapsulated PCM system. Eq.(4.16) uses the second partial boundary gradient (g_2), defined as $(T_\infty - T_\mathrm{b})$ to obtain the sample independent, device transfer coefficient (u_2). We use the convention to include the spatial dimension of the gradient in u_1/u_2. This approach is convenient and allows for calibrated measurements, as long as the position of the temperature measurements is fixed, and the encapsulation geometry isn't altered.

Eq.(4.16)
$$\frac{2\varepsilon\left(< c_{\mathrm{p},sl} > m_\mathrm{p} + c_{\mathrm{p,E}} m_\mathrm{E}\right) + h_\mathrm{f} m_\mathrm{p}}{\mathrm{Gi}_2} = -u_2 A$$

The gradient integral $\mathrm{Gi}_2 = \int \left(T_\infty - T_\mathrm{b}\right) \delta t$ has the units of Ksec. The temperature intensity differential dGi_2 is directly related to the enthalpy differential d*H,* provided neither geometry nor heat transfer properties at the air gap change. The surface at the boundary A is equal to $2\pi L_z\, r_\mathrm{b}$. $u_2 A$ becomes the proportionality constant and machine calibration factor in units of $\mathrm{JK^{-1}sec^{-1}}$. Knowledge of $c_{\mathrm{p,E}} m_\mathrm{E}$ is not required, when a baseline measurement with the empty encapsulation is acquired before

measurement of the calibration standard. The exact value of $< c_{\mathrm{p},sl} >$ can be evaluated as the weighted average of $c_{\mathrm{p},l}$ and $c_{\mathrm{p},s}$: $\int \left(\phi_l c_{\mathrm{p},l} + \phi_s c_{\mathrm{p},s}\right) \mathrm{d}T$, but is in practice close to the mean of $c_{\mathrm{p},l}$ and $c_{\mathrm{p},s}$. $u_2 A$ is obtained using Eq.(4.16) when a suitable calibration standard with well know $h_{\mathrm{f}} m_{\mathrm{p}}$ is used. Eq.(4.17) allows to calculate the exact value of $\dot{Q}_{\mathrm{b}}$ based on knowledge of $u_2 A$, if g_2 is constant.

$$\dot{Q}_{\mathrm{b}} = g_2 u_2 A \qquad \text{Eq.(4.17)}$$

For narrow ε, small heating rate ($\dot{T}_\infty$), and large h_{f}, the gradients g_1 and g_2 can be regarded as constant in time. Then, u_1 can be estimated with tentative precision using the steady state relation given by Eq.(4.18).

$$g_1 u_1 = g_2 u_2 \qquad \text{Eq.(4.18)}$$

The aim of the in the following described experiment is to investigate the heat transfer performance of cylindrically encapsulated Al PCMs, and to test Predictions made on the basis of the model presented in Chapter 2. Ultimately the goal is to learn under what conditions this and similar systems can be operated at high and sufficiently stabile performance.

4.2. Experimental

A calorimetric experiment with in-situ monitoring of the stability of thermo-physical characteristics of encapsulated aluminum alloys was purpose-built from refractory calcium silicate porous ceramic material (Duratec-1000, PROMAT). Samples were prepared from stainless steel tubes. The ends were sealed with Duratec, and ceramic high-temperature glue. The top lid had openings prepared for the insertion of an alumina protected thermocouple (Figure 4.2). Coatings were applied in some cases, using the injection method described in Chapter 3. The heated set-up, as well as the samples had a cylindrical topology with circumferential heating (Figure 4.3 and Figure 4.5). This ensured a uniform radial heat flux, which facilitated the analytical treatment. A stack of three individually controlled heating mantels maintained a uniform temperature along the axis of rotation (z-axis). Chromel-R (80%Ni-20%Cr) wire of 0.16 mm^2 cross-section was integrated into the wall of the calcium silicate sample chamber and served as electrical resistive heating source. Melt-solidification cycles were imposed on PCM and encapsulation according to

defined temperature sequences. A digital terminal (LabVIEW 2017a, National instruments) provided a user interface for programming experimental conditions. Thermocouple readings were recorded in positions corresponding to T_p, T_b and T_∞. Heating power was adjusted by pulse density modulation of a 48VDC power supply. A pulse frequency of 1 kHz making use of fast switching semiconductor relays (CMX60D10, Crydom) assured precise temperature control. Homeostasis was maintained to a root mean square (rms) smoothness of the temperature feedback of below 0.1 K, and bias was not measurable.

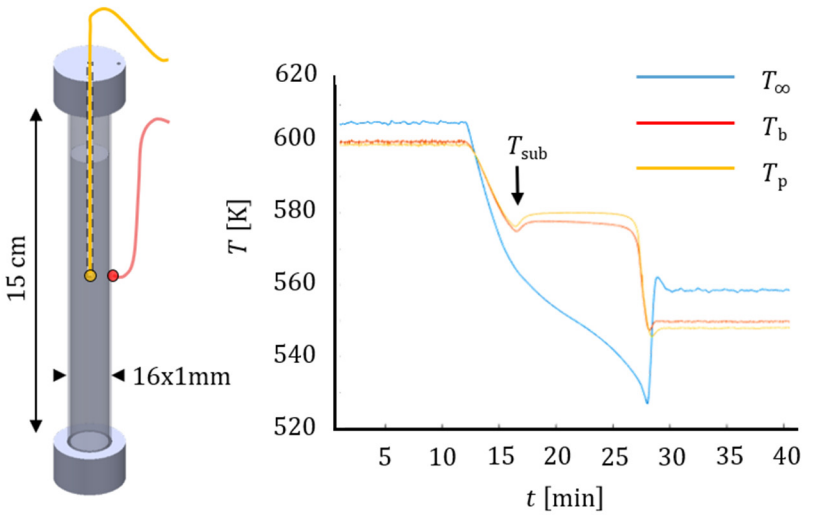

Figure 4.2 Fixed temperature sensors in and on the surface of cylindrically encapsulated Al storage medium allowing for in-situ observation of heat transfer gradient, undercooling, rebounds and stabilization of discharge heat temperature. Sample with aspect ratio close to 1:10 (left), and *T*-history plot (right) allowing for efficient quantification of heat transfer.

Temperature boundary conditions were piecewise linear, with isothermal holds of up to 5 h. Linear heating rates were limited by the capabilities of the setup, i.e. the maximum recorded rates were within [-12 K/min…+42 K/min]. The boundary condition seen in Figure 4.2 was passively invoked. The cooling rate was convection limited, and precise rate control was achieved when rates were chosen within [-10 K/min…+25 K/min]. Heat transfer rate and storage capacity were calculated according to Eq.(4.16). Calibration of $u_2 A \coloneqq U_b$ was initially achieved using 13 g of Al (99.99%, <9.5 mm pellets, ABCR) and the referred value of h_f=398 J/g.[98] The encapsulation consisting of a 46.5 mm long, 2x20 mm hollow 316 L cylinder with Duratec® seals for the shown calibration. Baseline measurements were recorded

during 3-5 cycles to accurately subtract the sensible heat capacity of the encapsulating material from the PCM signal. The encapsulation length was varied from 46.5 mm, to 72 mm, 92 mm, and 155 mm. Each geometry received either a dedicated calibration measurement or calibration was achieve using the first solidification event and DSC measurements of the pristine PCM as internal standard. Figure 4.4 shows the enthalpy curve of the calibration standard for the 46.5 mm case. The use of u_2 as calibration factor was tested by comparing measurements of h_f for Al-12%Si and Al-26%Cu-5%Si with literature data. Transition temperature thresholding was facilitated by zero phase filtering using a low-pass frequency filter design with a passband frequency of 1/90 sec.

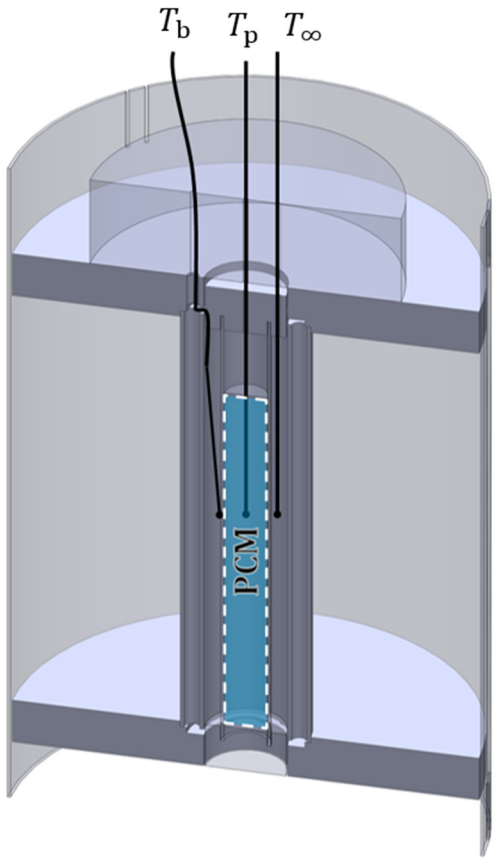

Figure 4.3 Experimental set-up for applying extended load cycles and monitoring of heat storage performance. Vertical section reveals the central location of the phase change material and placement of temperature sensors. Temperatures were measured at the mid-height plane at the center, immersed in the aluminum alloy (T_p), on the surface of the steel encapsulation (T_b), and close to the porous ceramic wall (T_∞) of the temperature-controlled calorimeter.

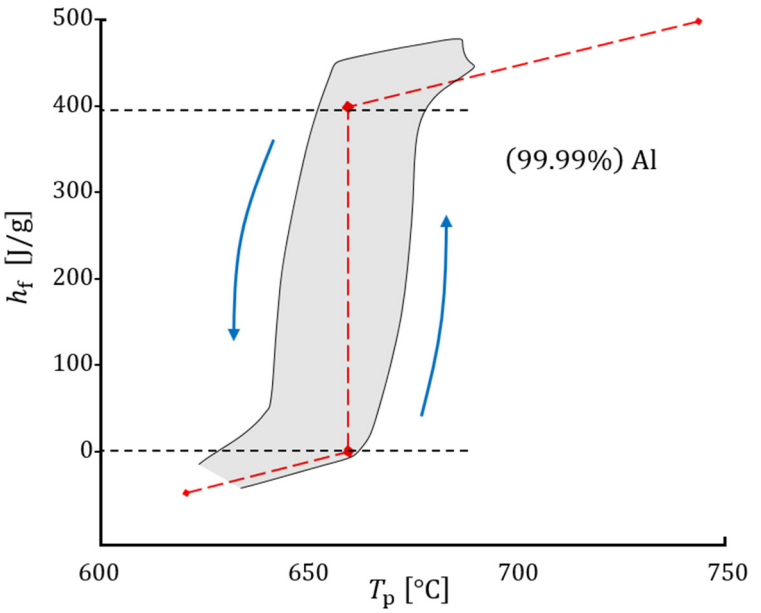

Figure 4.4 The enthalpy curve of pure Al (blue area), obtained by integration of g_2 after calibration using a correlation from [22] (dashed line). The measured slope before the respective phase change events (up/down arrow) compares to $c_{p,s}$, and $c_{p,l}$.

4.3. Results of cyclic testing

Figure 4.6 shows two enthalpy curves recorded with the in-house developed calorimetry test bench. The measured transformation temperature and magnitude of the heat of fusion are in good agreement with literature data on measurements carried out on commercial DSC hardware. Table 4.2 compares the heat of fusion and transformation temperatures for commercial Al-12%Si, synthesized Al-25%Cu-5%Si PCM, and the calibration element. The generally good agreement with reported values and additional methods should underline the accurate quantification capabilities of the method. The obtained calibration factor of $U_b = 0.5822$ $JK^{-1}sec^{-1}$ was valid as long as the encapsulation length and diameter were kept constant and no heating coils had to be replaced.

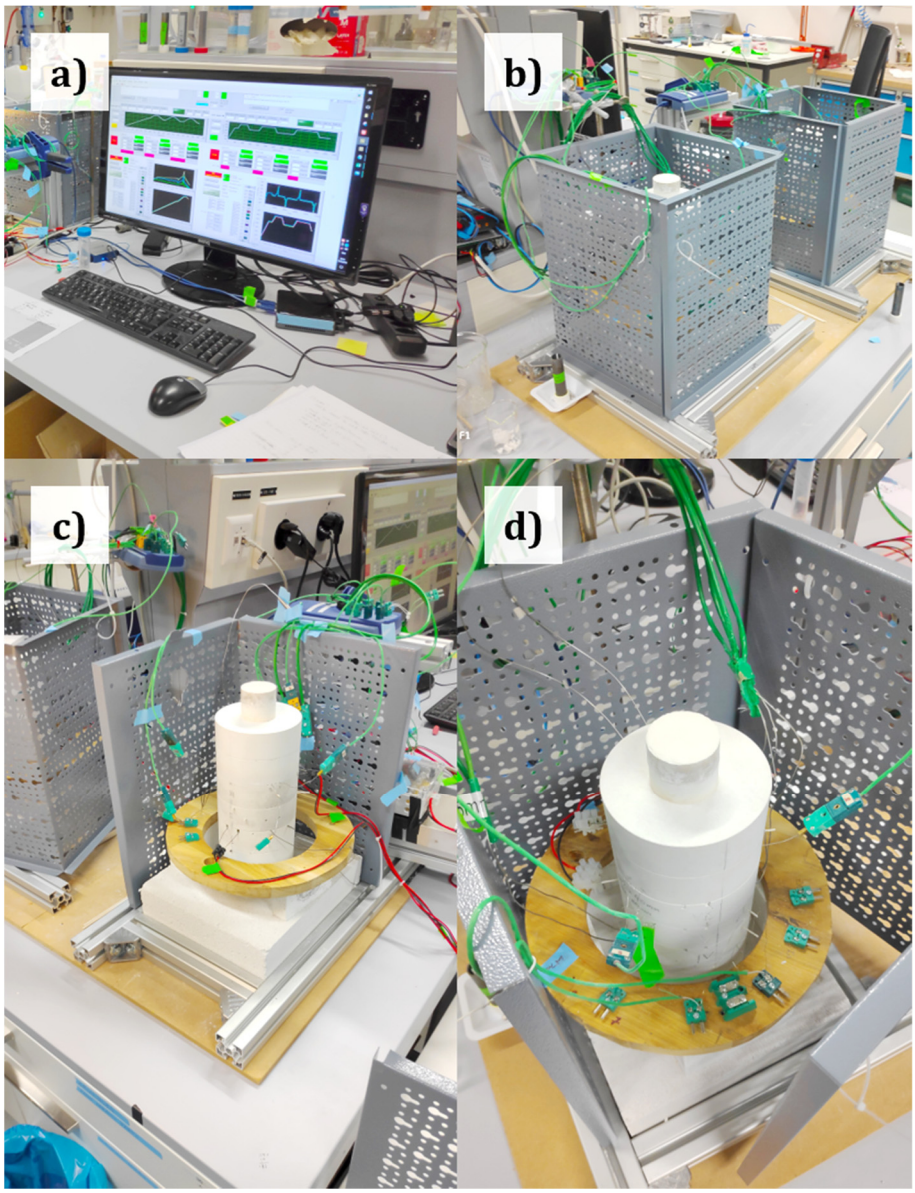

Figure 4.5

Calorimetry test bench for prolongued cycle endurance and performance testing of high-temperature metal PCM units. **a)** LabVIEW control terminal. **b)** Cycling furnace no.2 and no.3 behind convection shielding. **c)** Furnace no.2 with removed shield revewls individually *T*-controlled segments called heating stages. **d)** Conector board with adaptable sensor setup.

4.3.1. Reduced under-cooling

Our method for the in-situ determination gave largely similar results for h_f, c_p, and the onset of melting $T_{(s)}$ as DSC confirmation measurements by us, and values reported in the literature. However, we found significantly narrower phase transition boundaries with regard to the onset of solidification $T_{(l)}$, compared to conventional DSC analysis. Under-cooling assessed by the local minima and maxima in the PCM temperature trace never exceeded 3 K for our encapsulated samples of Al-12%Si, as can be seen in Figure 4.2. In the enthalpy curves in Figure 4.6a it is again met, when following the described path counterclockwise, after passing the turning point of the highest temperature. The largest hysteresis in this series of measurements was produced by the Al 99.99% calibration material, and reaches a width of approximately 25 K (see Figure 4.4, previous section). Typical separation of melting and solidification peak in DSC was often larger than 60 K with the solidification onset 20 K below the reported melting temperature of the substance. In contrast, the in-situ method gave a relative cross-over, with solidification onset as high as 582 °C (Figure 4.6b). This may be due to the buried thermocouple within the PCM being used as reference. Additionally, the almost complete absence of under-cooling may be connected to the increased defect density on the encapsulation surfaces, promoting heterogeneous nucleation. Generally, DSC manufacturers recommend high-density, and high-purity α-alumina for the characterization of metals, to exclude chemical reactions and guarantee longevity of the equipment. Therefore, quality DSC crucibles minimize interaction with the sampling material. Appearance of the solidification signal 25 K below the reported T_m of Al could be explained by the lack of interaction with the DSC crucible and consequently retarded nucleation. Confirmation could be in principle obtained by neutron diffraction, where the formation of crystallization nuclei can be detected.[76]

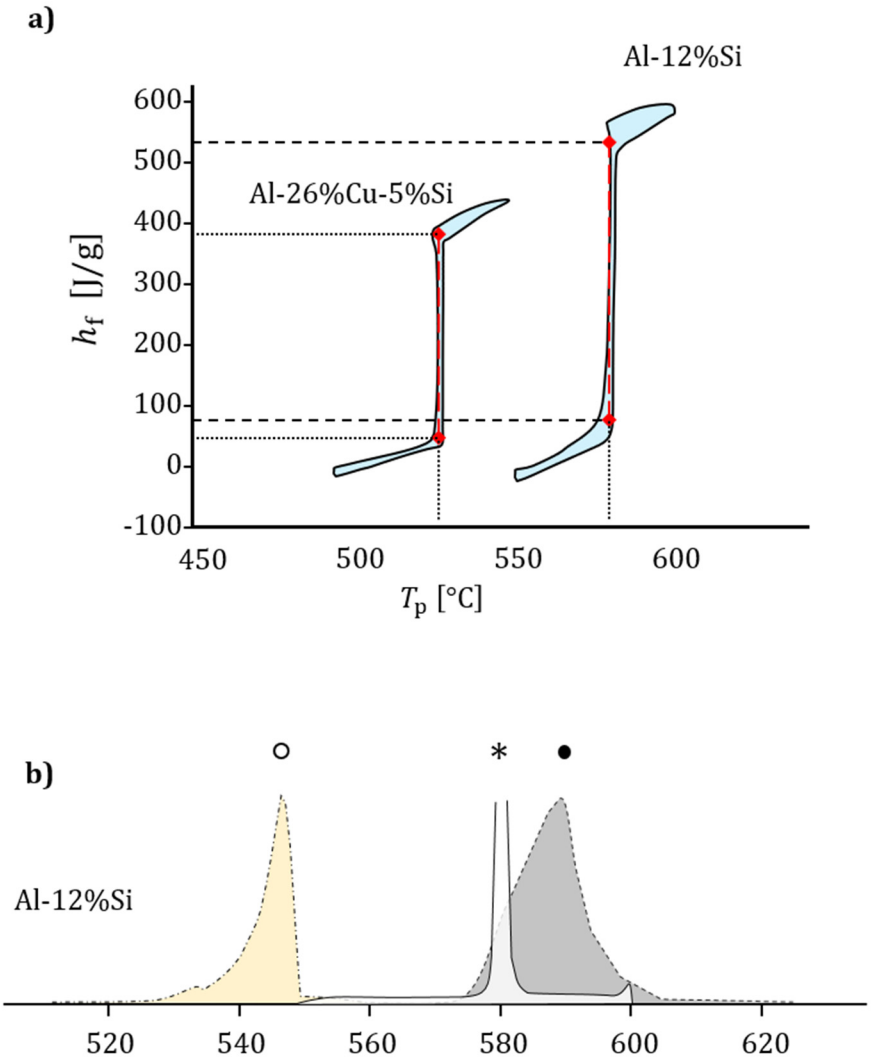

a) Quantitative enthalpy curve recordings of Al-26%Cu-5%Si (left) and Al-12%Si (right). **b)** DSC traces for melting (dot) and solidification (circle) of Al-12%Si compared to the heat capacity curve derived from in-situ calorimetric cycling (asterisks). Curves are scaled to the same height to emphasis peak width.

Figure 4.6

Table 4.2. Summary of thermo-physical properties, quantified in the calibrated cyclic load test bench*, measured in this work by DSC, and reported in the literature.

Storage material	U_b^* $JK^{-1}sec^{-1}$	h_f* Jg^{-1}	h_f^{DSC} Jg^{-1}	$h_f^{lit.}$ Jg^{-1}
99.99% Al	0.5822	Cal.	404	397.7[98]
Al-12%Si		470	462	466[48]
Al-26%Cu-5%Si		330	373	364[22]
		T_m* [°C]	T_f^{DSC} [°C]	$T_m^{lit.}$ [°C]
99.99% Al		655	663	660.3[98]
Al-12%Si		577	569	579[23]
Al-26%Cu-5%Si		524.4	519	525[11]

4.3.2. Heat transfer evolution

Figure 4.7 shows the heat transfer of an Al-12%Si encapsulation during 114 full storage cycles. Performance reduction was rapid during the first 10-20 cycles for this uncoated sample under relatively demanding conditions (cycle type C_1, Figure 4.10, following section). The trace of $\dot{Q}_b$ (Figure 4.7a) is shown over $(t - t_{i,0})$, i.e. with respect to the begin of the *i*-th storage displacement ($t_{i,0}$). The first two displacements lasted 120 min, and all subsequent displacements lasted 60 minutes. During these periods $\dot{T}_\infty$ was kept constant, equal to 1.25 $Kmin^{-1}$ for the first two events, and 2.5 $Kmin^{-1}$ for the 226 subsequent events. The shape of the power-time curve resembled those obtained in typical DSC measurements. $\dot{Q}_b$ scaled proportionally with $1/\dot{T}_\infty$, which is seen in the comparison of the first and subsequent cycles. Sensible heat capacity contributions produced a horizontal plateau. Melting and solidification were characterized by relatively linear acceleration of heat transfer rate up to the peak, and a sharp decay after reaching the maximum. We adapted the convention that positive values represent stored energy, i.e. the melting events are shown above the zero-Watt line, and the solidification events below. Time runs left to right in both cases. Evaluation of the extrema of $\dot{Q}_b$, and the average ($<\dot{Q}_b>$) are shown in Figure 4.7b. It can be expected that $<\dot{Q}_b>$ is relatively less dominated by the latent heat capacity, compared to $\max(\dot{Q}_b)$ and $\min(\dot{Q}_b)$. Relative reductions for all four

values were calculated to be within 43% and 57%. Significant differences in degradation of melting and solidification behavior were not confirmed.

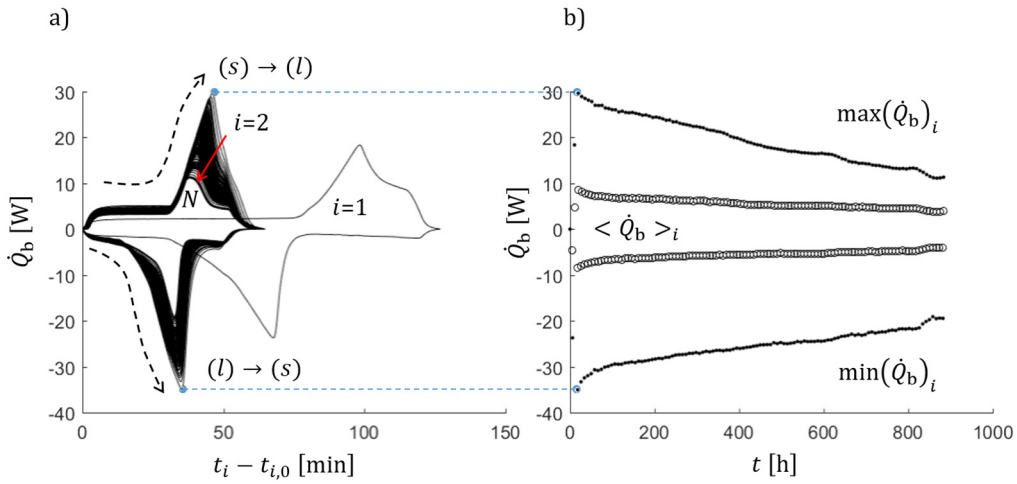

Heat transfer rate during $i = 1 \ldots 114$ storage cycles with Al-12%Si storage medium. Storage ($(s) \rightarrow (l)$) and release ($(l) \rightarrow (s)$) correspond to + and - sign, respectively. **a)** Area under the trace is reduced during 900 h of testing. The first cycle (i=1) was recorded at half the heating rate. Successive cycles (i=2 … 114) are done at 2.5 K/min. **b)** Peak and average power per transition.

Figure 4.7

Figure 4.8 shows how different solid and liquid conductivity impact the latent heat uptake and release kinetics. Different magnitude of the peak charging power ($P^{+}_{\max}$) during melting and the peak discharge power ($P^{-}_{\max}$) during solidification was in agreement with predictions from numerical simulation of the Stefan problem (Section 4.1.2). $P^{-}_{\max}$ was initially 20% and later up to 80% greater than $P^{+}_{\max}$, while the average rates of discharge/charge were equal close to equal (Figure 4.8a). Figure 4.8b shows increasing conductive heat transfer resistance within the encapsulated PCM. The trend may be explained by the growing intermetallic layer, or changing effective conductivity in the bulk of the PCM. u_2/u_1 is generally lower when the PCM is in the solid state. The integrated enthalpy as function of temperature is shown in Figure 4.9a. The totally stored heat over the fixed temperature interval of 150 K indicated to decrease with increasing cycle count. The overall capacity per full storage displacement expressed as ΔH_i is diminished from close to 40 kJ to below 30 kJ in less then 10 cycles (Figure 4.9b). Later the decreaseing trend continues monotonically. Energy conservation demanded charging and discharging energies to be equal. A slight inaccuracy during t=[100…400] h is attributed to incompatibility of the integration scheme with under-cooling.

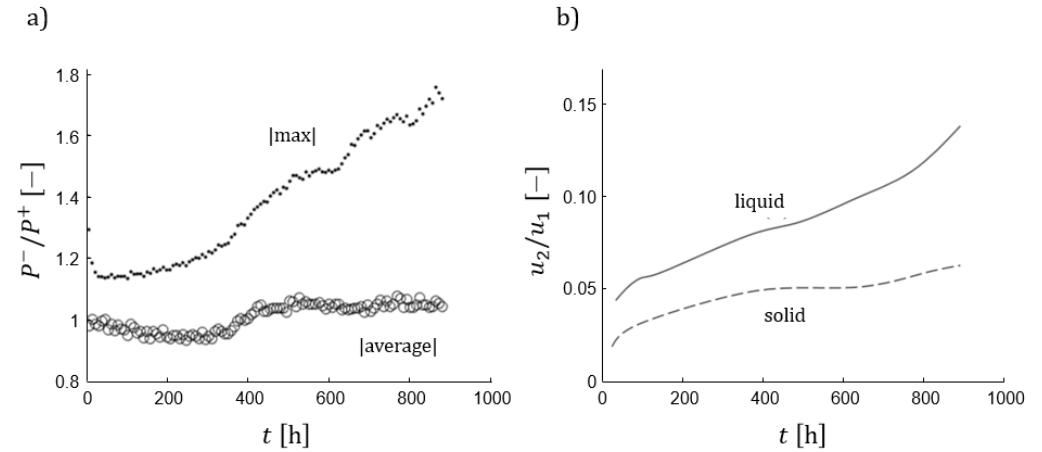

Figure 4.8 **a)** Ratio of peak heat transfer rate (dots) and average heat transfer rate (circles) comparing solidification to melting. Peak-values >1 reflect higher conductivity of Al-12%Si in the solid state compared to the liquid. The relative difference follows an increasing trend with cycling time. The average ratio stays relatively close to 1. **b)** relative conductive resistance of the solid (dashed line) is lower compared to the liquid state (solid line), with increasing trend for both.

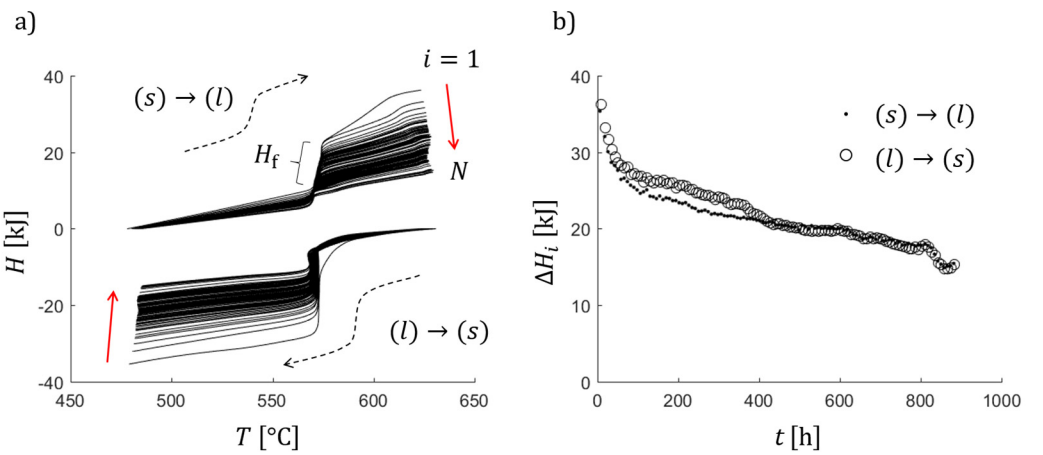

Figure 4.9 Cumulative enthalpy function of i=1 … 114 storage cycles with Al-12%Si storage medium. **a)** Enthalpy curves recorded between 475 and 625 °C, exhibiting 1st order discontinuity. In the case of the $(l) \rightarrow (s)$ transition under-cooling is visible. **b)** Storage capacity for a given ΔT_p reduced by approximately 50 % after 922 h of accelerated aging.

4.3.3. Effect of cycling conditions

Cycle definition was found to have profound impact on the performance evolution of tested encapsulations. Critical factors were anticipated to be linked to the frequency of phase transitions (f_{pc}) and boundary conditions such as $\tilde{T}_{\mathrm{b}}$ and ΔT_{b}. Figure 4.10a shows two principal types of cycles, i.e. C_1 emphasizes large temperature swings at high rate of change, and high-temperature holding periods. We express the ratio of high-temperature hold duration to repetition period as R_{h}. Then we can characterize C_1 as $\sim R_{\mathrm{h}}$=5/8, ΔT_{b}=75 K, and $\tilde{T}_{\mathrm{b}}$=575 °C. On the other hand, we see that C_2 with $\sim R_{\mathrm{h}}$=3/8, ΔT_{b}=25 K, and $\tilde{T}_{\mathrm{b}}$=575 °C, has the same median temperature and differs by its lower average temperature and less extensive swings.

Figure 4.10b compares 3 cases based on C_1, as well as two variations of C_2. We found a pronounced capacity stabilization in favor of a sample which was coated in BN as compared to the base C_1 condition. The stabilization appeared effective throughout 500 h. Later, the effect of the coating appeared to vanish and the trace started approaching the reference sample asymptotically. The relatively sudden change in behavior could be explained by homogeneous thinning of the coating by dissolution. Microstructural investigation showed evidence supporting a pin-and-peal mechanism, where intact patches of coating appear to get peeled off by newly formed intermetallic phases (compare Figure 4.11). Both models could lead to a relatively discrete de-protection event, however in the case of homogeneous coating dissolution the lifetime should be more deterministic, while the pin-and-peal mechanism infers a strong stochastic component. A superposition of both mechanisms may also be envisioned.

The so far evaluated measures are determined by the size and aspect ratio of the test samples. They serve as model validation and basis to deepen mechanistic understanding. Figure 4.12 shows the evaluation of $T_{(l)}$ and u_1, for two sample with the same geometry and test conditions. Decreases in $T_{(l)}$ are consistent with increasing impurity content of which Fe was previously found to make up the largest portion. Evaluation of u_2 reflects the growth of an intermetallic layer of non-negligible thermal resistivity, and falls from initially 6 $\mathrm{kWK^{-1}m^{-2}}$ to below 1 $\mathrm{kWK^{-1}m^{-2}}$, after 900 h of testing, and more than 400 phase transitions. Intermetallic layer growth has been

found in previous studies to start at a high rate††, and decelerate quickly to proceed at a relatively slow monotonic rate.[38],[40],[124] The observed kinetics agree qualitative with the model prediction made for isothermal conditions. Predictions from section 2.2.3 for the r_0=8 mm when converted to an estimation of u_1 after 1 year gave a value between 100 $WK^{-1}m^{-2}$ and 500 $WK^{-1}m^{-2}$. Results from cyclic calorimetry gave a value close to 1000 $WK^{-1}m^{-2}$ after 900 h of cycling. Long term numerical predictions and calorimetric data from cyclic testing corroborate to confirm that the favorable properties of the investigated LH-TES components maintain low heat transfer resistance under relevant conditions. Scaling is expected to affect u_1, and $T_{(l)}$ indirectly, so that the obtained results can tentatively be used to design larger systems. $T_{(l)}$ for instance, may evolve similarly fast or even slower in a larger system, where saturation may take longer to reach.

Evidence for the existence of regenerating natural passivity can be found in the conditions termed C_1+break, where a single pause in the test sequence with intermediate cooling to room temperature and reuptake produced a complete stabilization of a previously fast degrading encapsulation (Figure 4.10b). C_2 cycles have been reproducibly confirmed to not initiate the interface reaction observed in C_1 cycles, over a period of 120-160 h. The relative increase in the two depicted C_2 cycles was explained by the first cycles not reaching complete melting, and subsequent improvement of u_1. Refinement of the dissolution modelling may clarify if there is a stabile dynamic equilibrium with a dissolving and regenerating passivation of oscillating thickness.

†† After an incubation period without any growth, of variable duration.

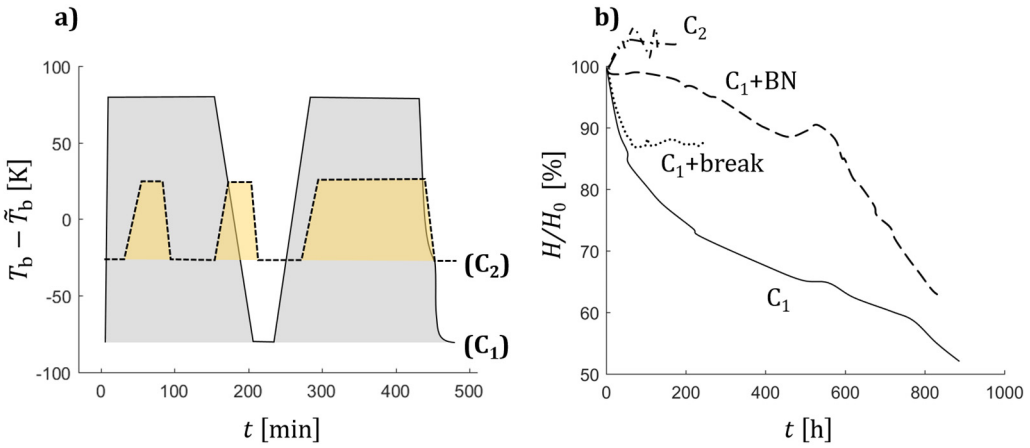

a) Variation of cycle definitions with 8 h periodicity: High intensity cycles where average temperature is above median with phase change frequency of f_{DC}=12 day^{-1}, and high to low T-ratio of R_{h}=5/8 (C_1). Balanced cycles definition with similar median temperature, and increased phase change frequency of f_{DC}=18 day^{-1}, and R_{h}=3/8 (C_2). **b)** Capacity traces of selected samples show stabilizing effect of BN coating and cycle definition. C_1+break indicates a single 24 h pause in the otherwise unchanged sequence.

Figure 4.10

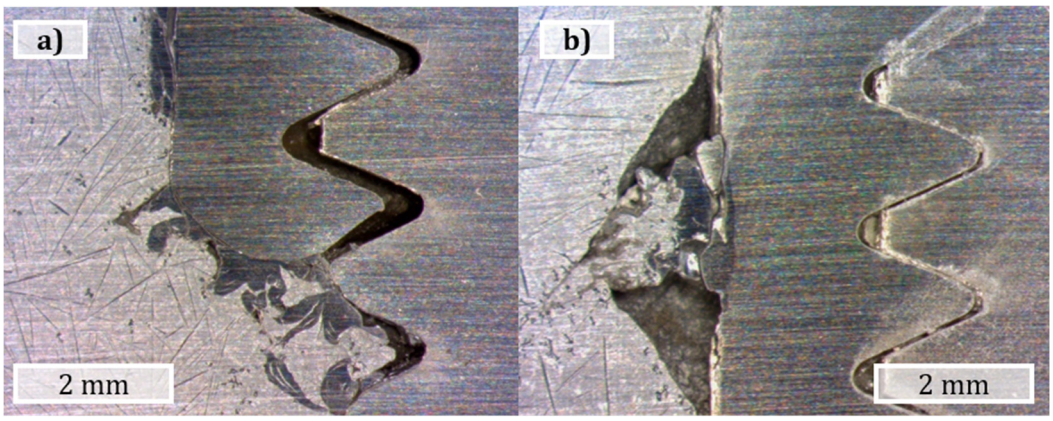

a) Initiation of intermetallic reaction begins close to the test encapsulations threaded cap. **b)** Aluminum penetrating the BN diffusion barrier causes deformation and delamination of the coating.

Figure 4.11

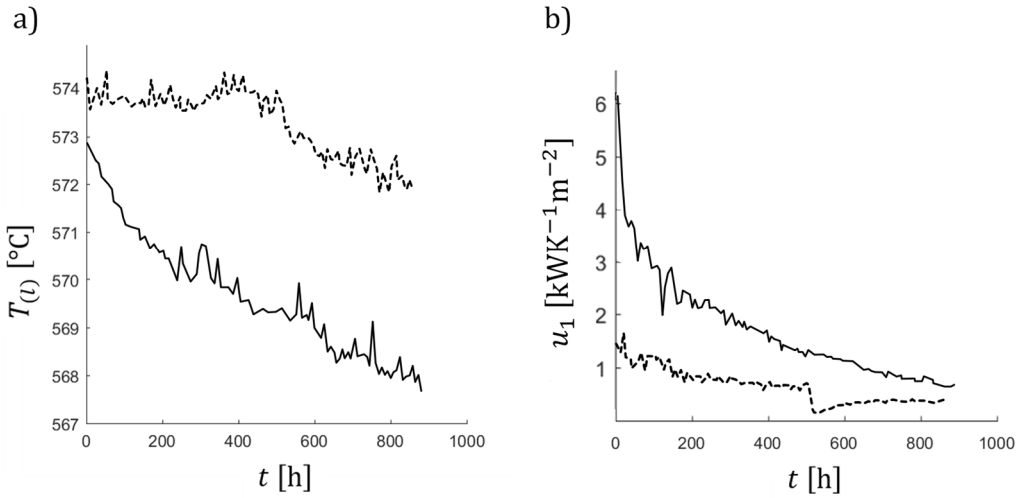

Figure 4.12 **a)** Liquidus transition temperature decreasing with prolonged cyclic testing for the case of Al-12%Si encapsulated in bare 316L steel (solid line) and coated with *h*-BN (dashed line). **b)** Heat transfer coefficient of the coated sample with step-down after 500 h, around the same time as $T_{(l)}$ starts to fall.

Chapter 5:
Discussion and outlook

5.1. Diffusion and solubility modelling

Diffusion/dissolution modelling with Arrhenius temperature dependence has helped to understand experimental observations and contributes to the development of advanced high-temperature LH-TES technology, by improving on the predictive power of current state of the art models. Our work extends the current knowledge and contributes to the discussion of intermetallic layer formation kinetics, i.e. there is an active discussion about why in the present and in related systems growth kinetics deviate from the self-limiting parabolic rate law. Our numeric calculations of the de-passivation mechanism have demonstrated a possible explanation with physical relevance for the initially observed acceleration. This feat is impossible in a purely self-limiting system. The introduction of a slowly dissolving passivation layer with low but finite permeability resolves this issue, and provides an acceleration mechanism for the diffusive fluxes involved in intermetallic layer formation. The calorimetric cycling method contributed with explicit quantitative capacity and heat transfer data to the validation of both out heat and mass transfer modelling. The hypothetic regeneration mechanism for naturally existing passivation layers, may be tested by further systematic variations of cycling conditions. A refined and validated model may have the potential to predict and extend the innate passivity domain of otherwise uncoated steel encapsulations, and beyond the current application may be of general interest for the understanding of wetting and corrosion phenomena.

5.2. Performance stabilization

Initial exploration found the main challenge to metal LH-TES to be posed by the corrosiveness of liquid aluminum alloys. Integration of experimental findings into numeric modelling has derived operation conditions which mitigate performance under active degradation. Operation temperature and encapsulation-PCM interface design in terms of surface to volume ratio consideration were fundamental to a conservative operation scenario. Primarily, this approach yields the estimate, that high volume to surface systems can expect manageable capacity aging, and encapsulation thinning, while still profiting from the excellent heat transfer properties provided by the Al PCM alloy family. Coatings from inert ceramics could be deposited by methods purposely developed, while scaled field tests have also revealed where the limitations of the diffusion barrier approach exist. The applied boron nitride coating prevented performance degradation efficiently during 500 h of testing under the harsh C_1 type conditions. 95 % of the initial capacity remained at the end of this period, while the control experiment shows a reduction of 50% in the same period. Combining the results from isothermal lab scale tests, pressurized cyclic field experiment, and calorimetric cycling endurance testing. BN has been seen consistently and under variable and prolonged testing to have a beneficial effect on storage capacity. Coating breaches occurred under dynamic conditions more often than under relatively hotter isothermal conditions, pointing towards sufficient chemical resistance towards dissolution attack. Application of BN diffusion barrier coatings for performance stabilization may therefore preferentially most suitable in combination with high $\tilde{T}_\mathrm{b}$, high R_h applications, which do not rely on excessively dynamic storage displacement action. Under such conditions the inertness of *h*-BN may significantly enhance LH-TES container lifetime and thereby contribute to economical operation. Aggravated localized attack after puncture has not been confirmed nor denied by the data. If future investigations find that such mechanisms get enhanced by larger surface to volume ratio, pre-saturation of the PCM with Fe, Ni, or Cr may mitigate their severity. Thick coatings present an additional resistance to heat transfer, but not to a significantly greater extent than the growth an intermetallic layer may produce. The bare encapsulation starts out with $u_1 \sim 6000$ $\mathrm{WK^{-1}m^{-2}}$, but loose the advantage quickly as layer growth is initially rapid. In both cases Bi would still be <1 after 800 h of cyclic operation.

5.3. Outlook

We have so far seen that although manageable, ceramic coatings add to the overall heat transfer resistance and may still not suffice under all conditions. Dense fully-ceramic encapsulations may deserve a second look, under conditions where a single layer shell of dense material may facilitate heat transfer compared to a tangible ceramic-metal laminate. Such an approach would reduce delicate ceramic metal interface design, which may balance the added cost of bulk technical ceramic raw material, compared to economic steel substrates. Recent advancements in our experimental approach may suggest that thin walled, self-supporting ceramic encapsulations can be fabricated to accommodate the internal pressure exerted by the PCM. Such encapsulations could be chemically lasting and potentially applied to the PCM in an efficient coat-on encapsulation process. Suitable materials may be obtained from gelled colloids with ultra-high *h*-Si_3N_4 particle loading directly deposited onto Al pellets to obtain mm-scale ceramic encapsulated PCMs of elliptical shape. Formulations of Si-(Na)-(Al)-O-N have been reported to be sluggish in crystallization behavior,[125],[126] which may enable the precursor encapsulation to accommodate the 8-15 % volume increase of the PCM during the annealing step, after which they can be crystallized and will only endure comparatively low thermomechanical force. The synthetic route via metal-oxide-polymers, in situ formed glassy functional intermediates, and finally obtaining refractory glass ceramic certainly is an exciting prospect, and diverse investigations spanning the fields of electronics and structural transparent glasses for device and building applications have been in progress.[125],[126] Promising materials synthesized in this work were intended for coating and sealing purposes of metal substrates. It can be regarded as synthesis from objective successes in regard the objectives (A) and (C), which contribute these new possibilities toward the next generation of mitigation strategies for liquid PCM encapsulation corrosion.

5

Bibliography

[1] International Energy Agency. *World Energy Outlook 2018*; World Energy Outlook; OECD, 2018. https://doi.org/10.1787/weo-2018-en.

[2] Grübler, A.; Jefferson, M.; Nakićenović, N. Global Energy Perspectives: A Summary of the Joint Study by the International Institute for Applied Systems Analysis and World Energy Council. *Technol. Forecast. Soc. Change* **1996**, *51* (3), 237–264. https://doi.org/10.1016/0040-1625(95)00251-0.

[3] Lee, R. The Outlook for Population Growth. *Science* **2011**, *333* (6042), 569–573. https://doi.org/10.1126/science.1208859.

[4] Chu, S.; Majumdar, A. Opportunities and Challenges for a Sustainable Energy Future. *Nature* **2012**, *488* (7411), 294–303. https://doi.org/10.1038/nature11475.

[5] Arce, P.; Medrano, M.; Gil, A.; Oró, E.; Cabeza, L. F. Overview of Thermal Energy Storage (TES) Potential Energy Savings and Climate Change Mitigation in Spain and Europe. *Appl. Energy* **2011**, *88* (8), 2764–2774. https://doi.org/10.1016/j.apenergy.2011.01.067.

[6] *Schweiz. Gesamtenergiestatistik 2017*; Statistic; Bundesamt für Energie, BFE: 3003 Bern, 2017.

[7] *ECOHEATCOOL, Work Package 1*; The european heat market; Final report; Euroheat & Power: 1150 Brussels, Belgium, 2006.

[8] Rea, J. E.; Oshman, C. J.; Olsen, M. L.; Hardin, C. L.; Glatzmaier, G. C.; Siegel, N. P.; Parilla, P. A.; Ginley, D. S.; Toberer, E. S. Performance Modeling and Techno-Economic Analysis of a Modular Concentrated Solar Power Tower with Latent Heat Storage. *Appl. Energy* **2018**, *217* (December 2017), 143–152. https://doi.org/10.1016/j.apenergy.2018.02.067.

[9] Zanganeh, G.; Commerford, M.; Haselbacher, A.; Pedretti, A.; Steinfeld, A. Stabilization of the Outflow Temperature of a Packed-Bed Thermal Energy Storage by Combining Rocks with Phase Change Materials. *Appl. Therm. Eng.* **2014**, *70* (1), 316–320. https://doi.org/10.1016/j.applthermaleng.2014.05.020.

[10] Jalalzadeh-Azar, A. A.; Steele, W. G.; Adebiyi, G. A. Performance Comparison of High-Temperature Packed Bed Operation with PCM and Sensible-Heat Pellets. *Int J Energy Res* **1997**, *21*, 14.

[11] Kenisarin, M. M. High-Temperature Phase Change Materials for Thermal Energy Storage. *Renew. Sustain. Energy Rev.* **2010**, *14* (3), 955–970. http://dx.doi.org/10.1016/j.rser.2009.11.011.

[12] Pielichowska, K.; Pielichowski, K. Phase Change Materials for Thermal Energy Storage. *Prog. Mater. Sci.* **2014**, *65*, 67–123. https://doi.org/10.1016/j.pmatsci.2014.03.005.

[13] Cárdenas, B.; León, N. High Temperature Latent Heat Thermal Energy Storage: Phase Change Materials, Design Considerations and Performance Enhancement Techniques. *Renew. Sustain. Energy Rev.* **2013**, *27*, 724–737. https://doi.org/10.1016/j.rser.2013.07.028.

[14] Laing, D.; Bahl, C.; Bauer, T.; Fiss, M.; Breidenbach, N.; Hempel, M. High-Temperature Solid-Media Thermal Energy Storage for Solar Thermal Power Plants. *Proc. IEEE* **2012**, *100* (2), 516–524. https://doi.org/10.1109/JPROC.2011.2154290.

[15] Zanganeh, G.; Pedretti, A.; Zavattoni, S.; Barbato, M.; Steinfeld, A. Packed-Bed Thermal Storage for Concentrated Solar Power – Pilot-Scale Demonstration and Industrial-Scale Design. *Sol. Energy* **2012**, *86* (10), 3084–3098. https://doi.org/10.1016/j.solener.2012.07.019.

[16] Khanna, R. Storing Sunlight: Experimental Investigation of a Combined Sensible and Latent Heat Storage for Concentrated Solar Power Plants. **2013**. https://doi.org/10.3929/ethz-a-010075261.

[17] Kenisarin, M.; Mahkamov, K. Solar Energy Storage Using Phase Change Materials☆. *Renew. Sustain. Energy Rev.* **2007**, *11* (9), 1913–1965. https://doi.org/10.1016/j.rser.2006.05.005.

[18] Becattini, V.; Geissbühler, L.; Zanganeh, G.; Haselbacher, A.; Steinfeld, A. Pilot-Scale Demonstration of Advanced Adiabatic Compressed Air Energy Storage, Part 2: Tests with Combined Sensible/Latent Thermal-Energy Storage. *J. Energy Storage* **2018**, *17*, 140–152. https://doi.org/10.1016/j.est.2018.02.003.

[19] Geissbühler, L.; Becattini, V.; Zanganeh, G.; Zavattoni, S.; Barbato, M.; Haselbacher, A.; Steinfeld, A. Pilot-Scale Demonstration of Advanced Adiabatic Compressed Air Energy Storage, Part 1: Plant Description and Tests with Sensible Thermal-Energy Storage. *J. Energy Storage* **2018**, *17*, 129–139. https://doi.org/10.1016/j.est.2018.02.004.

[20] Chen, H.; Zhang, X.; Liu, J.; T, C. Compressed Air Energy Storage. In *Energy Storage - Technologies and Applications*; Zobaa, A., Ed.; InTech, 2013. https://doi.org/10.5772/52221.

[21] Dunham, M. T.; Iverson, B. D. High-Efficiency Thermodynamic Power Cycles for Concentrated Solar Power Systems. *Renew. Sustain. Energy Rev.* **2014**, *30*, 758–770. https://doi.org/10.1016/j.rser.2013.11.010.

[22] Gasanaliev, A. M.; Gamataeva, B. Y. Heat-Accumulating Properties of Melts. *Russ. Chem. Rev.* **2000**, *69* (2), 179–186. https://doi.org/10.1070/RC2000v069n02ABEH000490.

[23] Birchenall, C. E.; Riechman, A. F. Heat Storage in Eutectic Alloys. *Metall. Trans. A* **1980**, *11* (8), 1415–1420. https://doi.org/10.1007/BF02653497.

[24] Iida, T.; Guthrie, R. I. L. *The Physical Properties of Liquid Metals*; Oxford science publications; Clarendon Press: Oxford, 1993.

[25] Wei, G.; Wang, G.; Xu, C.; Ju, X.; Xing, L.; Du, X.; Yang, Y. Selection Principles and Thermophysical Properties of High Temperature Phase Change Materials for Thermal Energy Storage: A Review. *Renew. Sustain. Energy Rev.* **2018**, *81*, 1771–1786. https://doi.org/10.1016/j.rser.2017.05.271.

[26] Yan, M.; Fan, Z. Review Durability of Materials in Molten Aluminum Alloys. *J. Mater. Sci.* **2001**, *36* (2), 285–295. https://doi.org/10.1023/A:1004843621542.

[27] Pasche, G. Interaction between Liquid Aluminium and Solid Iron . Al-Rich Intermetallics Formation PAR. **2013**, *6044*.

[28] *High-Temperature Characteristics of Stainless Steels*; A designers' handbook series; Booklet 9004; Nickel Development Institut: Washington, DC, USA, 1972.

[29] Auerkari, P. *Mechanical and Physical Properties of Engineering Alumina Ceramics*; VTT tiedotteita; VTT Technical Research Center of Finland: Espoo, 1996.

[30] Tobita, K.; Sato, N.; Kitahara, K.; Takagiwa, Y.; Kimura, K. Effect of Anomalous Crystal Structure of Iron Aluminides Fe_2Al_5 and Fe_4Al_{13}: Low Phonon Thermal Conductivity and Potentiality as Thermoelectric Materials. *Mater. Trans.* **2016**, *advpub*. https://doi.org/10.2320/matertrans.MF201607.

[31] *Binary Alloy Phase Diagrams*; Massalski, T. B., Murray, J. L., Bennett, L. H., Baker, H., Eds.; American Society for Metals: Metals Park, Ohio, 1986.

[32] Laurent, V.; Chatain, D.; Chatillon, C.; Eustathopoulos, N. Wettability of Monocrystalline Alumina by Aluminium between Its Melting Point and 1273 K. *Acta Metall.* **1988**, *36* (7), 1797–1803. https://doi.org/10.1016/0001-6160(88)90248-9.

[33] Fujii, H.; Nakae, H.; Okada, K. Interfacial Reaction Wetting in the Boron Nitride/Molten Aluminum System. *Acta Metall. Mater.* **1993**, *41* (10), 2963–2971. https://doi.org/10.1016/0956-7151(93)90111-5.

[34] Solé, A.; Miró, L.; Barreneche, C.; Martorell, I.; Cabeza, L. F. Review of the T -History Method to Determine Thermophysical Properties of Phase Change Materials (PCM). *Renew. Sustain. Energy Rev.* **2013**, *26*, 425–436. https://doi.org/10.1016/j.rser.2013.05.066.

[35] Yinping, Z.; Yi, J.; Yi, J. A Simple Method, the T-History Method, of Determining the Heat of Fusion, Specific Heat and Thermal Conductivity of Phase-Change Materials. *Meas. Sci. Technol.* **1999**, *10* (3), 201–205. https://doi.org/10.1088/0957-0233/10/3/015.

[36] Hong, H.; Kim, S. K.; Kim, Y.-S. Accuracy Improvement of T-History Method for Measuring Heat of Fusion of Various Materials. *Int. J. Refrig.* **2004**, *27* (4), 360–366. https://doi.org/10.1016/j.ijrefrig.2003.12.006.

[37] Marìn, J. M.; Zalba, B.; Cabeza, L. F.; Mehling, H. Determination of Enthalpy Temperature Curves of Phase Change Materials with the Temperature-History Method: Improvement to Temperature Dependent Properties. *Meas. Sci. Technol.* **2003**, *14* (2), 184–189. https://doi.org/10.1088/0957-0233/14/2/305.

[38] Pasche, G.; Scheel, M.; Schäublin, R.; Hébert, C.; Rappaz, M.; Hessler-Wyser, A. Time-Resolved X-Ray Microtomography Observation of Intermetallic Formation Between Solid Fe and Liquid Al. *Metall. Mater. Trans. A* **2013**, *44* (9), 4119–4123. https://doi.org/10.1007/s11661-013-1788-6.

[39] Atabaki, M. M.; Nikodinovski, M.; Chenier, P.; Ma, J.; Harooni, M.; Kovacevic, R. Welding of Aluminum Alloys to Steels: An Overview. *J. Manuf. Sci. Prod.* **2014**, *14* (2). https://doi.org/10.1515/jmsp-2014-0007.

[40] Bouché, K.; Barbier, F.; Coulet, A. Intermetallic Compound Layer Growth between Solid Iron and Molten Aluminium. *Mater. Sci. Eng. A* **1998**, *249* (1–2), 167–175. https://doi.org/10.1016/S0921-5093(98)00573-5.

[41] Shahverdi, H. R.; Ghomashchi, M. R.; Shabestari, S.; Hejazi, J. Microstructural Analysis of Interfacial Reaction between Molten Aluminium and Solid Iron. *J. Mater. Process. Technol.* **2002**, *124* (3), 345–352. https://doi.org/10.1016/S0924-0136(02)00225-X.

[42] Wang, D.; Shi, Z. Aluminizing and Oxidation Treatment of 1Cr18Ni9 Stainless Steel. *Appl. Surf. Sci.* **2004**, *227* (1–4), 255–260. https://doi.org/10.1016/j.apsusc.2003.11.076.

[43] Kobayashi, S.; Yakou, T. Control of Intermetallic Compound Layers at Interface between Steel and Aluminum by Diffusion-Treatment. *Mater. Sci. Eng. A* **2002**, *338* (1–2), 44–53. https://doi.org/10.1016/S0921-5093(02)00053-9.

[44] Deqing, W.; Ziyuan, S.; Longjiang, Z. A Liquid Aluminum Corrosion Resistance Surface on Steel Substrate. *Appl. Surf. Sci.* **2003**, *214* (1–4), 304–311. https://doi.org/10.1016/S0169-4332(03)00505-1.

[45] Deqing, W. Phase Evolution of an Aluminized Steel by Oxidation Treatment. *Appl. Surf. Sci.* **2008**, *254* (10), 3026–3032. https://doi.org/10.1016/j.apsusc.2007.10.059.

[46] Perraudin, D. Y. S.; Binder, S. R.; Rezaei, E.; Ortona, A.; Haussener, S. Phase Change Material Systems for High Temperature Heat Storage. *Chim. Int. J. Chem.* **2015**, *69* (12), 780–783. https://doi.org/10.2533/chimia.2015.780.

[47] Geissbühler, L.; Zavattoni, S.; Barbato, M.; Zanganeh, G.; Haselbacher, A.; Steinfeld, A. Experimental and Numerical Investigation of Combined Sensible/Latent Thermal Energy Storage for High-Temperature Applications. *Chim. Int. J. Chem.* **2015**, *69* (12), 799–803. https://doi.org/10.2533/chimia.2015.799.

[48] Zanganeh, G.; Khanna, R.; Walser, C.; Pedretti, A.; Haselbacher, A.; Steinfeld, A. Experimental and Numerical Investigation of Combined Sensible–Latent Heat for Thermal Energy Storage at 575°C and Above. *Sol. Energy* **2015**, *114*, 77–90. https://doi.org/10.1016/j.solener.2015.01.022.

[49] Geissbühler, L.; Kolman, M.; Zanganeh, G.; Haselbacher, A.; Steinfeld, A. Analysis of Industrial-Scale High-Temperature Combined Sensible/Latent Thermal Energy Storage. *Appl. Therm. Eng.* **2016**, *101*, 657–668. https://doi.org/10.1016/j.applthermaleng.2015.12.031.

[50] Farkas, D.; Birchenall, C. E. New Eutectic Alloys and Their Heats of Transformation. *Metall. Trans. A* **1985**, *16* (3), 323–328. https://doi.org/10.1007/BF02814330.

[51] Sun, J. Q.; Zhang, R. Y.; Liu, Z. P.; Lu, G. H. Thermal Reliability Test of Al–34%Mg–6%Zn Alloy as Latent Heat Storage Material and Corrosion of Metal with Respect to Thermal Cycling. *Energy Convers. Manag.* **2007**, *48* (2), 619–624. http://dx.doi.org/10.1016/j.enconman.2006.05.017.

[52] Wang, X.; Liu, J.; Zhang, Y.; Di, H.; Jiang, Y. Experimental Research on a Kind of Novel High Temperature Phase Change Storage Heater. *Energy Convers. Manag.* **2006**, *47*, 2211–2222. https://doi.org/10.1016/j.enconman.2005.12.004.

[53] Shukla, A.; Buddhi, D.; Sawhney, R. L. Thermal Cycling Test of Few Selected Inorganic and Organic Phase Change Materials. *Renew. Energy* **2008**, *33* (12), 2606–2614. https://doi.org/10.1016/j.renene.2008.02.026.

[54] Tyagi, V. V.; Buddhi, D. Thermal Cycle Testing of Calcium Chloride Hexahydrate as a Possible PCM for Latent Heat Storage. *Sol. Energy Mater. Sol. Cells* **2008**, *92* (8), 891–899. https://doi.org/10.1016/j.solmat.2008.02.021.

[55] Risueño, E.; Faik, A.; Rodríguez-Aseguinolaza, J.; Blanco-Rodríguez, P.; Gil, A.; Tello, M.; D'Aguanno, B. Mg-Zn-Al Eutectic Alloys as Phase Change Material for Latent Heat Thermal Energy Storage. *Energy Procedia* **2015**, *69*, 1006–1013. https://doi.org/10.1016/j.egypro.2015.03.193.

[56] Blanco-Rodríguez, P.; Rodríguez-Aseguinolaza, J.; Risueño, E.; Tello, M. Thermophysical Characterization of Mg–51%Zn Eutectic Metal Alloy: A Phase Change Material for Thermal Energy Storage in Direct Steam Generation Applications. *Energy* **2014**, *72*, 414–420. https://doi.org/10.1016/j.energy.2014.05.058.

[57] Raghavan, V. Al-Fe-Si (Aluminum-Iron-Silicon). *J. Phase Equilibria Diffus.* **2009**, *30* (2), 184–188. https://doi.org/10.1007/s11669-009-9486-1.

[58] Zhou, Z.; Li, Z.; Xie, Y.; Wang, X.; Liu, Y.; Long, Z.; Yin, F. Experimental Study of the Phase Relationships in the Al-Rich Corner of the Al-Si-Fe-Cr Quaternary System at 700°C. *Int. J. Mater. Res.* **2015**, *106* (5), 470–480. https://doi.org/10.3139/146.111202.

[59] Springer, H.; Kostka, A.; Payton, E. J.; Raabe, D.; Kaysser-Pyzalla, A.; Eggeler, G. On the Formation and Growth of Intermetallic Phases during Interdiffusion between Low-Carbon Steel and Aluminum Alloys. *Acta Mater.* **2011**, *59* (4), 1586–1600. https://doi.org/10.1016/j.actamat.2010.11.023.

[60] Chen, S.; Yang, D.; Zhang, M.; Huang, J.; Zhao, X. Interaction Between the Growth and Dissolution of Intermetallic Compounds in the Interfacial Reaction Between Solid Iron and Liquid Aluminum. *Metall. Mater. Trans. A* **2016**, *47* (10), 5088–5100. https://doi.org/10.1007/s11661-016-3667-4.

[61] Yan, M.; Fan, Z. Erosion of H21 Tool Steel in Molten A380 Alloy. *J. Mater. Sci.* **2000**, *35* (7), 1661–1667. https://doi.org/10.1023/A:1004799713069.

[62] Bouayad, A.; Gerometta, C.; Belkebir, A.; Ambari, A. Kinetic Interactions between Solid Iron and Molten Aluminium. *Mater. Sci. Eng. A* **2003**, *363* (1–2), 53–61. https://doi.org/10.1016/S0921-5093(03)00469-6.

[63] Yin, F.; Zhao, M.; Liu, Y.; Han, W.; Li, Z. Effect of Si on Growth Kinetics of Intermetallic Compounds during Reaction between Solid Iron and Molten Aluminum. *Trans. Nonferrous Met. Soc. China* **2013**, *23* (2), 556–561. https://doi.org/10.1016/S1003-6326(13)62499-1.

[64] Yeremenko, V. N.; Natanzon, Ya. V. V; Dybkov, V. I. The Effect of Dissolution on the Growth of the Fe2Al5 Interlayer in the Solid Iron -Liquid Aluminium System. *J. Mater. Sci.* **1981**, *16* [7], 1748–1756. https://doi.org/10.1007/BF00540620.

[65] Stahel, W. *Statistische Datenanalyse: Eine Einführung für Naturwissenschaftler [Statistical data analysis]*, 4th ed.; Springer Vieweg Verlag: Braunschweig, Germany, 2002.

[66] Murray, J. L.; McAlister, A. J. The Al-Si (Aluminum-Silicon) System. *Bull. Alloy Phase Diagr.* **1984**, *5* (1), 74–84. https://doi.org/10.1007/BF02868729.

[67] Atlas Steels; Technical Department. AKSteel - 2013 - Stainless Steel 316L Product Data Bulletin http://www.atlassteels.com.au/ (accessed Mar 20, 2019).

[68] Crank, J. *The Mathematics of Diffusion*, 2d ed.; Clarendon Press: Oxford, [Eng], 1975.

[69] Reddy, B. V.; Deevi, S. C. Thermophysical Properties of FeAl (Fe-40 at.%Al). *Intermetallics* **2000**, *8* (12), 1369–1376. https://doi.org/10.1016/S0966-9795(00)00084-4.

[70] Hale, D. K. The Physical Properties of Composite Materials. *J. Mater. Sci.* **1976**, *11* (11), 2105–2141. https://doi.org/10.1007/PL00020339.

[71] Fan, L.; Khodadadi, J. M. Thermal Conductivity Enhancement of Phase Change Materials for Thermal Energy Storage: A Review. *Renew. Sustain. Energy Rev.* **2011**, *15* (1), 24–46. https://doi.org/10.1016/j.rser.2010.08.007.

[72] Olsson, C.-O. A.; Landolt, D. Passive Films on Stainless Steels—Chemistry, Structure and Growth. *Electrochimica Acta* **2003**, *48* (9), 1093–1104. https://doi.org/10.1016/S0013-4686(02)00841-1.

[73] Papadias, D. D.; Ahluwalia, R. K.; Thomson, J. K.; Meyer, H. M.; Brady, M. P.; Wang, H.; Turner, J. A.; Mukundan, R.; Borup, R. Degradation of SS316L Bipolar Plates in Simulated Fuel Cell Environment: Corrosion Rate, Barrier Film Formation Kinetics and Contact Resistance. *J. Power Sources* **2015**, *273*, 1237–1249. https://doi.org/10.1016/j.jpowsour.2014.02.053.

[74] Seitz, F. On the Porosity Observed in the Kirkendall Effect. *Acta Metall.* **1953**, *1* (3), 355–369. https://doi.org/10.1016/0001-6160(53)90112-6.

[75] Takata, N.; Nishimoto, M.; Kobayashi, S.; Takeyama, M. Crystallography of Fe 2 Al 5 Phase at the Interface between Solid Fe and Liquid Al. *Intermetallics* **2015**, *67*, 1–11. https://doi.org/10.1016/j.intermet.2015.07.011.

[76] Hannon, A. C. Results on Disordered Materials from the GEneral Materials Diffractometer, GEM, at ISIS. *Nucl. Instrum. Methods Phys. Res. Sect. Accel. Spectrometers Detect. Assoc. Equip.* **2005**, *551* (1), 88–107. https://doi.org/10.1016/j.nima.2005.07.053.

[77] Williams, W. G.; Ibberson, R. M.; Day, P.; Enderby, J. E. GEM — General Materials Diffractometer at ISIS. *Phys. B Condens. Matter* **1997**, *241–243*, 234–236. https://doi.org/10.1016/S0921-4526(97)00561-9.

[78] *Neutron Scattering, Part A.*; Sköld, K., Price, D. L., Eds.; Methods of experimental physics; Academic Press: Orlando, 1986.

[79] Bragg, W. L.; Bragg, H. The Structure of Some Crystals as Indicated by Their Diffraction of X-Rays. *Proc. R. Soc. Lond. Ser. Contain. Pap. Math. Phys. Character* **1913**, *89* (610), 248–277. https://doi.org/10.1098/rspa.1913.0083.

[80] Bragg William Henry; Bragg William Lawrence. The Reflection of X-Rays by Crystals. *Proc. R. Soc. Lond. Ser. Contain. Pap. Math. Phys. Character* **1913**, *88* (605), 428–438. https://doi.org/10.1098/rspa.1913.0040.

[81] Delhez, R.; de Keijser, Th. H.; Mittemeijer, E. J. Determination of Crystallite Size and Lattice Distortions through X-Ray Diffraction Line Profile Analysis. *Fresenius Z. Für Anal. Chem.* **1982**, *312* (1), 1–16. https://doi.org/10.1007/BF00482725.

[82] Cullity, B. D.; Stock, S. R. *Elements of X-Ray Diffraction*, 3. ed., internat. ed.; Pearson/Prentice Hall: Upper Saddle River, NJ, 2001.

[83] Shull, C. G.; Wilkinson, M. K. Neutron Diffraction Studies of Various Transition Elements. *Rev. Mod. Phys.* **1953**, *25* (1), 100–107. https://doi.org/10.1103/RevModPhys.25.100.

[84] Stein, F.; Vogel, S. C.; Eumann, M.; Palm, M. Determination of the Crystal Structure of the ε Phase in the Fe–Al System by High-Temperature Neutron Diffraction. *Intermetallics* **2010**, *18* (1), 150–156. https://doi.org/10.1016/j.intermet.2009.07.006.

[85] Sina, H.; Corneliusson, J.; Turba, K.; Iyengar, S. A Study on the Formation of Iron Aluminide (FeAl) from Elemental Powders. *J. Alloys Compd.* **2015**, *636*, 261–269. https://doi.org/10.1016/j.jallcom.2015.02.132.

[86] Planck, M. Ueber Das Gesetz Der Energieverteilung Im Normalspectrum. *Ann. Phys.* **1901**, *309* (3), 553–563. https://doi.org/10.1002/andp.19013090310.

[87] Monshi, A.; Foroughi, M. R.; Monshi, M. R. Modified Scherrer Equation to Estimate More Accurately Nano-Crystallite Size Using XRD. *World J. Nano Sci. Eng.* **2012**, *02* (03), 154–160. https://doi.org/10.4236/wjnse.2012.23020.

[88] *Neutron Scattering, Part B.*; Price, D. L., Ed.; Acad. Press: New York, 1987.

[89] Zienert, T.; Amirkhanyan, L.; Seidel, J.; Wirnata, R.; Weissbach, T.; Gruber, T.; Fabrichnaya, O.; Kortus, J. Heat Capacity of η-AlFe (Fe2Al5). *Intermetallics* **2016**, *77*, 14–22. https://doi.org/10.1016/j.intermet.2016.07.002.

[90] Frutos, E.; Álvarez, D.; Fernandez, L.; González-Carrasco, J. L. Effects of Bath Composition and Processing Conditions on the Microstructure and Mechanical Properties of Coatings Developed on 316 LVM by Hot Dipping in Melted AlSi Alloys. *J. Alloys Compd.* **2014**, *617*, 646–653. https://doi.org/10.1016/j.jallcom.2014.08.020.

[91] Bahlawane, N.; Watanabe, T. New Sol–Gel Route for the Preparation of Pure α-Alumina at 950°C. *J. Am. Ceram. Soc.* **2000**, *83* (9), 2324–2326. https://doi.org/10.1111/j.1151-2916.2000.tb01556.x.

[92] Schlupp, M. V. F.; Binder, S.; Martynczuk, J.; Prestat, M.; Gauckler, L. J. Crack-Free Yttria Stabilized Zirconia Thin Films by Aerosol Assisted Chemical Vapor Deposition: Influence of Water and Carrier Gas. In *Thin Solid Films*; 2012; Vol. 522, pp 58–65. https://doi.org/10.1016/j.tsf.2012.09.042.

[93] Kim, J.; Lin, Y. S. Synthesis and Characterization of Suspension-Derived, Porous Ion-Conducting Ceramic Membranes. *J. Am. Ceram. Soc.* **1999**, *82* (10), 2641–2646. https://doi.org/10.1111/j.1151-2916.1999.tb02135.x.

[94] Lewis, J. A. Colloidal Processing of Ceramics. *J. Am. Ceram. Soc.* **2004**, *83* (10), 2341–2359. https://doi.org/10.1111/j.1151-2916.2000.tb01560.x.

[95] Ikeda, K. Preparation of Fly Ash Monoliths Consolidated with a Sodium Silicate Binder at Ambient Temperature. *Cem. Concr. Res.* **1997**, *27* (5), 657–663. https://doi.org/10.1016/S0008-8846(97)00053-7.

[96] Yuan, M.; Lu, J.; Kong, G.; Che, C. Effect of Silicate Anion Distribution in Sodium Silicate Solution on Silicate Conversion Coatings of Hot-Dip Galvanized Steels. *Surf. Coat. Technol.* **2011**, *205* (19), 4466–4470. https://doi.org/10.1016/j.surfcoat.2011.03.064.

[97] Belova, E. V.; Kolyagin, Ya. A.; Uspenskaya, I. A. Structure and Glass Transition Temperature of Sodium-Silicate Glasses Doped with Iron. *J. Non-Cryst. Solids* **2015**, *423–424*, 50–57. https://doi.org/10.1016/j.jnoncrysol.2015.04.039.

[98] *Aluminum: Properties and Physical Metallurgy*; Hatch, J. E., Ed.; American Soc. for Metals: Metals Park, Ohio, 1984.

[99] Retajczyk, T. F.; Sinha, A. K. Elastic Stiffness and Thermal Expansion Coefficients of Various Refractory Silicides and Silicon Nitride Films. *Thin Solid Films* **1980**, *70* (2), 241–247. https://doi.org/10.1016/0040-6090(80)90364-8.

[100] De Faoite, D.; Browne, D. J.; Chang-Díaz, F. R.; Stanton, K. T. A Review of the Processing, Composition, and Temperature-Dependent Mechanical and Thermal Properties of Dielectric Technical Ceramics. *J. Mater. Sci.* **2012**, *47* (10), 4211–4235. https://doi.org/10.1007/s10853-011-6140-1.

[101] Hayashi, H.; Saitou, T.; Maruyama, N.; Inaba, H.; Kawamura, K.; Mori, M. Thermal Expansion Coefficient of Yttria Stabilized Zirconia for Various Yttria Contents. *Solid State Ion.* **2005**, *176* (5–6), 613–619. https://doi.org/10.1016/j.ssi.2004.08.021.

[102] Solozhenko, V. L.; Peun, T. Compression and Thermal Expansion of Hexagonal Graphite-like Boron Nitride up to 7 GPa and 1800 K. *J. Phys. Chem. Solids* **1997**, *58* (9), 1321–1323. https://doi.org/10.1016/S0022-3697(97)00037-1.

[103] Belenkii, G. L.; Salaev, E. Yu.; Suleimanov, R. A.; Abdullaev, N. A.; Shteinshraiber, V. Ya. The Nature of Negative Linear Expansion in Layer Crystals C, Bn, GaS, GaSe and InSe. *Solid State Commun.* **1985**, *53* (11), 967–971. https://doi.org/10.1016/0038-1098(85)90470-3.

[104] Ellingham Diagram. *Wikipedia*; 2019.

[105] Long, G.; Foster, L. M. Aluminum Nitride, a Refractory for Aluminum to 2000°C. *J. Am. Ceram. Soc.* **1959**, *42* (2), 53–59. https://doi.org/10.1111/j.1151-2916.1959.tb14066.x.

[106] Zhou, X. B.; De Hosson, J. Th. M. Reactive Wetting of Liquid Metals on Ceramic Substrates. *Acta Mater.* **1996**, *44* (2), 421–426. https://doi.org/10.1016/1359-6454(95)00235-9.

[107] Whalen, T. J.; Anderson, A. T. Wetting of SiC, Si_3N_4, and Carbon by Si and Binary Si Alloys. *J. Am. Ceram. Soc.* **1975**, *58* (9–10), 396–399. https://doi.org/10.1111/j.1151-2916.1975.tb19006.x.

[108] Li, J.-G. Wetting of Ceramic Materials by Liquid Silicon, Aluminium and Metallic Melts Containing Titanium and Other Reactive Elements: A Review. *Ceram. Int.* **1994**, *20* (6), 391–412. https://doi.org/10.1016/0272-8842(94)90027-2.

[109] Zhu, C.; Chentao, Y.; Bo, L.; Bangchao, Y. Investigation on the Effects of PbO Content and Seeding Layers of TiO2and ZrO2on the Orientation and Microstructure of Pb(Zr0.52Ti0.48)O3ferroelectric Films Grown by Reverse Dip-Coating Method of Sol-Gel. *Mater. Lett.* **2006**, *60* (13–14), 1559–1564. https://doi.org/10.1016/j.matlet.2005.11.075.

[110] Munro, R. G.; Dapkunas, S. J. Corrosion Characteristics of Silicon Carbide and Silicon Nitride. *J. Res. Natl. Inst. Stand. Technol.* **1993**, *98* (5), 607. https://doi.org/10.6028/jres.098.040.

[111] Lei, W.; Mochalin, V. N.; Liu, D.; Qin, S.; Gogotsi, Y.; Chen, Y. Boron Nitride Colloidal Solutions, Ultralight Aerogels and Freestanding Membranes through One-Step Exfoliation and Functionalization. *Nat. Commun.* **2015**, *6* (1), 8849. https://doi.org/10.1038/ncomms9849.

[112] Khare, S.; Dell'Amico, M.; Knight, C.; McGarry, S. Selection of Materials for High Temperature Latent Heat Energy Storage. *Sol. Energy Mater. Sol. Cells* **2012**, *107*, 20–27. https://doi.org/10.1016/j.solmat.2012.07.020.

[113] Blanco-Rodríguez, P.; Rodríguez-Aseguinolaza, J.; Gil, A.; Risueño, E.; D'Aguanno, B.; Loroño, I.; Martín, L. Experiments on a Lab Scale TES Unit Using Eutectic Metal Alloy as PCM. *Energy Procedia* **2015**, *69*, 769–778. https://doi.org/10.1016/j.egypro.2015.03.087.

[114] Kotzé, J. P.; von Backström, T. W.; Erens, P. J. Simulation and Testing of a Latent Heat Thermal Energy Storage Unit with Metallic Phase Change Material. *Energy Procedia* **2014**, *49*, 860–869. https://doi.org/10.1016/j.egypro.2014.03.093.

[115] Rubenstein, L. I. *The Stefan Problem. Translations of Math*; Monographs, 1971.

[116] Prüss, J.; Saal, J.; Simonett, G. Existence of Analytic Solutions for the Classical Stefan Problem. *Math. Ann.* **2007**, *338* (3), 703–755. https://doi.org/10.1007/s00208-007-0094-2.

[117] Voller, V.; Cross, M. Accurate Solutions of Moving Boundary Problems Using the Enthalpy Method. *Int. J. Heat Mass Transf.* **1981**, *24* (3), 545–556. https://doi.org/10.1016/0017-9310(81)90062-4.

[118] Hu, H.; Argyropoulos, S. A. Mathematical Modelling of Solidification and Melting: A Review. *Model. Simul. Mater. Sci. Eng.* **1996**, *4* (4), 371–396. https://doi.org/10.1088/0965-0393/4/4/004.

[119] Neumannn, F. Die Partiellen Differentialgleichungen Der Mathematischen Physik. *Reimann–Weber* **1912**, *2*, 121.

[120] Paterson, S. Propagation of a Boundary of Fusion. *Glasg. Math. J.* **1952**, *1* (1), 42–47. https://doi.org/10.1017/S2040618500032937.

[121] Spink, C. H. Differential Scanning Calorimetry. In *Methods in Cell Biology*; Elsevier, 2008; Vol. 84, pp 115–141. https://doi.org/10.1016/S0091-679X(07)84005-2.

[122] Kenfack, F.; Bauer, M. Innovative Phase Change Material (PCM) for Heat Storage for Industrial Applications. *Energy Procedia* **2014**, *46*, 310–316. https://doi.org/10.1016/j.egypro.2014.01.187.

[123] Sandnes, B.; Rekstad, J. Supercooling Salt Hydrates: Stored Enthalpy as a Function of Temperature. *Sol. Energy* **2006**, *80* (5), 616–625. https://doi.org/10.1016/j.solener.2004.11.014.

[124] Binder, S.; Haussener, S. Design Guidelines for Al-12%Si Latent Heat Storage Encapsulations to Optimize Performance and Mitigate Degradation. *Appl. Surf. Sci.* **2019**, 143684. https://doi.org/10.1016/j.apsusc.2019.143684.

[125] Hampshire, S. Oxynitride Glasses, Their Properties and Crystallisation – a Review. *J. Non-Cryst. Solids* **2003**, *316* (1), 64–73. https://doi.org/10.1016/S0022-3093(02)01938-5.

[126] Jin, J.; Sakka, S.; Kozuka, H.; Yoko, T. Formation and Chemical Durability of Na-Si-O-N and Na-Al-Si-O-N Oxynitride Glasses. *J. Ceram. Soc. Jpn.* **1992**, *100* (1162), 841–846. https://doi.org/10.2109/jcersj.100.841.

Curriculum vitae

Contact information

Selmar Binder (27.3.1988)
Rue du Centre 80A
CH-1025, St-Sulpice
+41 77 423 45 41 / selmarbinder@gmail.com

Overview

1988-1999	Thurgau, CH	South of the Bodensee
…-2005	Obwalden, CH	Fast track Matura
…-2009	Zürich, CH	BSc, ETHZ, material science
…-2012	Luzern, CH	Industrial placement, Schindler R&D
…-2014	Zürich, CH	MSc, ETHZ, material science
…-2019	Lausanne, CH	PhD, EPFL-…-LRESE***

***Laboratory of renewable energy science and engineering, doctoral school of energy (EDEY), current employer

- “Electrical conductivity and microstructure of yttrium doped zirconia (YDZ) thin films” (BSc thesis at (II))
- “Bivalent Hyper-branched Polymers: Dual-Reactive Scaffold Synthesis through Proton Transfer Polymerization and Bi-functionalization Aspects” (MSc thesis at (III))

- “Preparation of Phase Change Material Encapsulations for Fast and Reliable Latent Heat Thermal Energy Storage” (PhD thesis at ***)

Journal Publications[1–6]

[1] Scherrer, B.; Martynczuk, J.; Galinski, H.; Grolig, J. G.; Binder, S.; Bieberle-Hütter, A.; Rupp, J. L. M.; Prestat, M.; Gauckler, L. J. Microstructures of YSZ and CGO Thin Films Deposited by Spray Pyrolysis: Influence of Processing Parameters on the Porosity. Advanced Functional Materials 2012, 22 (16), 3509–3518. https://doi.org/10.1002/adfm.201200454.

[2] Schlupp, M. V. F.; Binder, S.; Martynczuk, J.; Prestat, M.; Gauckler, L. J. Crack-Free Yttria Stabilized Zirconia Thin Films by Aerosol Assisted Chemical Vapor Deposition: Influence of Water and Carrier Gas. Thin Solid Films 2012, 522, 58–65. https://doi.org/10.1016/j.tsf.2012.09.042.

[3] Gadwal, I.; Binder, S.; Stuparu, M.; Khan, A. Dual-Reactive Hyperbranched Polymer Synthesis through Proton Transfer Polymerization of Thiol and Epoxide Groups. Macromolecules 2014, 47 (Scheme 1), 5070–5080.

[4] Binder, S.; Gadwal, I.; Bielmann, A.; Khan, A. Thiol-Epoxy Polymerization via an AB Monomer: Synthetic Access to High Molecular Weight Poly(β-Hydroxythio-Ether)s. Journal of Polymer Science Part A: Polymer Chemistry 2014, 52 (14), 2040–2046. https://doi.org/10.1002/pola.27212.

[5] Perraudin, D. Y. S.; Binder, S. R.; Rezaei, E.; Ortona, A.; Haussener, S. Phase Change Material Systems for High Temperature Heat Storage. CHIMIA International Journal for Chemistry 2015, 69 (12), 780–783. https://doi.org/10.2533/chimia.2015.780.

[6] Binder, S.; Haussener, S. Design Guidelines for Al-12%Si Latent Heat Storage Encapsulations to Optimize Performance and Mitigate Degradation. *Applied Surface Science* **2019**, 143684. https://doi.org/10.1016/j.apsusc.2019.143684.

In preparation[7–10]

[7] Binder, S.; Haussener, S. *provisional Title* Stabilization of 316L Steel Encapsulated Liquid Al-13%Si by a Modified Dip-Coating Procedure for Ceramic Suspensions.

[8] Binder, S.; Haussener, S. *provisional Title* Calorimetric Load-Cycle Stability of Coated and Uncoated PCM Encapsulations.

[9] Binder, S.; Haussener, S. *provisional Title* Processing and Deposition of Composite Boron Nitride Diffusion Barrier Coatings for High Temperature Latent Heat Storage with Molten Metals.

[10] Binder, S.; Haussener, S. *provisional Title*Time Resolved Neutron Scattering Experiment on Anomalous Crystallite Growth in Early Fe_2Al_5 Formation.

Conference Presentations

- “Encapsulation Strategy for Metallic Phase Change Materials used for High-Temperature Heat Storage” - Selmar Binder, Sophia Haussener, Materials Science & Technology 2016, Energy Storage VI: Materials, Systems and Applications Symposium, Salt Lake City, UT, USA
- “In situ cycling stability evaluation in an encapsulated high-temperature phase change material system” -Selmar Binder, Sophia Haussener, Euromat 2017, C8: Solidification, Casting, Foundry and Liquid Metal processing, Thessaloniki, Greece
- “Encapsulation strategy for stable metallic phase change materials” - Selmar Binder, Sophia Haussener, Euromat 2017, C5: Interface Design and Modelling, Wetting and High-Temperature Capillarity, Thessaloniki, Greece

Analytic tools

- SEM: Formal training at microscopy center (CIME, EPFL) on Merlin-Gemini-II in VP-mode, EDX, etc. + previous trainings at (II) on LEO-Gemini + spare time project (Octanis: tech start-up) on S-scan120
- H-NMR (see org. synth.)
- DSC (Polymers, Metals)
- Neutron-Diffraction (Fe-Al-intermetallic compounds)
- IR/UV-VIS, XRD, light microscopy, microstructure analysis, …

Synthesis techniques

- Suzuki-Miyaura coupling, Tetrakis(triphenylphosphine)-Pt(0) catalyst (Schlüter's M6 2-D monomer), Thiol-ene Michaels-Addition (thiol-epoxy AB and AB2-monomer), + various organic chem.-lab. Survival skills
- Polymers: Thiol-epoxy poly-cond., hν-induced Diels-Alder-addition, Suzuki-Miyaura poly-cond.
- Thin film deposition: YSZ (spray-pyrolysis, metal-organic CVD), Alumina (metal-organic sol-gel dip-coating), Sodium silicate (inorganic sol-gel dip-coating),

- Colloidal thick film deposition: Alumina, silica, silicon nitride, boron nitride, zirconia

**Ce document a été imprimé au Centre d'impression EPFL,
imprimerie climatiquement neutre, certifiée myClimate.**